AALBORG UNIVERSITY
STUDENT REPORT

FACULTY OF ENGINEERING AND SCIENCE
MSc. in Mechatronic Control Engineering

Investigation into Tribological state observation in journal bearings using ultrasound and temperature measurements

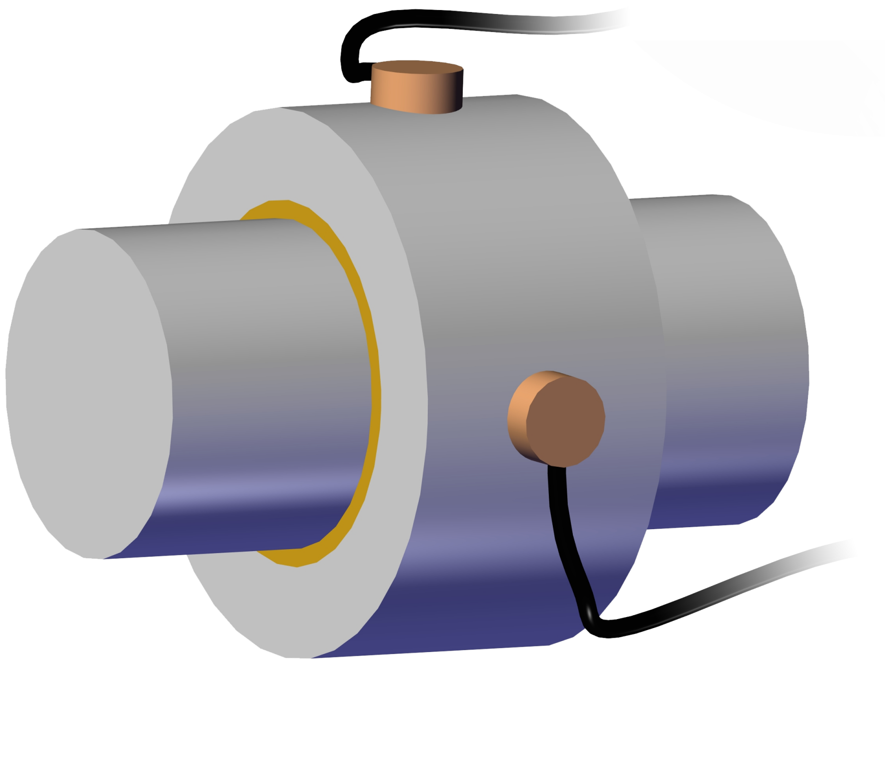

Master's Thesis
Group MCE4-1024
Energy Engineering - Mechatronics
Aalborg University
May, 2021

Programs such as Maple, Matlab, Comsol, and Simulink have been used to do calculations, simulations and graphs. Latex has been used as the typesetting program to produce this report.

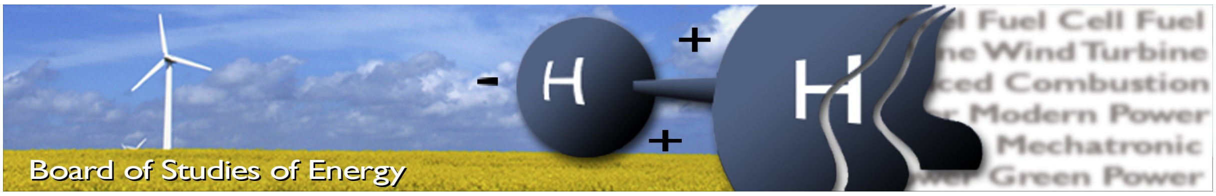

Title: Investigation into Tribological state observation in journal bearings using ultrasound and temperature measurements
Semester: 10$^{\text{th}}$
Semester theme: Master's Thesis
Project period: 05.02 2021 to 28.05 2021
ECTS: 30
Supervisor: Per Johansen
Project group: MCE4 - 1024

Group members:
Andreas Filtenborg Laustsen
Elias Vagn Hansen
Morten Nielsen

Total: 114 pages
Appendix: 17 pages

Synopsis

This study investigates the robustness and accuracy of different tribological state observer strategies using ultrasound reflectometry and temperature measurements. Based on virtual experiments it is from this study found that including thermoviscous effects in the hydrodynamic system model significantly increases the robustness and accuracy of the tribological state observers. It is in this study also found that placing the ultrasound transducers inside the journal is beneficial for the tribological state observer strategies.

It is in this study proposed combining auto-calibration ultrasound reflectometry and tribological state observer methods. It is found that these algorithms have increased robustness and accuracy compared to the standalone auto-calibration ultrasound reflectometry used for comparison.

By accepting the request from the fellow student who uploads the study group's project report in Digital Exam System, you confirm that all group members have participated in the project work, and thereby all members are collectively liable for the contents of the report. Furthermore, all group members confirm that the report does not include plagiarism.

Summary

This study is concerned with estimating the fluid film height and other tribological states in journal bearings relating to wear and friction using tribological state observer strategies. The study takes offset in a case study of a simple journal bearing. The tribological state observer strategies proposed in this study, is based on including a system model of the hydrodynamics in the journal bearing into an extended Kalman filter optimisation algorithm with ultrasound reflectometry, temperature measurements, and information of the system inputs, such as journal angular velocity and external radial force, to increase the robustness and accuracy of the tribological state estimates.

This study is a continuation of a previous study of the same authors. The previous study investigated the applicability of tribological state observes in journal bearings, using ultrasound reflectometry methods. In the previous study it is found from virtual experiments that tribological state observers show potential for predictive maintenance and prognostic control schemes. This study therefore aims to further investigate some of the aspects excluded in the previous study.

This study investigates the development of an improved virtual experimental setup, compared to the previous study. The virtual experimental setup developed in this study includes thermoviscous hydrodynamics, since it is found that these significantly affects the dynamics and steady state condition of journal bearings. Furthermore, the virtual experimental setup is made to include thermodynamics in the fluid film layer, journal, and bushing. Lastly the virtual experimental setup is improved since it does not use the short bearing approximation, included in the virtual experiments from the previous study. The virtual experimental setup allows for data generation used for the comparison of the tribological state observer strategies.

This study also investigates the performance of combined tribological state observer and auto-calibration ultrasound reflectometry methods. It is in this study found that these methods have increased robustness and accuracy, compared to the standalone auto-calibration ultrasound reflectometry method derived in this study. Furthermore, this study includes an evaluation criterion for the ultrasound reflectometry that uses multi-frequency information from the measured ultrasound waves. In this study, the method is not seen to improve the tribological state estimates. This method is found to be less sensitive to disturbances at large fluid film heights, compared to the other methods proposed, and for this reason might be used in combination with other methods.

This study is also concerned with strategies for placing the ultrasound transducers on the journal bearing. It is in this study found that placing the ultrasound transducers on the inside of the journal show the greatest potential for the ultrasound reflectometry methods. This is due to the increased excitements in the fluid film height seen from the transducers, and this aids the assumption of slow varying incident waves, required for the derivation of the tribological state

observer and ultrasound reflectometry methods.

In this study it is found that including thermoviscous effects in the hydrodynamic model, used for the tribological state observer strategies, have increased accuracy and robustness, compared to tribological state observer that uses regular hydrodynamic models. The thermoviscous effects are included in the tribological state observers using perturbation theory for solving the equation describing energy conservation within the fluid film layer. It is also from this study found that with the inclusion of thermodynamics in the tribological state observer, it is possible to get an estimate of the dynamic viscosity of the oil. This estimate is seen to have an offset compared to the true value, but from the estimate it is possible to track changes of the dynamic viscosity, and relate this to degradation of the oil. However, the tribological state observer strategies might need further improvement, since it is found that the dynamic viscosity estimate is affected by changes to other system parameters. It is in this study found that changes to the radial clearance affect the system dynamics to a degree that is not described by adjusting the dynamic viscosity estimate. It is from this believed that it might be possible to expand the tribological state observer algorithms to include an estimate of the radial clearance.

In this study it is also found that the tribological state observer strategies that include thermoviscous effects are able to estimate both fluid film height and dynamic viscosity to a satisfying degree with limited knowledge of the external force. This is a great indication of the potential of tribological state observers since it might not be possible to measure the external force in real-life applications. However, it is still believed that in order to fully explore the applicability of tribological state observers, the strategies have to be experimentally validated in a laboratory environment.

Preface

This study is a master's thesis project written by 3 students studying Mechatronic Control Engineering at AAU. This study is a continuation of a study written by the same authors named "Investigation of a tribological state observer using an ultrasound reflectometry method for measurement of the fluid film height in journal bearings".

This study aims to investigate the effects of implementing tribological state observer in a journal bearing to predict the fluid film height of the lubrication based on ultrasound and temperature measurements.

Readers guide

The figures in this project depicting the journal bearing are highly exaggerated to better illustrate the concepts of interest.

Equations, figures, and tables are denoted as x.y, where x denoted the chapter at which it is located and y is the number for the certain element in that given chapter.

Matrices and vectors is in this project denoted as "$\underline{\ \ }$" and "$\vec{\ }$", respectively. Furthermore, "$\dot{\ }$" denotes time derivatives and "$\hat{\ }$" denotes estimates.

The sources in this study are noted with the Vancouver notation.

Nomenclature

Symbol	Name	Unit
A	Magnitude of reflection coefficient spectrum	$[-]$
a, b	Local coordinate frame	$[m]$
a, b, c	Material layers	$[-]$
a_{bv}	Barus-Vogel viscosity	$[Pa\,s]$
a_r	Reynold viscosity	$[Pa\,s]$
a_v	Vogel viscosity	$[Pa\,s]$
$a_{1,bv}$	Barus-Vogel viscosity	$[Pa]$
$a_{2,bv}$	Barus-Vogel viscosity	$[\frac{Pa}{K}]$
Br	Brinkman number	$[-]$
b_{bv}	Barus-Vogel viscosity	$[K]$
b_r	Reynold viscosity	$[K^{-1}]$
b_v	Vogel viscosity	$[K]$
C	Specific heat capacity	$[\frac{J}{kg\,K}]$
$\underline{C}$	Covariance matrix	[-]
C_r	Radial clearance	$[m]$
c	Speed of sound	$[\frac{m}{s}]$
c_{bv}	Barus-Vogel viscosity	$[K]$
c_v	Vogel viscosity	$[K]$
$\vec{d}$	Disturbance vector	[-]
Ec	Eckert number	$[-]$
F	Force	$[N]$
f	Fluid stress	$[\frac{N}{m^2}]$
h	Fluid film height	$[m]$
$J(\omega)$	Layer phase spectrum	$[-]$
L	Bushing length	$[m]$
L_j	Journal length	$[m]$
L_N	Load number	[-]
L_T	Distance from ultrasound transducer to flid film	$[m]$
m	Mass of the journal	$[kg]$
n	Number of wave	$[-]$
$\vec{n}$	Noise vector	[-]
$\vec{n}$	Normal vector	[-]
$\underline{P}$	Covariance matrix	[-]
P_e	Energy in the ultra sound signal	$[-]$
p	Pressure	[Pa]
Q_f	Heat source	$[\frac{W}{m^3}]$
R	Bushing inner radius	$[m]$
R	Reflection coefficient	$[\frac{kg}{s\,m^2}]$

R	Reflection wave	$[Pa]$
R_b	Bushing outer radius	$[m]$
Re	Reynolds number	$[-]$
$R(\omega)$	Reflection coefficient spectrum	$[-]$
r	Journal radius	$[m]$
S	Sensitivity	$[-]$
T	Temperature	$[K]$
T	Transmission wave	$[Pa]$
T_{eq}	Equivalent temperature	$[-]$
T_{pr}	Time of pulse rate	$[-]$
T_s	Sampling time	$[s]$
t	Time	[s]
u, v, w	Velocity components	$[\frac{m}{s}]$
$\vec{v}$	Velocity vector	$[m/s]$
x, y, z	Spacial coordinates	$[m]$
z	Specific acoustic impedance	$[\frac{kg}{s\,m^2}]$
α, β	Global coordinate frame	$[m]$
α_i, β_i	Local coordinate frame following the ultrasound transducers	$[-]$
γ	Phase of reflection coefficient spectrum	$[rad]$
δ	Fluidity	$[\frac{1}{Pa\,s}]$
ϵ	Eccentricity	$[m]$
ϵ_r	Eccentricity ratio	[-]
θ	Eccentricity angle	$[rad]$
λ	Thermal conductivity	$[\frac{W}{m\,K}]$
μ	Dynamic viscosity	$[Pa\,s]$
ξ	Attitude angle	$[rad]$
ρ	Density	$[\frac{kg}{m^3}]$
σ	Standard deviation	$[-]$
τ	Time delay	$[s]$
τ	Shear stress	$[\frac{N}{m^3}]$
Φ	Viscous dispassion	$[s^{-2}]$
ϕ	Polar coordinate	$[rad]$
ψ	Angle of pressure state vector	$[rad]$
Ω	Measurement angle from α	$[rad]$
ω	Angular frequency	$[\frac{rad}{s}]$
ω	Angular velocity of the journal	$[\frac{rad}{s}]$

Abbreviation	Definition
COM	Centre of mass
CCE	Complex component evaluation
CCTE	Complex component and temperature evaluation
EKF	Extended Kalman filter
eq.	Equation
LMSE	Layer spectrum magnitude evaluation
LPL	Layer phase lag
LTI	Linear time independent
PDE	Phase derivative evaluation
p.	page
SISO	Single input single output
S.S.	Steady state
TSO	Tribological state observer

Table of Contents

1 Introduction

This study aims to investigate the applicability of tribological state observer (TSO) strategies and the ability to estimate tribological states in journal bearings using measurements from ultrasound transducers. Journal bearings are of interest since they are widely used in industries as a way of separating rotating components. The journal bearing have two primary tasks, reducing the friction and wear in the system. This results in a reduced energy loss and less maintenance on the system. Journal bearings use a fluid lubrication layer as the separating element, as seen in Figure 1.1.

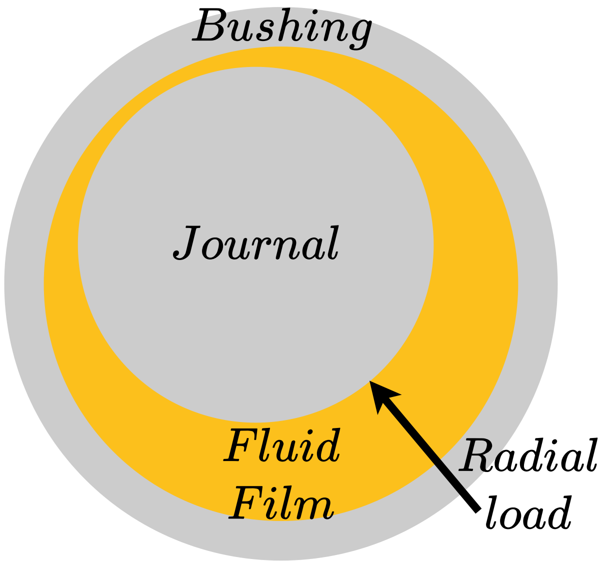

Figure 1.1: Journal bearing under radial load.

Figure 1.1 illustrates a journal bearing under radial load. It is in this figure seen that when a journal bearing is under a radial load, the geometric centre of the journal and bushing misalign. If this misalignment becomes to large an excess amount of friction occur in the journal bearing. This results in decreased efficiency as well as increased wear on the journal bearing. Furthermore, tribological states such as the viscosity of the lubrication is an indication of a degraded lubrication film [9]. It is believed that with TSOs it is possible to monitor the tribological states and use this information for condition monitoring or prognostic control of the journal bearings.

1.1 Case study

In this study the investigation into TSOs is based on a case study. In the case study the journal bearing is modelled as shown in Figure 1.2 on the following page. The journal bearing model is chosen to be a cylinder as the journal and a cylindrical shell as the bearing.

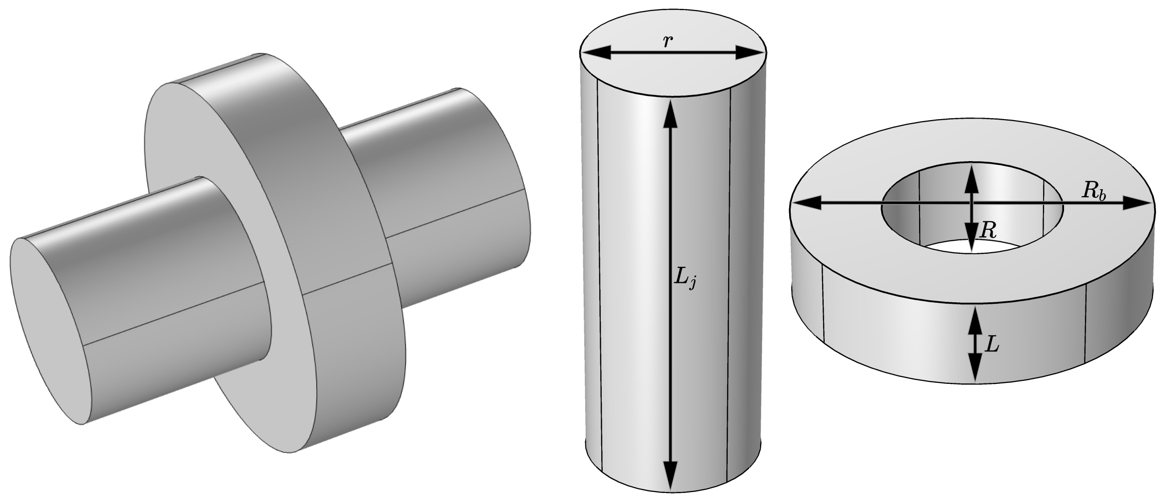

(a) Journal bearing **(b)** Journal and bushing

Figure 1.2: Dimension definitions of the journal bearing case study.

The journal bearing depicted in the figure has the parameters shown in Table 1.1.

Table 1.1: Baseline parameters of journal bearing

Journal length, $\mathrm{L_J}$	50 mm
Journal radius, r	9.95 mm
Bushing length (fluid film length), L	10 mm
Bushing inner radius, R	10 mm
Bushing outer radius, $\mathrm{R_b}$	20 mm
Radial clearance, $\mathrm{C_r}$	50 μm
Journal mass, m	2 kg
Operational temperature, T	313.2 K

These dimensions form the baseline for the journal bearing analysis in this study. The mass of the journal is chosen to be 2 kg. This is based on the assumption that the journal is connected to larger components. It is from the table further seen that in this study the operational temperature is assumed to be 313.2 K, unless otherwise stated. A full list of baseline parameters used throughout this report is found in Appendix G on page 113.

2 Problem analysis

This study is a continuation of a previous study from the same authors, Laustsen et al. [12]. The previous study showed through virtual experiments that the proposed tribological state observer strategies reduced noise and increased robustness of fluid film height estimates. The tribological state observer further showed similar journal bearing dynamics as the virtual experiments. It is from the previous study therefore believed that tribological state observer strategies has potential. However, in the previous study thermoviscous effects were neglected and it is therefore of interest to analyse if these have a significant effect on the system.

2.1 Temperature dependent viscosity

The initial analysis of the thermoviscous effects take offset in the Vogel viscosity model, given by the following equation. [7]

$$\mu_v = a_v \, e^{\frac{b_v}{T - c_v}} \tag{2.1}$$

Where μ is the dynamic viscosity. T is the temperature of the oil. a_v, b_v, and c_v are fluid specific parameters given in Table 2.1 for HM46 hydraulic oil.

Table 2.1: Parameters used for the Vogel model. [7]

a_v	b_v	c_v
63.34 µPas	879.8 K	177.8 K

The Vogel viscosity model is used to determine the baseline dynamic viscosity in this study and is seen plotted in Figure 2.1.

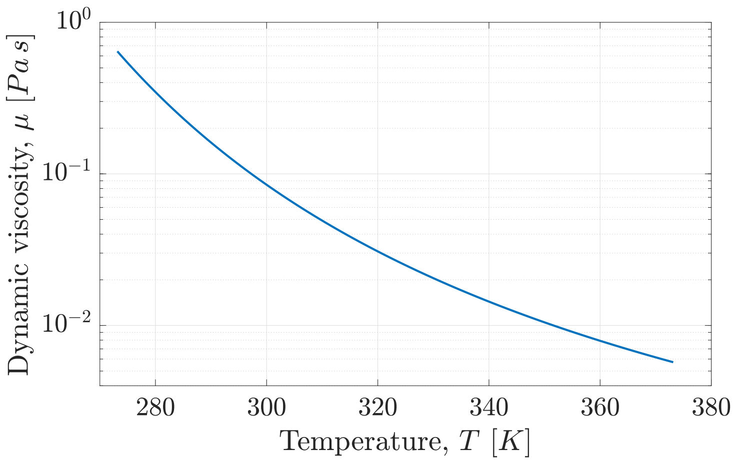

Figure 2.1: The viscosity as a function of temperature.

The dynamic viscosity is seen to be highly dependent on the temperature and for the 100 degrees of temperature change plotted, the viscosity is seen to change several order of magnitudes.

2.2 G.B. DuBois and F.W. Ocvirk's steady state solution

It is seen that the viscosity affects the steady state (S.S.) of the journal bearing. The relation between viscosity and S.S. of the journal bearing, is found from the load number, L_n. The load number is found to be related to the placement of the journal within the journal bearing in S.S. This placement is described by the eccentricity, ϵ. The eccentricity is defined as the distance between the geometric centre of the journal and bushing. This relation is both described and experimentally validated by G.B. DuBois and F.W. Ocvirk and is given by the following equation. [8]

$$L_N = 4\,\pi\,\frac{|\vec{F}_{ext}|\,C_r^2}{\mu\,\omega\,L^3\,R} = \frac{\pi\,\frac{\epsilon}{C_r}\sqrt{\pi^2\left(1-\left(\frac{\epsilon}{C_r}\right)^2\right)+16\,\left(\frac{\epsilon}{C_r}\right)^2}}{\left(1-\left(\frac{\epsilon}{C_r}\right)^2\right)^2} \tag{2.2}$$

Where $\vec{F}_{ext}$ is the external force and ω is the angular velocity of the journal. It is notable that it is the ratio between eccentricity and radial clearance that explicitly correlates to the load number. This relation is known as the eccentricity ratio, ϵ_r. The eccentricity ratio is also found to relate to the eccentricity angle, θ, in S.S. The eccentricity angle is defined as angle with least fluid film height, measured from an arbitrary coordinate frame. However, attitude angle, ξ, is defined as the angle with least fluid film height measured from the direction of the external force. With these definitions the following relation is found.

$$\xi = tan^{-1}\left(\frac{\pi\sqrt{1-\left(\frac{\epsilon}{C_r}\right)^2}}{4\left(\frac{\epsilon}{C_r}\right)}\right) = \theta - \angle\vec{F}_{ext} \tag{2.3}$$

Using eq. (2.2) and eq. (2.3) it is possible to calculate the placement of the journal within the journal bearing in S.S. for a given angular velocity and external force.

The S.S. eccentricity is from eq. (2.2) seen to be dependent on the viscosity and thereby the temperature. The S.S. eccentricity is seen as a function of the temperature for different magnitudes of the external force and a journal angular velocity of 500 rad/s in Figure 2.2.

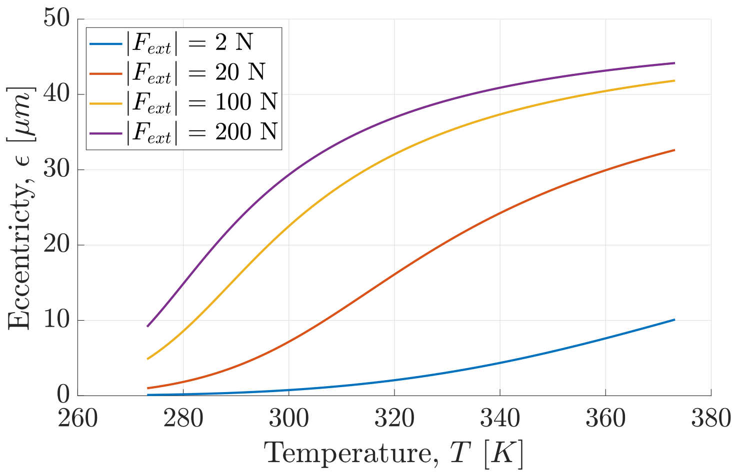

Figure 2.2: The S.S. eccentricity as a function of temperature at different external loads.

The S.S. eccentricity is seen to be dependent on the temperature and this is especially evident for large external loads. It should be noted that this analysis is based on the assumption that the thermal expansion and deflection of the journal and bushing can be neglected. This assumption is used in the study from hereon. This analysis indicates that thermoviscous effects are significant enough to further investigate how they affect the performance of a TSO for journal bearings.

2.3 Study purpose

Based on the above problem analysis and the previous study by the same authors, this study aims to investigate the following topics. The above analysis shows that thermoviscous effects are found to have significant influence on the steady state placement of the journal, it is therefore of interest to investigate these. The tribological state observer strategies presented in the previous study uses a separate ultrasound reflectometry and tribological state observer algorithm, where this study aims to investigate the combination of these algorithms, since this is believed to increase the robustness of the strategy. The previous study proposes placing the ultrasound transducers on the outside of the bushing, however another study proposes placing the transducer within the journal [1]. This way of placing the ultrasound transducer also have the potential of affecting the robustness of the algorithms and is for this reason of interest to investigate. Furthermore this study aims to investigate a method of accessing the external loads affecting the journal bearing which is a concern from the previous study. Lastly, this study is concerned with investigating the theoretical potential of tribological state observer algorithms, and it is for this reason of interest to develop a more complex system model used for virtual experiments, compared to the previous study.

To summarise, this study is concerned with the following five main topics:

- Development of an advanced virtual experiment which includes thermoviscous hydro- and thermodynamics.
- Investigation into the performance of combined tribological state observer and ultrasound reflectometry algorithms.
- Investigation into the accuracy and robustness of fluid film height estimates considering ultrasound transducer placement.
- Investigation into the accuracy and robustness of the tribological state observer algorithms when considering thermoviscous hydrodynamics.
- Investigation into the robustness of the tribological state observer algorithms with limited knowledge of the external force.

3 Journal bearing model

In order to derive TSO strategies and perform system analysis an analytical journal bearing model is derived. The analytical journal bearing model describes hydrodynamics, mechanical dynamics, and the coupling between these.

3.1 Bearing geometry and mechanical dynamics

The derivation of the mechanical journal bearing dynamics takes offset in the coordinate definitions shown in Figure 3.1.

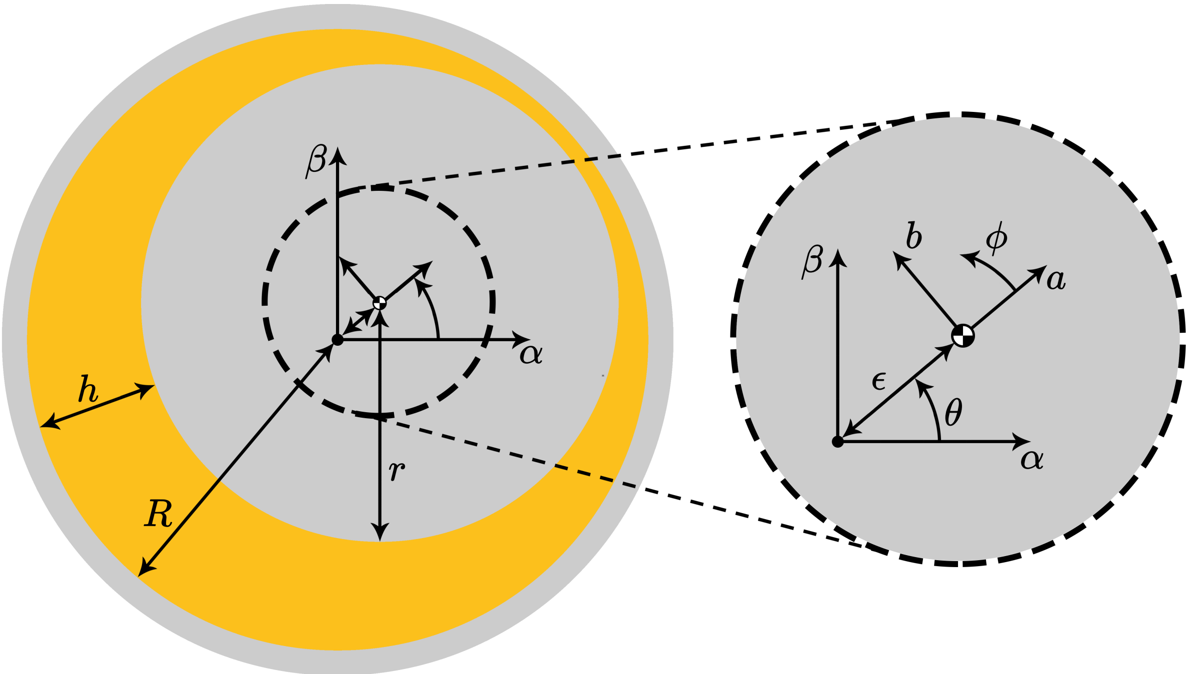

Figure 3.1: The coordinate definitions used for the derivation of the journal bearing kinematics [12].

The figure shows two coordinate frame definitions. The global coordinate frame, $\alpha\beta$, is defined to have origin in the centre of the journal but otherwise placed arbitrary in space. It is in this coordinate frame that the eccentricity and eccentricity angle are defined. The eccentricity is defined as the distance between the geometric centre of the bushing and journal, given as the equation below.

$$\epsilon = \sqrt{\alpha^2 + \beta^2} \tag{3.1}$$

The eccentricity angle is defined as the angle between the α-axis and the eccentricity.

$$\theta = tan^{-1}\left(\frac{\beta}{\alpha}\right) \tag{3.2}$$

In Figure 3.1 on the previous page it is seen that the local coordinate frame, ab, is defined to have origin in the geometric centre of the journal and the a-axis is defined such that it is always aligned with the eccentricity angle. In the figure it is also seen that the inner radius of the bushing is defined as R and the outer radius of the journal is defined as r. The radial clearance, C_r, is defined as the difference between the two radii.

$$C_r = R - r \tag{3.3}$$

In the ab-frame an arbitrary angle, ϕ, is defined as the angle from the a-axis to an arbitrary angle of interest. It is from this angle seen that the fluid film height is defined as stated in eq. (3.4) assuming that the fluid film height does not change in the longitudinal direction of the bearing.

$$h = C_r - \epsilon \, cos\,(\phi) \tag{3.4}$$

The mechanical dynamics of the system is found from an Euler-Lagrange analysis of the system kinematics. The Euler-Lagrange analysis is based on the Lagrangian, $\mathcal{L}$, defined as the difference between the kinetic and potential energy of the system [19].

$$\mathcal{L} = \mathcal{K} - \mathcal{P} \tag{3.5}$$

Where $\mathcal{K}$ is kinetic energy and $\mathcal{P}$ is potential energy. In order to derive the energies of the system a kinematic expression is derived. The kinematic expression describes the placement of the journal's centre of mass (COM) within the global coordinate frame and is given in eq. (3.6), assuming that the mass of the journal is uniformly distributed.

$$\overrightarrow{COM} = \epsilon \begin{bmatrix} cos(\theta) \\ sin(\theta) \end{bmatrix} \tag{3.6}$$

It is for this analysis only translatory kinetic energy that is considered. This consideration is based on the assumption that the only potential energy affecting the system is that of gravitational force and this is seen as an external force and is for this reason not included in the dynamics of the system. The reason for not considering rotational kinetic energy is due to the angular velocity of the journal is seen as an input to the system. This means that the dynamics of this rotation is not of interest. These assumptions results in the following Lagrangian.

$$\mathcal{L} = \mathcal{K} = \frac{1}{2}\frac{d}{dt}\overrightarrow{COM}^T m \frac{d}{dt}\overrightarrow{COM} = \frac{m}{2}\left(\dot{\epsilon}^2 + \left(\dot{\theta}\,\epsilon\right)^2\right) \tag{3.7}$$

With this Lagrangian it is possible to derive the mechanical journal bearing dynamics using the Euler-Lagrange equation, as given by eq. (3.8). [19]

$$\vec{F} = \frac{d}{dt}\left(\frac{\partial \mathcal{L}}{\partial \dot{\vec{q}}}\right) - \frac{\partial \mathcal{L}}{\partial \vec{q}} \tag{3.8}$$

Where $\vec{q}$ is the coordinate vector, given by eq. (3.9).

$$\vec{q} = \begin{bmatrix} \theta \\ \epsilon \end{bmatrix} \tag{3.9}$$

This analysis results in the following equation for the mechanical system dynamics.

$$\vec{F} = m \begin{bmatrix} \epsilon \left(\ddot{\theta}\, \epsilon + 2\dot{\theta}\, \dot{\epsilon} \right) \\ \ddot{\epsilon} - \epsilon\, \dot{\theta}^2 \end{bmatrix} \tag{3.10}$$

In Figure 3.1 on page 7 it is seen that the force components along the b-axis are the forces which cause the torque affecting the eccentricity angle. This torque is seen in eq. (3.11) to be the forces in the b-direction multiplied by the eccentricity. The forces affecting the eccentricity is from the figure seen to be the forces in the a-direction.

$$\vec{F} = \begin{bmatrix} F_b \cdot \epsilon \\ F_a \end{bmatrix} \tag{3.11}$$

It is assumed that the forces affecting the journal are external, pressure, F_p, and shear, F_s, forces. The pressure and shear forces are due to the fluid film layer in the journal. It is in this study assumed that the shear forces only produce a translatory motion of the journal since the dynamics of the journal's rotation around its own axis is not of interest. It is assumed that a positive external force act along the axis definitions shown in Figure 3.1 on page 7 and that the positive pressure and shear forces act in the opposite direction. The sum of forces is for this reason given as the following equation.

$$\vec{F} = \vec{F}_{ext} - \vec{F}_p - \vec{F}_s \tag{3.12}$$

In order to derive the expressions describing the pressure and shear forces an equation of the pressure distribution in the fluid film layer is derived. In order to derive an expression describing the pressure distribution the motion of the fluid film is analysed.

3.2 Fluid motion

The analysis of the fluid motion takes offset in the assumption that the outer radius of the journal is approximately the inner radius of the bushing, as stated below.

$$R \approx r \tag{3.13}$$

This assumption means that the fluid film layer separating the journal and bushing is seen as the equivalent to the fluid film layer between two plates, as seen in Figure 3.2.

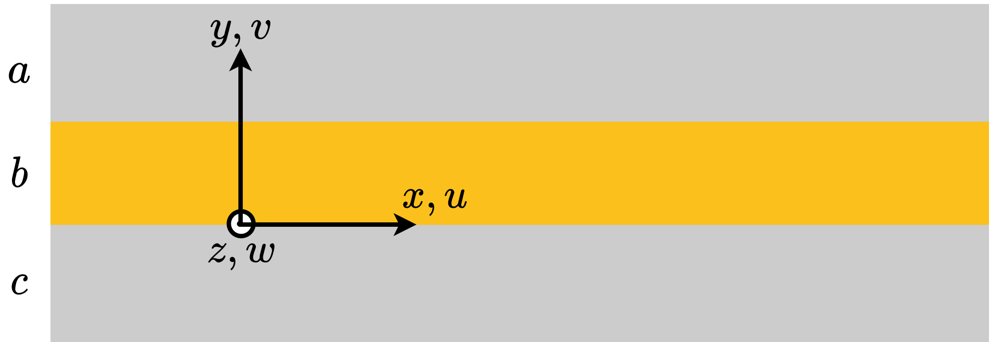

Figure 3.2: Fluid film layer between two plates.

As seen in Figure 3.2 on the previous page the bushing, fluid film layer, and journal are denoted as material a, b, and c, respectively. It is also seen from the figure that an arbitrary (x,y,z) coordinate frame is defined. In this coordinate frame the fluid motion is described by the velocity vector field, (u,v,w), describing fluid velocity in the x-,y-, and z-direction, respectively.

The fluid motion is derived from the Navier-Stokes equations for incompressible Newtonian fluids assuming body forces to be negligible. The Navier-Stokes equations are given in eq. (3.14) to eq. (3.16) and are derived from Cauchy's equation describing moment conservation. [20]

$$\begin{aligned}\rho\left(\frac{\partial u}{\partial t}+u\frac{\partial u}{\partial x}+v\frac{\partial u}{\partial y}+w\frac{\partial u}{\partial z}\right)=&\\ \frac{\partial}{\partial x}\left(-p+2\mu\frac{\partial u}{\partial x}\right)+&\frac{\partial}{\partial y}\left(\mu\left(\frac{\partial u}{\partial y}+\frac{\partial v}{\partial x}\right)\right)+\frac{\partial}{\partial z}\left(\mu\left(\frac{\partial u}{\partial z}+\frac{\partial w}{\partial x}\right)\right)\end{aligned} \tag{3.14}$$

$$\begin{aligned}\rho\left(\frac{\partial v}{\partial t}+u\frac{\partial v}{\partial x}+v\frac{\partial v}{\partial y}+w\frac{\partial v}{\partial z}\right)=&\\ \frac{\partial}{\partial y}\left(-p+2\mu\frac{\partial v}{\partial y}\right)+&\frac{\partial}{\partial x}\left(\mu\left(\frac{\partial u}{\partial y}+\frac{\partial v}{\partial x}\right)\right)+\frac{\partial}{\partial z}\left(\mu\left(\frac{\partial v}{\partial z}+\frac{\partial w}{\partial y}\right)\right)\end{aligned} \tag{3.15}$$

$$\begin{aligned}\rho\left(\frac{\partial w}{\partial t}+u\frac{\partial w}{\partial x}+v\frac{\partial w}{\partial y}+w\frac{\partial w}{\partial z}\right)=&\\ \frac{\partial}{\partial z}\left(-p+2\mu\frac{\partial w}{\partial z}\right)+&\frac{\partial}{\partial x}\left(\mu\left(\frac{\partial u}{\partial z}+\frac{\partial w}{\partial x}\right)\right)+\frac{\partial}{\partial y}\left(\mu\left(\frac{\partial v}{\partial z}+\frac{\partial w}{\partial y}\right)\right)\end{aligned} \tag{3.16}$$

Where ρ is the fluid density and p is the fluid pressure. These equations are simplified by considering the geometric relations of the journal bearing. The geometric relation of interest is the ratio between the normalised fluid film height, h_n, and the normalised fluid plane length, L_n, shown in the equation below.

$$\epsilon_n = \frac{h_n}{L_n} \tag{3.17}$$

The following relation is expected since the fluid film height is assumed to be significantly smaller than the fluid plane length.

$$0 < \epsilon_n << 1 \tag{3.18}$$

The Navier-Stokes expressions are simplified by introducing the following normalised variables, where the subscript n indicates the normalisation point and $^{-}$ indicates the normalised variable.

$$(\bar{x},\bar{y},\bar{z}) = \frac{1}{L_n}\left(x, \frac{1}{\epsilon_n}y, z\right) \tag{3.19}$$

$$\bar{t} = t\frac{U_n}{L_n} \tag{3.20}$$

$$\bar{\rho} = \frac{\rho}{\rho_n} \tag{3.21}$$

$$R_\epsilon = \epsilon_n\, Re_n \tag{3.22}$$

$$(\bar{u},\bar{v},\bar{w}) = \frac{1}{U_n}\left(u, \frac{1}{\epsilon_n}v, w\right) \tag{3.23}$$

$$\bar{\mu} = \frac{\mu}{\mu_n} \tag{3.24}$$

$$Re_n = \left(\frac{\rho_n L_n U_n}{\mu_n}\right) \tag{3.25}$$

$$\bar{p} = R_\epsilon \frac{p}{\rho_n U_n^2} \tag{3.26}$$

Where U_n is the normalised fluid velocity and R_ϵ is the reduced Reynolds number. Inserting these normalised variables into the Navier-Stokes equations, eq. (3.14) to eq. (3.16), the normalised Navier-Stokes equations are derived, given by eq. (3.27) to eq. (3.29).

$$\begin{gathered}\bar{\rho}R_\epsilon\left(\frac{\partial \bar{u}}{\partial \bar{t}}+\bar{u}\frac{\partial \bar{u}}{\partial \bar{x}}+\bar{v}\frac{\partial \bar{u}}{\partial \bar{y}}+\bar{w}\frac{\partial \bar{u}}{\partial \bar{z}}\right)= \\ \frac{\partial}{\partial \bar{x}}\left(-\bar{p}+2\bar{\mu}\epsilon_n^2\frac{\partial \bar{u}}{\partial \bar{x}}\right)+\frac{\partial}{\partial \bar{y}}\left(\bar{\mu}\left(\frac{\partial \bar{u}}{\partial \bar{y}}+\epsilon_n^2\frac{\partial \bar{v}}{\partial \bar{x}}\right)\right)+\epsilon_n^2\frac{\partial}{\partial \bar{z}}\left(\bar{\mu}\left(\frac{\partial \bar{u}}{\partial \bar{z}}+\frac{\partial \bar{w}}{\partial \bar{x}}\right)\right)\end{gathered} \tag{3.27}$$

$$\begin{gathered}\bar{\rho}R_\epsilon\epsilon_n^2\left(\frac{\partial \bar{v}}{\partial \bar{t}}+\bar{u}\frac{\partial \bar{v}}{\partial \bar{x}}+\bar{v}\frac{\partial \bar{v}}{\partial \bar{y}}+\bar{w}\frac{\partial \bar{v}}{\partial \bar{z}}\right)= \\ \frac{\partial}{\partial \bar{y}}\left(-\bar{p}+2\epsilon_n^2\bar{\mu}\frac{\partial \bar{v}}{\partial \bar{y}}\right)+\frac{\partial}{\partial \bar{x}}\left(\bar{\mu}\left(\epsilon_n^2\frac{\partial \bar{u}}{\partial \bar{y}}+\epsilon_n^4\frac{\partial \bar{v}}{\partial \bar{x}}\right)\right)+\frac{\partial}{\partial \bar{z}}\left(\bar{\mu}\left(\epsilon_n^4\frac{\partial \bar{v}}{\partial \bar{z}}+\epsilon_n^2\frac{\partial \bar{w}}{\partial \bar{y}}\right)\right)\end{gathered} \tag{3.28}$$

$$\begin{gathered}\bar{\rho}R_\epsilon\left(\frac{\partial \bar{w}}{\partial \bar{t}}+\bar{u}\frac{\partial \bar{w}}{\partial \bar{x}}+\bar{v}\frac{\partial \bar{w}}{\partial \bar{y}}+\bar{w}\frac{\partial \bar{w}}{\partial \bar{z}}\right)= \\ \frac{\partial}{\partial \bar{z}}\left(-\bar{p}+2\epsilon_n^2\bar{\mu}\frac{\partial \bar{w}}{\partial \bar{z}}\right)+\epsilon_n^2\frac{\partial}{\partial \bar{x}}\left(\bar{\mu}\left(\frac{\partial \bar{u}}{\partial \bar{z}}+\frac{\partial \bar{w}}{\partial \bar{x}}\right)\right)+\frac{\partial}{\partial \bar{y}}\left(\bar{\mu}\left(\epsilon_n^2\frac{\partial \bar{v}}{\partial \bar{z}}+\frac{\partial \bar{w}}{\partial \bar{y}}\right)\right)\end{gathered} \tag{3.29}$$

These equations are simplified by assuming laminar flow and that the thin film approximation is applicable. The thin film approximation is the assumption described by eq. (3.30). [20]

$$\epsilon_n^2 \to 0 \tag{3.30}$$

From these assumptions the reduced Navier-Stokes equations are given by eq. (3.31) to eq. (3.33).

$$\frac{\partial p}{\partial x}=\frac{\partial}{\partial y}\left(\mu\frac{\partial u}{\partial y}\right) \tag{3.31}$$

$$\frac{\partial p}{\partial y}=0 \tag{3.32}$$

$$\frac{\partial p}{\partial z}=\frac{\partial}{\partial y}\left(\mu\frac{\partial w}{\partial y}\right) \tag{3.33}$$

Equation (3.32) shows that the pressure change in the cross film direction, y, is negligible compared to the two other pressure gradients. It is for this reason from heron assumed that the pressure equation is not dependent on the cross film spatial coordinate.

Equation (3.31) is further simplified by the short bearing approximation. The short bearing approximation assumes that pressure driven flow in the circumferential direction, x, is negligible compared to pressure driven flow in the longitudinal direction, z. This assumption is experimentally found to be valid when the ratio between fluid film length and journal diameter is less than one [13]. This assumption results in the following reformulation of eq. (3.31).

$$0=\frac{\partial}{\partial y}\left(\mu\frac{\partial u}{\partial y}\right) \tag{3.34}$$

Since the temperature is spatially dependent and assuming that the viscosity is a function of temperature, the reduced Navier-Stokes equations gives the velocity profiles shown in eq. (3.35) and eq. (3.36).

$$u = \int \frac{1}{\mu} C_{u1}\, dy + C_{u2} \qquad (3.35) \qquad w = \int \frac{1}{\mu} \left(\frac{\partial p}{\partial z} y + C_{w1} \right) dy + C_{w2} \qquad (3.36)$$

Where C_{u1}, C_{u2}, C_{w1}, and C_{w2} are integration constants. These are found from known boundary conditions. It is here assumed that the journal is fixed in the longitudinal direction resulting in the boundary velocity given in the equation below.

$$w(0) = w(h) = 0 \qquad (3.37)$$

The boundary velocities for u is given as the following two equations.

$$u(0) = u_c \qquad (3.38) \qquad u(h) = u_a \qquad (3.39)$$

Inserting these boundary conditions into eq. (3.35) and (3.36) gives the following velocity profiles.

$$u = \frac{u_a - u_c}{\int_0^h \frac{1}{\mu}\, dy} \int_0^y \frac{1}{\mu} ds + u_c \qquad (3.40) \qquad w = \frac{\partial p}{\partial z} \int_0^y \frac{s}{\mu} ds - \frac{\partial p}{\partial z} \frac{\int_0^h \frac{y}{\mu}\, dy}{\int_0^h \frac{1}{\mu}\, dy} \int_0^y \frac{1}{\mu} ds \qquad (3.41)$$

Where s is a substitute variable for y in the integral. The full derivations of the velocity profiles are shown in Appendix A on page 97. These velocity profiles allow for the derivation of an expression describing the pressure distribution within the fluid film layer.

3.3 Pressure distribution

This study is concerned with the performance comparison of a TSO with and without the inclusion of thermoviscous effects. It is for this reason that an equation for both a regular and thermoviscous hydrodynamic pressure distribution are derived.

3.3.1 Regular hydrodynamic lubrication

The pressure distribution derived from regular hydrodynamic lubrication theory is described by the regular Reynolds equation. This equation is derived assuming constant viscosity. This means that the velocity profiles for u and w are given as the following equations.

$$u = \frac{u_a - u_c}{h} y + u_c \qquad (3.42) \qquad w = \frac{\partial p}{\partial z} \frac{1}{\mu} \left(\frac{y^2 - yh}{2} \right) \qquad (3.43)$$

With the velocity profiles there are the problem of three unknowns, w, u, and p, but only two equations and therefore no unique solution is achievable. However, an unique solution is found with the introduction of the continuity equation. The continuity equation is derived from the assumption of mass conservation within the system and is given as eq. (3.44). [20]

$$\frac{\partial \rho}{\partial t} + \frac{\partial}{\partial y} (v\, \rho) + \frac{\partial}{\partial x} (u\, \rho) + \frac{\partial}{\partial z} (w\, \rho) = 0 \qquad (3.44)$$

The deviation of the continuity equation is found in Appendix C on page 103. Assuming that the density is constant with respect to both time and space the continuity equation is simplified to the following equation.

$$\frac{\partial}{\partial y} v + \frac{\partial}{\partial x} u + \frac{\partial}{\partial z} w = 0 \qquad (3.45)$$

The continuity equation introduces one equation to the set but also another unknown variable, v. This problem is solved by integrating the continuity equation in the cross film direction, since the difference between the boundary conditions for v are known. The first term of the cross film integral from eq. (3.45) is given as.

$$\int_0^h \frac{\partial v}{\partial y} dy = v(h) - v(0) = \frac{\partial h}{\partial t} \tag{3.46}$$

The cross film integral of the last two terms in eq. (3.45) are found from Leibnitz's rule for differentiation of integrals given by eq. (3.47). [18, p. 109]

$$\begin{aligned} &\int_{g_1(\alpha)}^{g_2(\alpha)} \frac{\partial}{\partial \alpha} f(\alpha, \beta)\, d\beta = \\ &\frac{\partial}{\partial \alpha}\left(\int_{g_1(\alpha)}^{g_2(\alpha)} f(\alpha, \beta)\, d\beta\right) + f(\alpha, g_1(\alpha))\frac{\partial g_1(\alpha)}{\partial \alpha} - f(\alpha, g_2(\alpha))\frac{\partial g_2(\alpha)}{\partial \alpha} \end{aligned} \tag{3.47}$$

The continuity equation, eq. (3.45), is rewritten to the following equation.

$$\frac{\partial h}{\partial t} + \frac{\partial}{\partial x}\left(\int_0^h u\, dy\right) - u_a \frac{\partial h}{\partial x} + \frac{\partial}{\partial z}\left(\int_0^h w\, dy\right) = 0 \tag{3.48}$$

Inserting the velocity profiles into this equation and solving for the pressure gradient, the following equation is derived.

$$\frac{\partial^2 p}{\partial z^2} = \frac{6\mu}{h^3}\left((u_c - u_a)\frac{\partial h}{\partial x} + 2\frac{\partial h}{\partial t}\right) \tag{3.49}$$

The above differential equation is solved by assuming that the pressure has known boundary conditions. It is assumed that the pressure at each end of the journal bearing is constant with regards to space and is given as p_0 and p_L and the fluid film length is given as L. This assumption leads to the following equation.

$$p = \frac{6\mu}{h^3}\left((u_c - u_a)\frac{\partial h}{\partial x} + 2\frac{\partial h}{\partial t}\right)\frac{(z^2 - z\,L)}{2} + \frac{(p_L - p_0)\,z}{L} + p_0 \tag{3.50}$$

The expressions describing the boundary conditions of u are found by placing the origin of the xyz-coordinate frame, presented in Figure 3.2 on page 9, on the circumference of the journal. With this definition the circumferential movement of the bushing is stationary with respect to the coordinate frame. The coordinate frame is placed such that the positive x-axis direction is aligned with the direction of the positive rotation of the journal. The following two boundary condition for u is then given as seen below.

$$u_a = 0 \tag{3.51}$$

$$u_c = \omega r \tag{3.52}$$

With the above definition of the xyz-coordinate frame it is seen an arbitrary angle in the $\alpha\beta$-frame, described by x, relates to an angle in the ab-frame, described by ϕ, by the following equation.

$$\phi = \frac{x}{r} - \theta \tag{3.53}$$

Using this formulation of the angle ϕ the fluid film height is given as seen below.

$$h = C_r - \epsilon\, cos\left(\frac{x}{r} - \theta\right) \tag{3.54}$$

Inserting eq. (3.51), eq. (3.52), and eq. (3.54) into eq. (3.50) the following expression is derived.

$$p_R = \frac{12\mu}{h^3}\left(sin(\phi)\;\epsilon\left(\frac{\omega}{2}-\theta\right) - cos(\phi)\dot{\epsilon}\right)\frac{z^2-Lz}{2} + \frac{(p_L-p_0)z}{L} + p_0 \tag{3.55}$$

Where p_R describes the pressure in a fluid film layer following the general derivation of the Reynolds equation using the short bearing approximation and assuming constant density and viscosity.

3.3.2 Thermoviscous hydrodynamic lubrication

The thermoviscous pressure distribution equation is derived from Reynolds viscosity model, given by eq. (3.56) [7].

$$\mu_r = \frac{1}{\delta} = a_r\, e^{-b_r\, T} \tag{3.56}$$

Where a_r and b_r are fluid parameters and δ is the fluidity. Reynolds viscosity model is chosen due to its simplicity.

The temperature distribution within the fluid film is described by eq. (3.57). This equation is derived from the constraint of energy conservation within the fluid film layer. [20]

$$\rho\, C\left(\frac{\partial T}{\partial t} + \frac{\partial T}{\partial x}u + \frac{\partial T}{\partial y}v + \frac{\partial T}{\partial z}w\right) = \lambda\left(\frac{\partial^2 T}{\partial x^2} + \frac{\partial^2 T}{\partial y^2} + \frac{\partial^2 T}{\partial z^2}\right) + \mu\Phi \tag{3.57}$$

Where λ it the thermal conductivity. C is the specific heat capacitance. Φ is the viscous dissipation function and for incompressible fluids this is given by eq. (3.58). [20]

$$\begin{aligned}\Phi = 2&\left(\left(\frac{\partial u}{\partial x}\right)^2 + \left(\frac{\partial v}{\partial y}\right)^2 + \left(\frac{\partial w}{\partial z}\right)^2\right)\\ &+\left(\frac{\partial u}{\partial y} + \frac{\partial v}{\partial x}\right)^2 + \left(\frac{\partial v}{\partial z} + \frac{\partial w}{\partial y}\right)^2 + \left(\frac{\partial w}{\partial x} + \frac{\partial u}{\partial z}\right)^2\end{aligned} \tag{3.58}$$

The viscous dissipation function is simplified by normalising it with the same normalised variables as described in eq. (3.19) to eq. (3.26). This normalisation results in the following expression.

$$\begin{aligned}\Phi = \frac{U_n^2}{L_n^2}&\left(2\left(\left(\frac{\partial \bar{u}}{\partial \bar{x}}\right)^2 + \left(\frac{\partial \bar{v}}{\partial \bar{y}}\right)^2 + \left(\frac{\partial \bar{w}}{\partial \bar{z}}\right)^2\right)\right.\\ &\left.+\left(\frac{\partial \bar{u}}{\partial \bar{y}}\frac{1}{\epsilon_n} + \frac{\partial \bar{v}}{\partial \bar{x}}\epsilon_n\right)^2 + \left(\frac{\partial \bar{v}}{\partial \bar{z}}\epsilon_n + \frac{\partial \bar{w}}{\partial \bar{y}}\frac{1}{\epsilon_n}\right)^2 + \left(\frac{\partial \bar{w}}{\partial \bar{x}} + \frac{\partial \bar{u}}{\partial \bar{z}}\right)^2\right)\end{aligned} \tag{3.59}$$

It is seen that this equation is greatly reduced when only considering the terms divided by ϵ_n, since these are considered dominant due to the thin film approximation, eq. (3.30). This approximation results in the following reduced viscous dissipation function.

$$\bar{\Phi} = \frac{U_n^2}{L_n^2\epsilon_n^2}\left(\left(\frac{\partial \bar{u}}{\partial \bar{y}}\right)^2 + \left(\frac{\partial \bar{w}}{\partial \bar{y}}\right)^2\right) \tag{3.60}$$

This equation is further simplified by assuming that the journal's rotation drives a significantly larger flow in the circumferential direction compared to the longitudinal direction resulting in the following equation.

$$\bar{\Phi} = \frac{U_n^2}{L_n^2\epsilon_n^2}\left(\frac{\partial \bar{u}}{\partial \bar{y}}\right)^2 \tag{3.61}$$

Equation (3.57) is normalised by further introducing the normalised temperature, given by eq. (3.62).

$$\bar{T} = \frac{T}{T_n} \tag{3.62}$$

This results in eq. (3.63).

$$\frac{\rho_n C_n T_n U_n}{L_n}\left(\frac{\partial \bar{T}}{\partial \bar{t}} + \underbrace{\frac{\partial \bar{T}}{\partial \bar{x}}\bar{u} + \frac{\partial \bar{T}}{\partial \bar{y}}\bar{v} + \frac{\partial \bar{T}}{\partial \bar{z}}\bar{w}}_{Convection}\right) = \frac{\lambda_n T_n}{L_n^2}\left(\underbrace{\frac{\partial^2 \bar{T}}{\partial \bar{x}^2} + \frac{\partial^2 \bar{T}}{\partial \bar{y}^2}\frac{1}{\epsilon_n^2} + \frac{\partial^2 \bar{T}}{\partial \bar{z}^2}}_{Conduction}\right) + \mu_n \bar{\mu}\bar{\Phi} \tag{3.63}$$

Considering the conduction term of eq. (3.63) it is seen that the dominating term becomes conduction in the cross film direction, it is for this reason that the other two conduction terms are neglected. From the convection terms, it is assumed that convection in the cross film direction can be neglected. This is assumed since the flow in circumferential and longitudinal direction is expected to be significantly larger than flow in the cross film direction. Furthermore, the transient period of the temperature is neglected since the purpose of the model is to be included in a TSO that has significantly smaller sampling time than the expected rate of change of the temperature, with respect to time. In order to reduce the equation further the reduced Brinkman and Eckert number is introduced, given in the equations below.

$$Br_n = \frac{\mu_n U_n^2}{\lambda_n T_n} \tag{3.64}$$

$$Ec_n = \frac{U_n^2}{C_n T_n} \tag{3.65}$$

With the above assumptions and normalised variables eq. 3.63 becomes eq. (3.66).

$$Br_n \frac{R_\epsilon}{Ec_n}\left(\frac{\partial \bar{T}}{\partial \bar{x}}\bar{u} + \frac{\partial \bar{T}}{\partial \bar{z}}\bar{w}\right) = \frac{\partial^2 \bar{T}}{\partial \bar{y}^2} + Br_n \bar{\mu}\left(\frac{\partial \bar{u}}{\partial \bar{y}}\right)^2 \tag{3.66}$$

In the paper Johansen et al. [11] it is proposed to use perturbation theory with the reduced Brinkman number, Br_n, as the perturbative parameter in order to solve eq. (3.66). It is seen that this method is equivalent to introducing the perturbative parameter, K, in the non-normalised equation, eq. (3.67), on the corresponding terms that Br_n is multiplied on.

$$K\,\frac{\rho C}{\lambda}\left(\frac{\partial T}{\partial x}u + \frac{\partial T}{\partial z}w\right) = \frac{\partial^2 T}{\partial y^2} + K\,\frac{\mu}{\lambda}\left(\frac{\partial u}{\partial y}\right)^2 \tag{3.67}$$

The solution to eq. (3.67) is found from rewriting the equation to become a function of fluidity which is achieved by solving for the temperature in eq. (3.56) and inserting this into eq. (3.67). Furthermore the velocity profiles for u, eq. 3.40 on page 12, and w, eq. 3.41 on page 12, are inserted and rewritten to be a function of fluidity instead of viscosity. The approximation of the solution is assumed to follow a perturbation series defined as the following equation.

$$\delta = \sum_{n=0}^{\infty} \delta_n\, K^n \tag{3.68}$$

This project is only concerned with the approximation of the zeroth and first order coefficients, since it is found that these two coefficients can describe the temperature in a journal bearing to a satisfying degree [11]. The unperturbed problem is found when the perturbative parameter is set to zero as stated in the equation below.

$$K = 0 \tag{3.69}$$

The zeroth order coefficient is the solution to the unperturbed problem, given in the equation below. [2]

$$-\frac{\partial^2 \delta}{\partial y^2} + \left(\frac{\partial \delta}{\partial y}\right)^2 = 0 \tag{3.70}$$

The solution to this equation is found by assuming known boundary conditions for δ. In order to greatly simplify this expression it is assumed that the journal bearing has an equivalent temperature, T_{eq}, that describes the fluidity at both boundaries. The equivalent temperature is time dependent, but it is assumed to be constant with regards to the spatial coordinates. The solution to eq. (3.70) is from these assumption found as the following equation.

$$\delta_0 = \delta_b\left(T_{eq}\right) \tag{3.71}$$

Where $\delta_b(T_{eq})$ is the boundary fluidity as a function of the equivalent journal bearing temperature.

The first order coefficient is found by inserting the perturbation series into eq. (3.67) and matching the coefficient for n'th order of K on both sides of the equation. The first order coefficient is found to be given as the following equation.

$$\delta_1 = -b_r \frac{(u_a - u_c)^2\, y(y-h)}{\lambda\, 2\, h^2} \tag{3.72}$$

An approximation of the fluidity is from this analysis found to be given as the following equation when the perturbative parameter is equal to one.

$$\delta \approx \delta_0 + K\,\delta_1 = \delta_b - \; b_r \frac{(u_a - u_c)^2\, y(y-h)}{\lambda\, 2\, h^2} \tag{3.73}$$

The viscosity is the inverse fluidity as stated in eq. (3.56) which results in the following rewriting of the above equation.

$$\mu = \frac{2h^2\lambda}{2\delta_b h^2\lambda + b_r\, y(u_a - u_c)^2 h - b_r y^2 (u_a - u_c)^2} \tag{3.74}$$

The equation above allows for solving the velocity profiles, eq. (3.40) and eq. (3.41). With a deterministic expression for the velocity profiles the pressure distribution in the fluid film layer is solvable by the introduction of the continuity equation, eq. (3.48). Solving for the pressure gradient in the continuity equation, the following expression is derived.

$$\frac{\partial^2 p}{\partial z^2} = 60\, \frac{\lambda\left(\left(\frac{d}{dx}u_a\right)h - u_a\frac{\partial}{\partial x}h + u_c\frac{\partial}{\partial x}h + \left(\frac{d}{dx}u_c\right)h + 2\,\frac{\partial}{\partial t}h\right)}{h^3\left(u_a^2 b_r - 2\,u_a u_c b_r + u_c^2 b_r + 10\,\delta_b\lambda\right)} \tag{3.75}$$

Assuming known boundary condition for the pressure and inserting the fluid film height and boundary condition for u the following expression for the pressure distribution is derived.

$$p_T = \frac{60\lambda\left(z^2 - L\,z\right)\left(\left(\frac{\omega}{2} - \dot{\theta}\right)\epsilon\, sin(\phi) - \dot{\epsilon} cos(\phi)\right)}{\left(\omega^2\, r^2\, b_r + 10\delta_b\lambda\right)h^3} + \frac{(p_L - p_0)z}{L} + p_0 \tag{3.76}$$

Where p_T describes the pressure distribution in the fluid film layer when including thermoviscous effects.

3.4 Pressure force

The pressure force is found by integrating the previously found pressure distribution equations across the contact surface of the journal. However, both the regular hydrodynamic and thermoviscous pressure equation, eq. (3.55) and eq. (3.76), respectively, describes the pressure in ideal fluids. This means that both equations can give negative absolute pressures. This is assessed to be an invalid representation of the pressure in the journal bearing since an impure oil has air cavitations that counteracts negative fluid pressure. It is assumed that due to this effect, more realistic pressure force equations are obtained by only integrating the contact surface of the journal with a corresponding positive pressure. In order to derive this area the pressure equations are restructured to the following expression.

$$p = G\left(\vec{V_1} \cdot \vec{V_2}\right) + p_{off} \tag{3.77}$$

It is seen that both eq. (3.55) and eq. (3.76) are described by eq. (3.77) if the terms are described by the following equations.

$$p_{off} = \frac{(p_L - p_0)z}{L} + p_0 \tag{3.78}$$

$$\vec{V_1} = \begin{bmatrix} -\dot{\epsilon} \\ \epsilon\left(\frac{\omega}{2} - \dot{\theta}\right) \end{bmatrix} \tag{3.79}$$

$$\vec{V_2} = \begin{bmatrix} cos(\phi) \\ sin(\phi) \end{bmatrix} \tag{3.80}$$

The regular Reynolds pressure equation has G given by the following equation.

$$G_R = \frac{6\mu\left(z^2 - Lz\right)}{h^3} \tag{3.81}$$

The thermoviscous pressure equation has G given by the following equation.

$$G_T = \frac{60\lambda\left(z^2 - zL\right)}{\left(\omega^2 r^2 b_r + 10\delta_b\lambda\right)h^3} \tag{3.82}$$

The apparent advantageous part of rewriting the pressure equations is that it is possible to rewrite the dot product between the two vectors with the following relation.

$$\vec{V_1} \cdot \vec{V_2} = |\vec{V_1}|\,|\vec{V_2}|cos(\phi - \psi) \tag{3.83}$$

Where ψ is the angle of the pressure state vector $\vec{V_1}$, given by the following equation.

$$\psi = tan^{-1}\left(\frac{\epsilon\left(\frac{\omega}{2} - \dot{\theta}\right)}{-\dot{\epsilon}}\right) \tag{3.84}$$

Since $|\vec{V_2}|$ is equal to one, the pressure equation, eq. 3.77, is given by the following equation.

$$p = G\,|\vec{V_1}|cos\left(\phi - \psi\right) + p_{off} \tag{3.85}$$

The problem of finding the area with positive pressure then becomes a problem of solving the above equation for ϕ when $p = 0$. However, the solution to this is not trivial since the fluid film height also is a function of ϕ. The solution is greatly simplified when assuming that p_{off} is negligible. The solution then becomes the points where the sine term is equal to zero, since G_R and G_T do not change polarity. This is satisfied when ϕ is equal to the following equation.

$$\phi = \psi \pm \frac{\pi}{2} \tag{3.86}$$

The integration limits are as given in the following equation due to the negative polarity of the G terms.

$$F_{pa} = \int_0^L \left(\int_{\psi_i - \frac{\pi}{2}}^{\psi_i + \frac{\pi}{2}} p\, cos(\phi)\, d\phi \right) r\, dz \tag{3.87}$$

$$F_{pb} = \int_0^L \left(\int_{\psi_i - \frac{\pi}{2}}^{\psi_i + \frac{\pi}{2}} p\, sin(\phi)\, d\phi \right) r\, dz \tag{3.88}$$

Where ψ_i is given by the following equation.

$$\psi_i = \psi + \pi \tag{3.89}$$

In the pressure force equations the sine terms are included in order to account for the direction of the pressure forces in the ab-frame.

3.5 Shear Force

The shear force is found from the shear stress between fluid layers in Newtonian fluids, given by the following equation.

$$\tau = \mu \frac{\partial u}{\partial y} \tag{3.90}$$

As previously mentioned, movement in the longitudinal direction is neglected and it is therefore only of interest to find the shear forces caused by shear stress in the circumferential direction, as seen in the equation above. Since both μ and u is derived previously, these are inserted into the shear stress equation and evaluated at the surface of the journal, and integrated across the contact surface of the journal.

$$F_{sa} = -\int_0^L \left(\int_0^{2\pi} \tau|_{y=0}\, cos\left(\phi + \frac{\pi}{2}\right)\, d\phi \right) r\, dz \tag{3.91}$$

$$F_{sb} = -\int_0^L \left(\int_0^{2\pi} \tau|_{y=0}\, sin\left(\phi + \frac{\pi}{2}\right)\, d\phi \right) r\, dz \tag{3.92}$$

It is for these equations notable that the polarity is changed since the shear stress equation describes the shear stress in the fluid film layer and the shear force of interest is that affecting the journal. Furthermore, the sine-terms are included in order to account for the direction of the shear forces in the ab-frame where $\frac{\pi}{2}$ is added since the shear force are tangential to the contact surface.

3.6 Steady state validation

The two analytical models are validated by comparing them to the G.B. DuBois and F.W. Ocvirk S.S. solution presented in Section 2.2 on page 4. The simulation of the models are performed for a step in the external force, with different magnitudes. The simulation parameters are seen in Table 3.1 on the facing page.

Table 3.1: Fluid parameter used for the simulation evaluated at 313.15 K.

ω	λ [5]	b_r [3]
100π rad/s	$0.142\ \frac{\mathrm{W}}{\mathrm{m\,K}}$	$31 \cdot 10^{-3}\ \mathrm{K}^{-1}$

The fluid viscosity and boundary fluidity is found from Vogels viscosity model, eq. (2.1) on page 3, at 313.15 K. The results is seen in Figure 3.3.

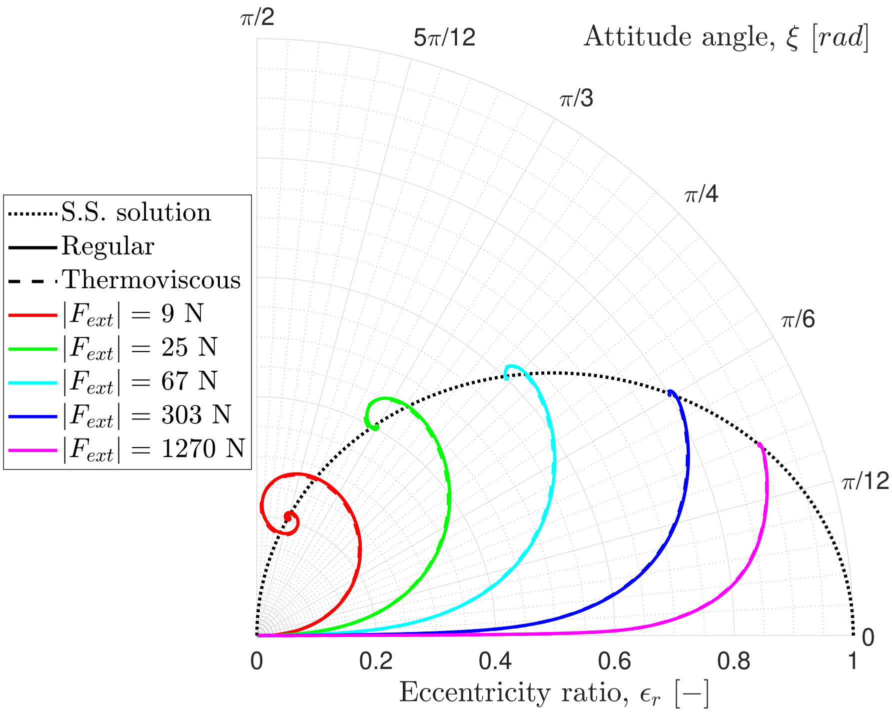

Figure 3.3: S.S. solutions of the analytical models compared to G.B. DuBois and F.W. Ocvirk at different external loads in the alpha direction.

It is seen that both the regular hydrodynamic and thermoviscous model settles at the S.S. solution. It is notable that the journal bearing starts to overshoot at low loads. These overshoots are enhanced even further at lower external forces than have been depicted on the figure. It is found that when the ratio between external force and angular velocity of decreases the overshoot increases, and eventually reaches a point where the models do not reach S.S., referred to as the oil whirl phenomena. The models are seen to follow the same trajectory for a journal angular velocity of 100π rad/s. This similarity of the models is investigated in the following section.

3.7 Difference between the two pressure models

The pressure equations for both the regular hydrodynamic, eq. (3.55), and the thermoviscous model, eq. (3.76), is seen to only deviate in the G-terms presented in Section 3.4 on page 17 and these are given below.

$$G_R = 6\mu \frac{\left(z^2 - Lz\right)}{h^3} \qquad (3.93) \qquad G_T = \frac{60\lambda}{\left(\omega^2 r^2 b_r + 10\delta_b\lambda\right)} \frac{\left(z^2 - Lz\right)}{h^3} \qquad (3.94)$$

It is found that these terms equate when the viscosity term from the regular hydrodynamic model is given by the following equation.

$$\mu = \frac{10\,\lambda}{\omega^2\, r^2\, b_r + 10\,\delta_b\,\lambda} \tag{3.95}$$

Assuming that the shear forces are negligible compared to the pressure forces, it is from this seen that the only difference between the two models corresponds to a change in the viscosity term. It is from this equation seen that if μ and δ_b is found at the same temperature, the difference increases the further the angular velocity is from zero.

The difference between the eccentricity from the two models are seen in the following figure for an angular journal velocity of 250 rad/s, 500 rad/s, 750 rad/s, and 1000 rad/s.

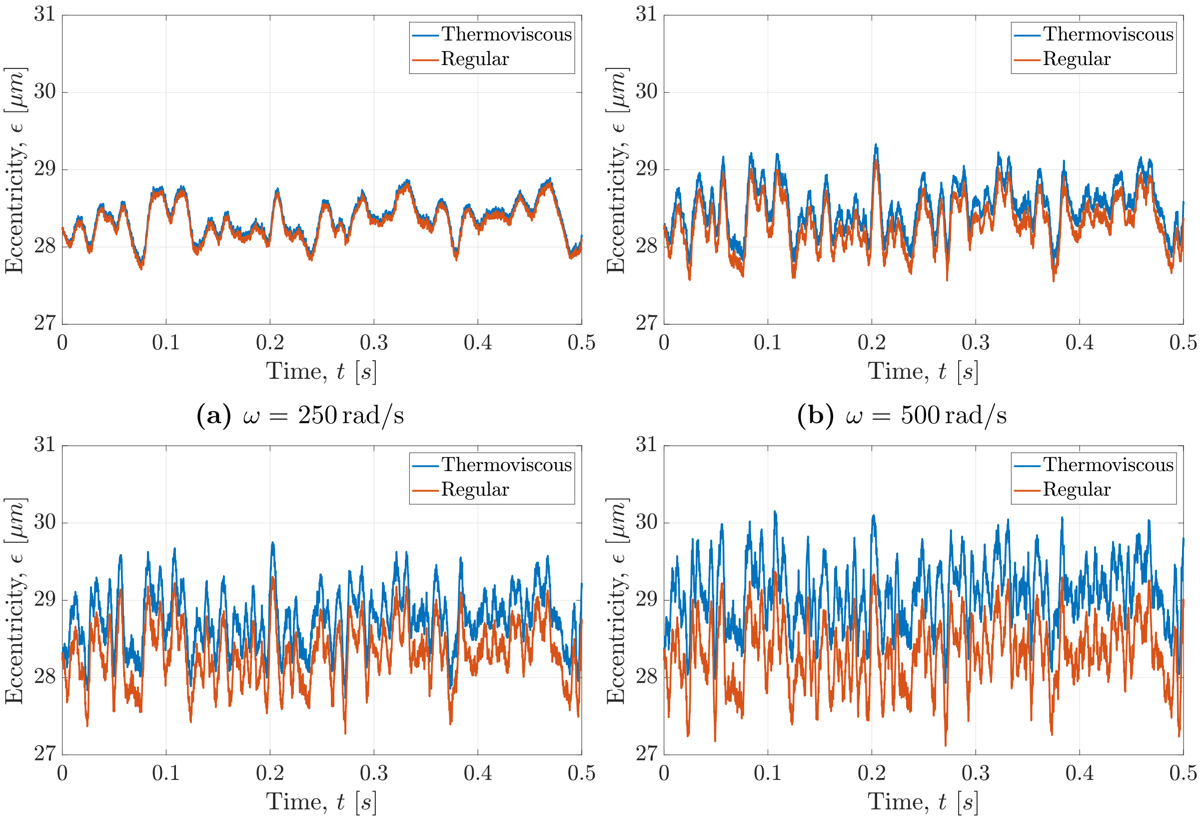

(a) $\omega = 250\,\text{rad/s}$ **(b)** $\omega = 500\,\text{rad/s}$

(c) $\omega = 750\,\text{rad/s}$ **(d)** $\omega = 1000\,\text{rad/s}$

Figure 3.4: Comparison of the analytical models at different journal angular velocities.

In the figure, the force is varied as a random binary signal between the forces corresponding to an eccentricity ratio of 35 % and 65 %, calculated from the load number, eq. (2.2). At these eccentricity ratios the shear force is negligible compared to the pressure force. The figure shows that the difference in the pressure expressions result in a close to constant offset between the eccentricity of the models.

It is from this analysis found that both analytical hydrodynamic lubrication models fit the experimentally verified S.S. solutions presented by G.B. DuBois and F.W. Ocvirk. The models are however not verified with respect to the dynamics, and it is for this reason of interest to investigate this.

4 Virtual experimental setup

In order to validate the dynamics of the analytical journal bearing models and test the TSO strategies, virtual experiments are conducted. The virtual experiments aim to include less assumptions and additional physics compared to the analytical models. The virtual experiments are conducted in the software COMSOL Multiphysics. COMSOL utilises numerical solvers, where it is possible to perform different studies such as time dependent and S.S.

4.1 Simulation strategy

The simulations are performed using the S.S. solutions as the initial conditions for the time dependent solver. The reason for using a time dependent solver is to validate the dynamics of the analytical journal bearing models. Furthermore, the test of the TSO is based upon the TSO strategies' ability to track the mechanical dynamics. The reason for using the S.S. solution as the initial condition is that the thermodynamics in the solids are not of interest in the TSO test, since the mechanical dynamics estimated in the TSO are found to be much faster than the thermodynamics of the solids.

4.2 Material properties

The journal bearing structure consists of a journal, fluid film layer, and bushing. The material used for the fluid film layer, is assumed to be hydraulic oil. The material used for both the bushing and journal are assumed to be AISI 4340 steel.

4.2.1 Hydraulic oil

The material properties of the hydraulic oil used in the virtual experiments are dynamic viscosity, density, specific heat capacity, and thermal conductivity.

Dynamic viscosity

In the virtual experiment the dynamic viscosity is modelled as both temperature and pressure dependent, using a reduced Barus-Vogel viscosity model, given as below. [7]

$$\mu_{bv} = a_{bv}\, e^{A(T)}\, e^{B(T,p)} \qquad A(T) = \frac{b_{bv}}{T - c_{bv}} \qquad B(T,p) = \frac{p}{a_{1,bv} + a_{2,bv}\,(T - 273.15\,[K])} \tag{4.1}$$

The parameters used in this equation are shown in Table 4.1.

Table 4.1: Barus-Vogel model parameters. [7]

a_{bv}	b_{bv}	c_{bv}	$a_{1,bv}$	$a_{2,bv}$
$63.34\,\mu$Pa s	879.8 K	177.8 K	33.4 MPa	325.6 $\frac{\text{kPa}}{\text{K}}$

This viscosity model is shown to be representative up to a fluid pressure of 40 MPa [7]. The viscosity model is seen in Figure 4.1 on the following page as a function of temperature at five different pressure levels.

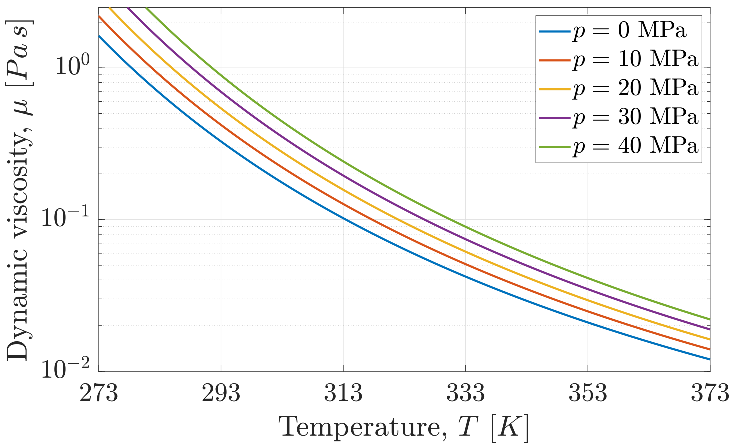

Figure 4.1: Dynamic viscosity with respect to temperature and pressure.

It is seen from the figure that an increase in the fluid pressure leads to an increase in the dynamic viscosity. It is also seen that an increase in temperature leads to a decrease in dynamic viscosity. Furthermore, the fluid pressure dependency of the dynamic viscosity is seen to decrease as the temperature increases.

Density

In the virtual experiments the density of the hydraulic oil, ρ_b, is modelled as temperature dependent and is given by the following equation. [10]

$$\rho_b = \frac{q_1}{1 + q_2\ (T - q_3)} \tag{4.2}$$

Where the parameters are given in Table 4.2.

Table 4.2: Density model parameters. [10]

q_1	q_2	q_3
$888\,\frac{\mathrm{kg}}{\mathrm{m}^3}$	$0.7 \cdot 10^{-3}\,\frac{1}{\mathrm{K}}$	$293.2\,\mathrm{K}$

The density model is depicted in Figure E.1b in Appendix E on page 109.

Specific heat capacity

In the virtual experiments the specific heat capacity, C_b, is modelled as temperature dependent. This model is found in the COMSOL material library under engine oil and described by the following equation.

$$C_b = q_1 + q_2\,T + q_3\,T^2 \tag{4.3}$$

Where the parameters are given in Table 4.3.

Table 4.3: Specific heat capacity model parameters. [5]

q_1	q_2	q_3
$761.4\,\frac{\mathrm{J}}{\mathrm{Kg\,K}}$	$3.477\,\frac{\mathrm{J}}{\mathrm{kg\,K^2}}$	$1.155\,\frac{\mathrm{mJ}}{\mathrm{kg\,K^3}}$

The expression for the specific heat capacity is deemed valid between 273 K and 433 K and is depicted in Figure E.1c in Appendix E on page 109. [5]

Thermal conductivity

In the virtual experiments the thermal conductivity, λ_b, is modelled as temperature dependent. The thermal conductivity model is also found in the COMSOL material library under engine oil and is described by the following equation.

$$\lambda_b = q_1 - q_2\,T + q_3\,T^2 \tag{4.4}$$

Where the parameters are given in Table 4.4.

Table 4.4: Parameters used for thermal conductivity. [5]

q_1	q_2	q_3
$192.2\frac{\text{mW}}{\text{m K}}$	$206.4\,\frac{\mu\text{W}}{\text{m K}^2}$	$154.2\,\frac{\text{nW}}{\text{m K}^3}$

The expression for the thermal conductivity is deemed valid between 273 K and 433 K and is depicted in Figure E.1d in Appendix E on page 109. [5]

4.2.2 Steel, AISI 4340

The specific heat capacity, C_a, density, ρ_a, and thermal conductivity, λ_a, for steel is found in the COMSOL material library under steel AISI 4340 [5]. These properties are given in table 4.5.

Table 4.5: The material properties of steel in the virtual experiment. [5]

C_a	ρ_a	λ_a
$475\frac{\text{J}}{\text{kg}\cdot\text{K}}$	$7850\frac{\text{kg}}{\text{m}^3}$	$44.5\frac{\text{W}}{\text{m}\cdot\text{K}}$

4.3 Physics in the virtual experiment

The virtual experiment includes hydro-, mechanical-, and thermodynamics.

4.3.1 Hydrodynamics

The pressure distribution in the fluid film is simulated using COMSOL's "Thin-Film Flow, Shell" module. The module takes offset in the Navier-Stokes equations with the thin film approximation and the continuity equation as in the derivation of the analytical hydrodynamic lubrication models in Section 3.2 on page 9. This means that the fluid pressure is assumed constant in the cross film direction. It is notable that in the virtual experiments the fluid pressure distribution is solved without the short bearing approximation used for the analytical expressions. The COMSOL module uses the average velocity fields with regards to the cross film direction. The average velocity field, eq. 4.5, and continuity equation, eq. 4.6 on the following page, are given by the following equations.

$$\vec{v}_{ave} = \frac{1}{2}(\vec{v}_a + \vec{v}_c) - \frac{h^2}{12\mu}\nabla_t p \tag{4.5}$$

$$\frac{\partial}{\partial t}(\rho\, h) + \nabla\left(\rho\, \vec{v}_{ave}\, h\right) = 0 \tag{4.6}$$

Where $\vec{v}_a$ and $\vec{v}_c$ are the boundary velocities of the bushing and journal, respectively. Furthermore, in order to solve the equation the boundary pressure at both ends of the fluid film are defined.

The fluid forces in the virtual experiments are derived using the velocity profiles derived from the Navier-Stokes equations, eq. (3.31) and eq. (3.33), assuming the viscosity is constant with regards to the cross film direction. The fluid stresses on the journal are given as the following two equation for the α- and β-direction, assuming no-slip condition.

$$f_\alpha = -\frac{h}{2}\frac{dp}{d\alpha} + \mu\frac{\vec{v}_{a,\alpha} - \vec{v}_{c,\alpha}}{h} + p_f\, \vec{n}_\alpha \tag{4.7}$$

$$f_\beta = -\frac{h}{2}\frac{dp}{d\beta} + \mu\frac{\vec{v}_{a,\beta} - \vec{v}_{c,\beta}}{h} + p_f\, \vec{n}_\beta \tag{4.8}$$

Where p_f is the non-negative fluid pressure, assuming the negative pressure from p is equal to zero. $\vec{n}$ is the normal vector defined such that it points towards the centre of the journal where the subscript indicates the component in a given direction.

By integrating the fluid stress across the contact surface of the journal, the fluid forces in the α- and β-direction are found, defined as F_α and F_β, respectively.

4.3.2 Mechanical dynamics

In the virtual experiments the mechanical dynamics are modelled using Newton's second law as described in eq. (4.9).

$$\begin{bmatrix} \ddot{\alpha} \\ \ddot{\beta} \end{bmatrix} = \frac{1}{m}\left(\begin{bmatrix} F_{ext,\alpha} \\ F_{ext,\beta} \end{bmatrix} + \begin{bmatrix} F_\alpha \\ F_\beta \end{bmatrix} \right) \tag{4.9}$$

To solve eq. (4.9) in COMSOL the "Global ODEs and DAEs" module is used. To solve the equation an initial position and velocity are given.

4.3.3 Thermodynamics in the fluid film

The heat transfer in the fluid film is simulated using COMSOL's "Heat Transfer in Films" module. The heat transfer is modelled using the thermally thin film approximation which is applied due to computational difficulties. This approximation means that the temperature does not change in the cross film direction. The heat transfer equation, (4.10), is derived from the constraint of energy conservation, as described by eq. (3.57) in Section 3.3.2 on page 14.

$$\rho\, C\left(\frac{\partial T}{\partial t} + \vec{v}\cdot\nabla_t T_f\right) - \nabla_t\cdot\left(\lambda \nabla_t T_f\right) = Q_f \tag{4.10}$$

T_f is the temperature of the fluid film. Q_f describes the heat source that is applied to the fluid film. This includes the heat flux from the boundary conditions and the viscous dissipation calculated in the the "Thin film flow, shell" module, using the reduced but non-normalised viscous dissipation function, eq. (3.60) from Section 3.3.2 on page 14. In the equation the subscript t on ∇ refers to the coordinate components, tangential to the surface.

The heat transfer at the boundary of the fluid film is modelled using Dirichlet boundary conditions. The temperature boundary condition of the fluid film is assumed to be equal to the adjacent surfaces and both edges are assumed to have the same temperature as the journal for the adjacent nodes.

The thermal field in the fluid layer is set to move with the average velocity profiles found in the "Thin-Film Flow, Shell" module.

4.3.4 Thermodynamics in the solids

The heat transfer in the solids are simulated using COMSOL's "Heat Transfer in Solids" module. The heat transfer in solids are modelled in a similar manner as the "Heat Transfer in Films" with eq. (4.10), where ∇ is used instead of ∇_t. In the simulation heat transfer from radiation is assumed negligible.

In order to account for the rotation of the journals thermal fields, the "Translational Motion" attribute has been added to the model.

The boundary conditions for the journal bearing is split into five regions, as seen in Figure 4.2.

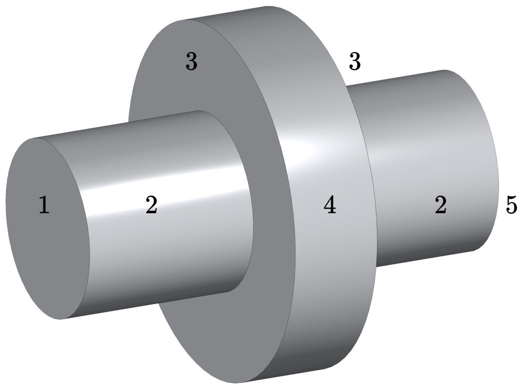

Figure 4.2: Boundary regions of the journal bearing.

All the boundary regions, except the first, shown in Figure 4.2 is designed to be in contact with air at a temperature of 293 K and atmospheric pressure.

Boundary region 1

The first boundary region is located at the end of the journal where a Dirichlet boundary condition is applied. At the boundary condition the temperature is set equal to 293 K. This boundary condition is chosen to simulate that the journal is connected to a large machine that is capable of maintaining a constant temperature due to a large thermal mass.

Boundary region 2

The second boundary region is located at the circumference of the journal excluding the area in contact with the fluid film. The boundary condition is designed to be a Neumann boundary condition where COMSOL is calculating the heat flux based on the temperature difference of the boundary and the external air temperature of 293 K. The heat transfer coefficient is calculated by COMSOL as the average heat transfer coefficient from a plate with forced convection, due to the relative air speed caused by the rotating journal. The air speed is calculated as the rotational speed multiplied with the radius of the journal. The plate length is assumed to be equal to the circumference of the journal.

Boundary region 3

The third boundary region is located on the sides of the bushing, where the boundary condition is designed to be a Neumann boundary condition. In this region the heat transfer coefficient is calculated based on vertical natural convection, as the bushing is fixed.

Boundary region 4

The fourth boundary region is on the outer circumference of the bushing, where the Neumann boundary condition is applied. The heat transfer coefficient is calculated based on natural convection from a horizontal cylinder, with the same diameter as the bushing.

Boundary region 5

The fifth boundary region is located at the opposite end of the journal compared to the first boundary region. The boundary is designed with the Neumann boundary condition, to be the average heat coefficient for a plate with force convection applied. The air speed is set to half the rotational speed multiplied with the journal radius. This air speed is chosen to half the rotational speed as the relative speed between the journal and air changes as the radius is increased. Furthermore, the plate length is assumed to be the circumference of a journal with half the radius.

4.4 Meshing and relative tolerance

To ensure the numerical solver in COMSOL is calculating with a sufficient accuracy and with a reasonable computational time, the relative tolerance and the mesh density is swept. In the virtual experiments the relative tolerance is used as the convergence criteria.

4.4.1 Strategy for determining the relative tolerance and mesh density

As discussed previously both a time dependent and S.S. solver is used for the virtual experiments. Each solver uses its own relative tolerance, but both solver uses the same mesh. The mesh convergence is determined using the S.S. solver, since this is a more time efficient method compared to using a time dependent solver. [6]

The relative tolerance for the S.S. solver is determined first. This is determined with a relative large mesh density. When convergence of the relative tolerance for the S.S. solver is found, it is possible to determine the convergence of the mesh density.

The mesh convergence study is performed by sweeping the maximum length between the mesh nodes, meaning that the COMSOL algorithm is able to reduce the mesh length even further. The mesh is split into a fluid film region and a solid region, as seen in Figure 4.3 on the next page, to improve the computational time of the model. This is due to the mesh density of the fluid film region is required to be significantly larger than that needed in the solid region.

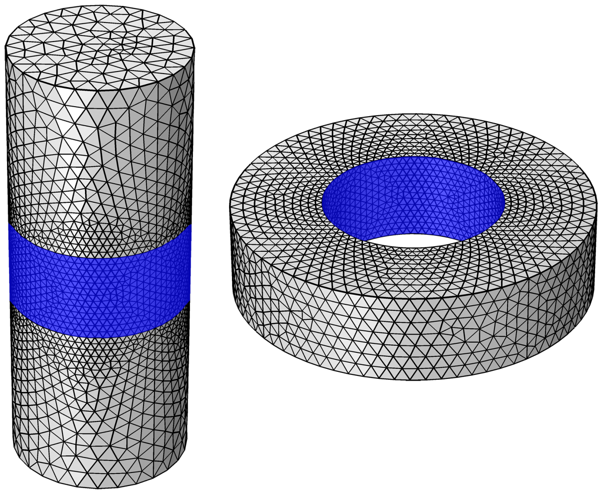

Figure 4.3: Highlight of the fluid film region.

In Figure 4.3 the highlighted blue region of the journal and bearing indicates the fluid film region, and the rest of the journal and bearing is called the solid region. It is from the figure seen that where the two regions meet, they have the same mesh density. However, when examining the solid region it is notable that the length between nodes is seen to increase as the nodes moves further away from the fluid film region. In the mesh convergence study, the mesh density of the fluid film region is determined first.

With the mesh determined only the relative tolerance used in time dependant solver has to be determined. For the time dependent solver the relative tolerance is used to evaluate the appropriate time steps, the maximum time step however is set $10\,\mu$s. The relative tolerances and maximum node distances are noted in Table 4.6 and a more detailed procedure is found in Appendix D on page 105.

Table 4.6: Relative tolerance and maximum node distance.

Relative tolerance steady state	Relative tolerance time dependent	Maximum node distance fluid film region	Maximum node distance solid region
10^{-3}	0.1	0.9 mm	2.5 mm

4.5 Data logging

As the time step is varying in COMSOL, as stated in Section 4.4 on the preceding page, a constant sampling rate of 80 kHz is chosen, since it is found possible to use ultrasound transducers with this pulse rate [1].

In the virtual experiments the temperature and dynamic viscosity of the oil is spatially dependent. It is for this reason that these are logged as 36 evenly distributed points along the circumference and in the middle of the oil film, as shown in Figure 4.4 on the following page.

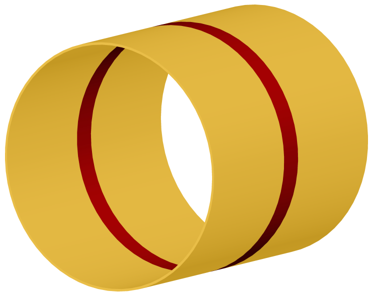

Figure 4.4: Red line indicating the placement of the 36 points of measurements.

4.6 Dynamic validation

Despite the limitations of the virtual experiments, they still exclude some of assumptions used in the derivation of the analytical model and is for this reason believed to represent an actual journal bearing to a greater extend. The main advantages of the virtual experiments are the following:

- The short bearing approximation is not included.
- Convection and conduction in the circumferential and longitudinal direction are included.
- Temperature and pressure are time dependent.
- The boundary temperature, and therefore also boundary viscosity, varies in space.
- The fluid parameter such as density, thermal conductivity, and specific heat capacity varies with temperature.
- The dynamic viscosity is modelled by Barus-Vogel, meaning it is temperature and pressure dependent.
- The viscous dissipation is modelled using shear in both the circumferential and longitudinal direction.

The main disadvantage of the virtual experiments is the use of the thermally thin approximation, which is not used in the analytical thermoviscous model.

With these differences between the analytical models and the virtual experiments some differences are expected, these are seen in Figure 4.5a.

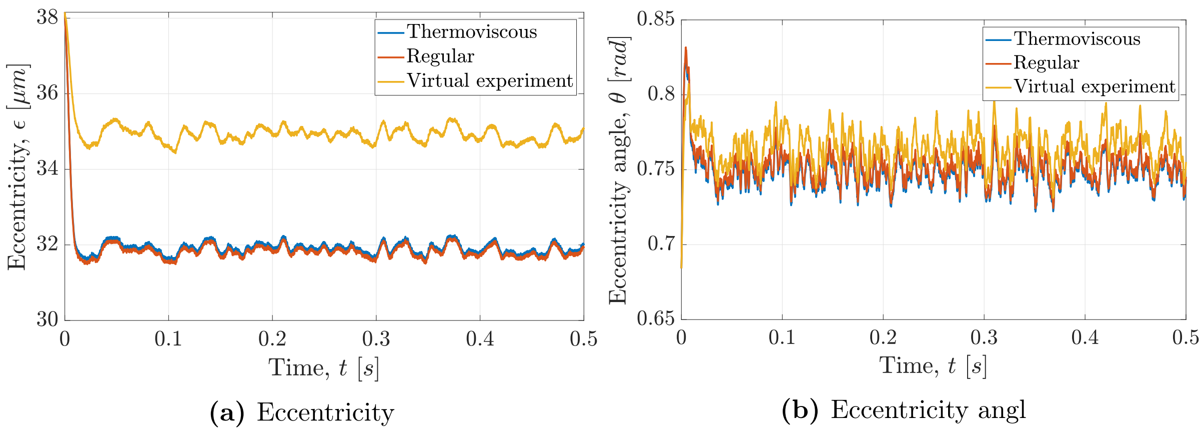

Figure 4.5: Comparison of a virtual experiment and analytical models.

A virtual experiment and the analytical models are modelled with the parameters and dimensions given in Appendix G on page 113.

In the simulation the external force is modelled as a random binary signal. The external force is applied in the α-direction and the magnitude varies between 50 N and 150 N. In the simulation the journal angular velocity is 100π rad/s.

The boundary viscosity used in the thermoviscous model are found using the Vogel model, with the spatially mean at a given time instance. The viscosity of the regular hydrodynamic model is found by using the mean temperature of the fluid film during the entire simulation.

The temperature change during the simulation of 0.5 s is found negligible, furthermore the angular velocity of the journal is significantly small, this results in the two analytical models to be almost identical, as seen in Figure 4.5a on the preceding page. The virtual experiment is seen to estimate the eccentricity slightly larger than the analytical models. This is the same tendency found by G.B. DuBois and F.W. Ocvirk [8] when comparing their analytical S.S, described in section 2.2 on page 4, with experimental data. The differences in eccentricity angles between the analytical models and virtual experiment is from Figure 4.5b on the preceding page seen to be insignificant. It is from 4.5 on the facing page seen that the both the analytical models have very similar mechanical dynamics as the virtual experiment. It is from this deemed that the analytical models represent the system to a satisfying degree, and that the TSO strategies is able to compensate for the constant offset. The analytical models are for the purpose of TSO derivation deemed valid.

5 Acoustics

The TSO strategies proposed in this study are based on ultrasound reflectometry. Ultrasound reflectometry methods are of interest for TSO development due to its non-invasive properties. In order to derive the coupling between the fluid film height and the ultrasound measurements, it is of interest to derive a model describing the acoustic properties of the system.

5.1 Three layered structure model

The acoustic model is derived from a three layered structure representation of the system. As seen in Figure 5.1 the three layers denoted a, b, and c corresponds to the bushing, fluid film, and journal, respectively. An arbitrary pressure wave is send into the structure and the resulting transmission and reflection of the pressure wave is illustrated in the figure. It is notable that for this study only longitudinal waves are considered.

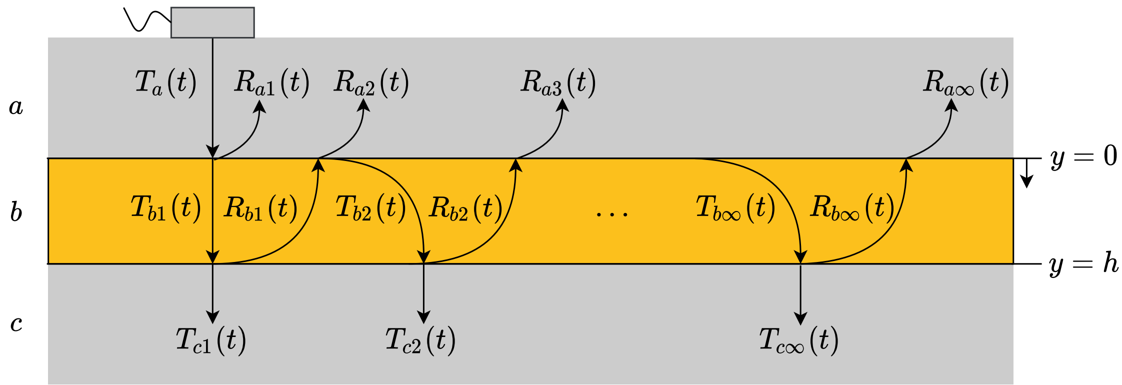

Figure 5.1: The three layered structure with pressure wave propagation. [12]

The incident wave emitted from the ultrasound transducer is denoted as T_a. When the incident wave reaches the boundary between material a and b it scatters into a reflection wave, R_a, and a transmission wave, T_b. This scattering of waves occurs each time a pressure wave encounters a boundary between two materials of different specific acoustic impedances, z. The reflections that occur in the materials are described using the reflection coefficient, R, which is given below. [15] [17]

$$R_{gh} = \frac{z_h - z_g}{z_h + z_g} = -R_{hg} \qquad (5.1) \qquad\qquad z = \rho\, c \qquad (5.2)$$

Where the index gh indicates a reflection coefficient for a wave travelling through material g into the boundary between g and h. c is the speed of sound. Using the reflection coefficient the initial reflection wave, R_{a1}, induced by the incident wave is calculated by the following equation.

$$R_{a1}(t)|_{y=0} = R_{ab} T_a(t)|_{y=0} \qquad (5.3)$$

The transmission wave induced by the incident wave, T_{a1}, is found on the basis that the pressure has to be equal on both sides of the boundary.

$$T_{b1}(t) = T_a(t) + R_{a1}(t) = (1 + R_{ab})T_a(t) \tag{5.4}$$

It should be noted that the above and future equations are derived at the ab-boundary at $y = 0$ but the mathematical notation is precluded in the equations due to simplicity.

Using the pressure constraint from eq. 5.4 for the entire series of transmission waves, T_{bx}, the following infinite sum is derived.

$$\begin{aligned} T_b(t) &= \underbrace{(1 + R_{ab})T_a(t)}_{T_{b1}} + \underbrace{R_{bc}\,(-R_{ab})(1 + R_{ab})T_a(t-\tau)}_{T_{b2}} \\ &\quad + \ldots + \underbrace{R_{bc}^n(-R_{ab})^n(1 + R_ab)T_a(t-n\tau)}_{T_{bn}} \\ &= (1 + R_{ab})T_a(t) + (1 + R_{ab})\sum_{n=1}^{\infty}(-R_{ab})^n R_{bc}^n T_a(t-n\tau) \end{aligned} \tag{5.5}$$

Here τ denotes the time delay caused by the travel time of a pressure wave through the fluid film and back again and is given by the following equation.

$$\tau = \frac{2h}{c_b} \tag{5.6}$$

Where h is the height of the fluid film layer. The infinite series representing the reflection wave, $R_b(t)$, is found in a similar manner as $T_b(t)$ and is given below.

$$\begin{aligned} R_b(t) &= \underbrace{(1 + R_{ab})R_{bc}T_a(t-\tau)}_{R_{b1}} + \underbrace{(-R_{ab})R_{bc}^2(1 + R_{ab})T_a(t-2\tau)}_{R_{b2}} \\ &\quad + \ldots + \underbrace{(-R_{ab}^{n-1}R_{bc}^n(1 + R_{ab})T_a(t-n\tau)}_{R_{bn}} \\ &= -\frac{1 + R_{ab}}{R_{ab}}\sum_{n=1}^{\infty}(-R_{ab})^n R_{bc}^n T_a(t-n\tau) \end{aligned} \tag{5.7}$$

At a boundary the pressure must equal on both sides resulting in the following equation for boundary ab.

$$T_a(t) + R_a(t) = T_b(t) + R_b(t) \tag{5.8}$$

Inserting equation eq. (5.5) and eq. (5.7) into eq. (5.8) the following equation is derived.

$$\begin{aligned} R_a(t) &= T_b(t) + R_b(t) - T_a(t) \\ &= \underbrace{\left((1 + R_{ab})T_a(t) + (1 + R_{ab})\sum_{n=1}^{\infty}(-R_{ab})^n R_{bc}^n T_a(t-n\tau)\right)}_{T_b(t)} \\ &\quad + \underbrace{\left(-\frac{1 + R_{ab}}{R_{ab}}\sum_{n=1}^{\infty}(-R_{ab})^n R_{bc}^n T_a(t-n\tau)\right)}_{R_b(t)} - T_a(t) \\ &= R_{ab}T_a(t) + \frac{R_{ab}^2 - 1}{R_{ab}}\sum_{n=1}^{\infty}(-R_{ab}R_{bc})^n T_a(t-n\tau) \end{aligned} \tag{5.9}$$

Due to the short time of flight in the fluid film layer it is often of interest to represent the acoustic model in the frequency domain. This representation is realised by representing the time of flight in the frequency domain as given in the equation below. This is also known as the layer spectrum, $J(\omega)$.

$$J(\omega) = e^{-i\omega\tau} \tag{5.10}$$

The reflection coefficient spectrum, $R(\omega)$, is the frequency representation of the acoustic system process. The reflection coefficient spectrum is defined as in eq. (5.11), and is found from eq. (5.9).

$$R(\omega) = \frac{\mathcal{F}[R_a(t)]}{\mathcal{F}[T_a(t)]} = R_{ab} + \frac{R_{ab}^2 - 1}{R_{ab}} \sum_{n=1}^{\infty} (-R_{ab}R_{bc}J(\omega))^n \tag{5.11}$$

The infinite sum in eq. (5.11) is seen to be a geometric series and it is for this reason possible to simplify this equation using the following relation, since the magnitude of the layer spectrum is equal to one and the magnitude of the reflection coefficients practically always are less than one. [18, p. 134]

$$\sum_{k=1}^{\infty} f^k = \frac{f}{1-f} \quad \textbf{if} \quad |f| < 1 \tag{5.12}$$

$$|R_{ab}R_{bc}J(\omega)| < 1 \tag{5.13}$$

The reflection coefficient spectrum then becomes.

$$R(\omega) = \frac{R_{ab} + R_{bc}J(\omega)}{1 + R_{ab}R_{bc}J(\omega)} \tag{5.14}$$

This equation is the acoustic model for the journal bearing in the frequency domain and forms the theoretical basis for both derivation of the TSO strategies and also the acoustic simulations.

5.2 Acoustic simulations

The parameters needed for the acoustic model are the density and speed of sound for the journal, bushing and fluid film. It is assumed that both the bushing and journal are made from AISI 4030 steel. The density is found to be 7850 $\frac{\text{kg}}{\text{m}^3}$ as described in Chapter 4 on page 21. The speed of sound is found to be 5850 $\frac{\text{m}}{\text{s}}$ [14]. The density of the oil used for the fluid film layer is found to be given as eq. (4.2) on page 22. The speed of sound of the oil is found to be given as in eq. (5.15) [10].

$$c_b = q_3 - q_2\ (T - q_4) + q_1\ (T - q_4)^2 \tag{5.15}$$

Table 5.1: Speed of sound oil parameters. [10]

q_1	q_2	q_3	q_4
3.9 $\left[\frac{mm}{s\,K^2}\right]$	3.39 $\left[\frac{m}{s\,K}\right]$	1555 $\left[\frac{m}{s}\right]$	273.2 $[K]$

With these parameters it is possible to calculate the reflection coefficients for the two boundaries used in the acoustic model, given by eq. (5.1).

5.2.1 Incident wave

The incident wave, used for the acoustic model, is modelled as a Gaussian pulse. A Gaussian pulse is chosen since it has a similar frequency response as an incident wave experimentally found in the previous study [12]. Both time an frequency response of the designed Gaussian pulse and experimentally found incident wave is seen in Figure 5.2.

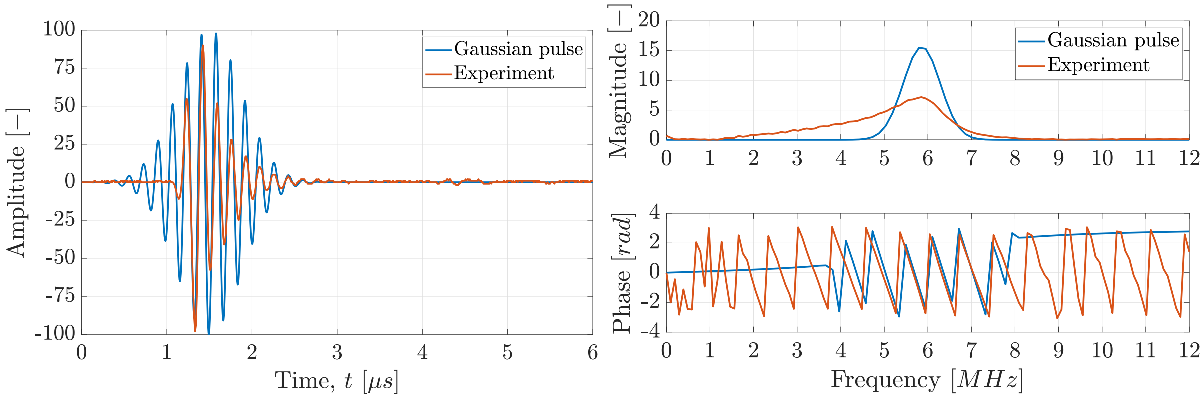

(a) Incident wave in time domain **(b)** Frequency response of incident wave

Figure 5.2: Comparison of incident waves.

It is from Figure 5.2b seen that the frequency band of the Gaussian pulse is more narrow compared to the experimentally found incident wave. It is also seen in the figure that the resonance frequency of the incident wave is at approximately 5.86 MHz. Furthermore, it is seen that both Gaussian pulse and experimentally found incident wave has similar phase properties within the exited frequencies of the signal. It is found from 3.5 µs to 6 µs in Figure 5.2a that the noise on the ultrasound transducer measurements approximately has a standard deviation of 0 75.

5.2.2 Reflection wave

In the acoustic simulation the reflection wave is is modelled in the discrete time domain using eq. (5.16).

$$R_a(t) = R_{ab}T_a(t) + \frac{R_{ab}^2 - 1}{R_{ab}} \sum_{n=1}^{\left\lceil \frac{T_{pr}}{T_s} \right\rceil} (-R_{ab}R_{bc})^n T_a(t - n\tau) \tag{5.16}$$

Where T_{pr} is the time between the pulses from the ultrasound transducer. T_s is the time step of the simulation, modelled to be 0.1 ns. The acoustic measurements used for the data processing are down sampled to a frequency of 100 MHz. A flow diagram of the model is seen in 5.3 on the next page.

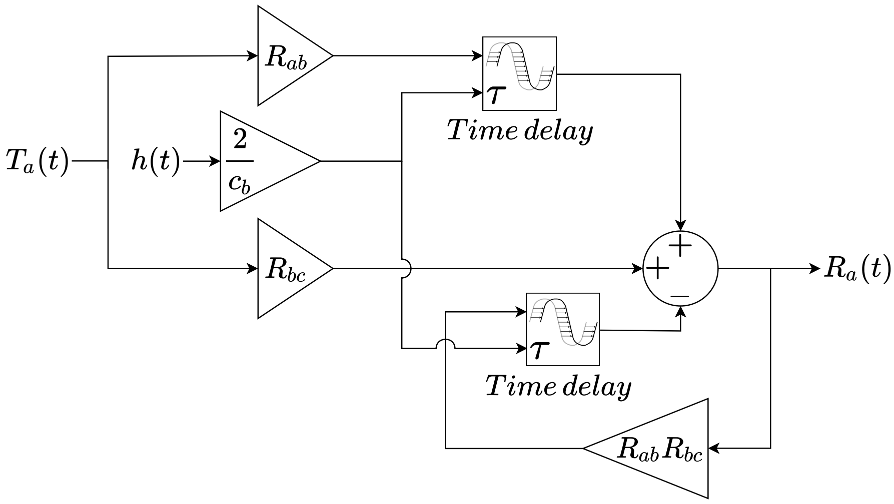

Figure 5.3: The simulation of the reflection wave from a predetermined incident wave.

The reflection coefficient are modelled as temperature dependent since the density and speed of sound in the oil is temperature dependent. The reason for not modelling temperature dependency of the steel is that this is found to be negligible compared to that of the oil. [10]

The measurement noise on the reflection wave is modelled as Gaussian white noise with a standard deviation of 1. The reason for choosing this value, is that the standard deviation from the laboratory sample was found to be approximately 0.75, and the modelled standard deviation is larger than this to account for uncertainties.

6 Tribological state observer

This study aims to investigate the performance of different TSO strategies. All the TSO strategies investigated are based on Extended Kalman Filters (EKF). The EKF algorithm is shown in full in Appendix B on page 101. The EKF algorithm is based on a discrete state space system representation.

$$\vec{x}_{k+1} = \vec{\mathcal{H}}(\vec{x}_k, \vec{u}_k) + \vec{d}_k \tag{6.1}$$

$$\vec{y}_k = \vec{\mathcal{G}}(\vec{x}_k) + \vec{n}_k \tag{6.2}$$

Where $\vec{x}$ is the state vector. $\vec{u}$ is the system input vector. $\vec{y}$ is the system output vector. $\vec{\mathcal{H}}$ is a nonlinear system process vector. $\vec{\mathcal{G}}$ is a nonlinear system output vector. $\vec{d}$ and $\vec{n}$ are the system disturbance and noise vectors, respectively. Both $\vec{d}$ and $\vec{n}$ are assumed to be Gaussian white noise with covariance matrices $\underline{C_d}$ and $\underline{C_n}$, respectively.

Since the derived journal bearing models are differential equations they are discretized using the Forward Euler method to comply with the EKF algorithm. The forward Euler method is shown below.

$$\dot{\vec{x}} \approx \frac{(\vec{x}_{k+1} - \vec{x}_k)}{T_{pr}} = \vec{\mathcal{H}}\left(\vec{x}_k, \vec{u}_k\right) \tag{6.3}$$

Where the time step is the corresponding sampling rate of the height measurements which is the pulse rate of the ultrasound transducer, T_{pr}. It is notable that for the EKF algorithm the tuning parameters are the covariance matrices of the disturbance and noise, $\underline{C_d}$ and $\underline{C_n}$. However, $\underline{C_n}$ is often quantifiable from measurement data. Another tuning parameter is the covariance matrix of the initial guess of the states denoted as $\underline{Pc}_0$.

The state space representation of both analytical journal bearing models uses the same input vector defined as the following equation.

$$\vec{u}_k = \begin{bmatrix} F_{\alpha,ext} & F_{\beta,ext} & \omega \end{bmatrix}^T \tag{6.4}$$

Furthermore, both the journal bearing models have the following four mechanical states.

$$\vec{x}_{mech} = \begin{bmatrix} \epsilon_k & \dot{\epsilon}_k & \theta_k & \dot{\theta}_k \end{bmatrix}^T \tag{6.5}$$

The journal bearing model that uses the thermoviscous pressure equation have the extra state of boundary fluidity.

$$x_{therm} = \delta_{b,k} \tag{6.6}$$

This state is assumed to be slow varying compared to the mechanical states of the system, and the model for this state is for this reason given as the following equation.

$$\delta_{b,k+1} = \delta_{b,k} \tag{6.7}$$

In the derivation of the thermoviscous pressure equation it is assumed that this boundary fluidity is related to an equivalent journal bearing temperature. It is therefore possible to calculate the equivalent temperature from the estimated boundary fluidity, and compare this to a sensor measurement. In a real life system, it is expected that the best results is achieved by using Vogel's viscosity model, eq. (2.1), for this calculation. However, since this is the model used in the virtual experiment to describe the temperature dependency of the viscosity, the Reynold's viscosity model, eq. (3.56), is used for this calculation in the test of the TSOs, in order to introduce model uncertainty. This equation is given below.

$$T_{eq} = -\frac{ln\left(\frac{1}{\delta_b\, a_r}\right)}{b_r} \tag{6.8}$$

6.1 Discrete system analysis

In order for the discrete system representation to represent the continuous system to an acceptable degree, the update frequency of the discrete system has to be significantly larger than the largest system frequency. A linear analysis of the system poles is for this reason derived. The linear analysis takes basis in distance to the pole furthest from the origin of the complex plane, since this distance is the break-off frequency of a standard first and second order system.

It is believed that ideally the system is fully represented if half the update frequency, the Nyquist frequency, is larger than the largest system frequency. However due to uncertainty of a linear analysis on the nonlinear system it is believed that the update frequency should be at least three times larger.

6.1.1 Linearisation points

The linear analysis is derived by choosing linearisation points around the S.S. solutions presented by F.W. Ocvirk and G.B. DuBois, this is such that the system inputs matches the eccentricity and eccentricity angle for the given linearisation point. The linear analysis contains ten linearisation points found by varying the eccentricity ratio from 5 % to 95 %. With the eccentricity ratio it is possible to calculate the load number and eccentricity angle from eq. (2.2) and eq. (2.3) from Chapter 2.2 on page 4, respectively. With the load number it is then possible to calculate the external force, required to reach the S.S. point for a given journal angular velocity. The linear analysis is performed for journal angular velocities of 100 rad/s and 500 rad/s. The linear analysis is performed on the regular hydrodynamic journal bearing model. This is such that it is possible to determine the S.S. point from the load number and because it is found in Chapter 3.7 on page 19 that the primary difference between the two analytical models simply corresponds to a change in the viscosity term of the regular hydrodynamic model.

In order to analyse the system in and around S.S., a sweep of the state velocities is performed. The results from this analysis is shown in Figure 6.1 on the next page.

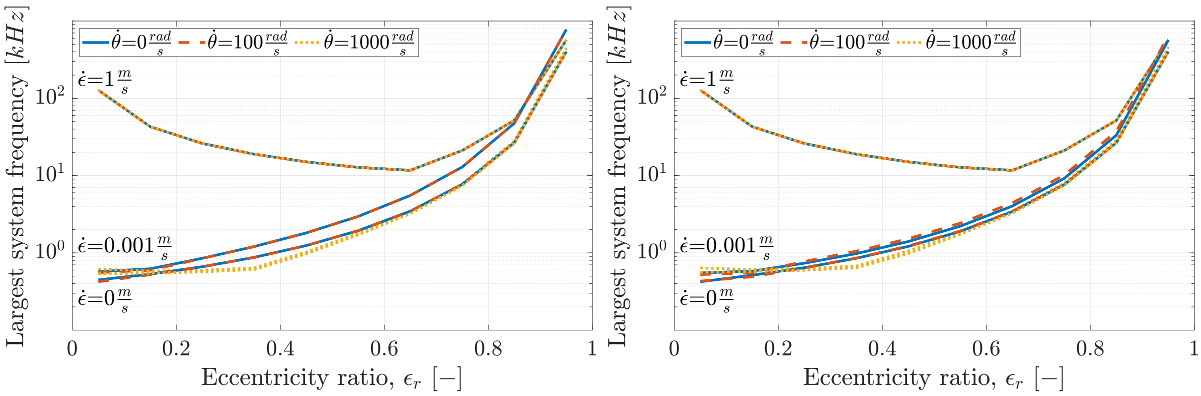

(a) $\omega = 100\,\frac{\text{rad}}{\text{s}}$ **(b)** $\omega = 500\,\frac{\text{rad}}{\text{s}}$

Figure 6.1: Largest system frequency as a function of eccentricity ratio at different eccentricity and eccentricity angle velocities.

It is from Figure 6.1 seen that in general the largest system frequency increases as the eccentricity ratio increases. It is from the figure also seen that journal angular velocity does not have a significant effect on the system dynamics. It is further seen that the state velocities do not have a significant effect on the system dynamics, unless they are unrealistically large. The above velocities are assumed unrealistic since the eccentricity is in order of $\mathcal{O}(10^{-6})$ and the eccentricity angle is in the order of $\mathcal{O}(1)$. It is for this reason the system is linearised at steady state, where the state velocities are zero.

6.1.2 Analysis of system dynamics

Figure 6.2 shows the largest system frequency as a function of the eccentricity ratio, for the baseline system with a journal angular velocity of 100 rad/s and 500 rad/s, and the recommended cut-off line of one third the update frequency.

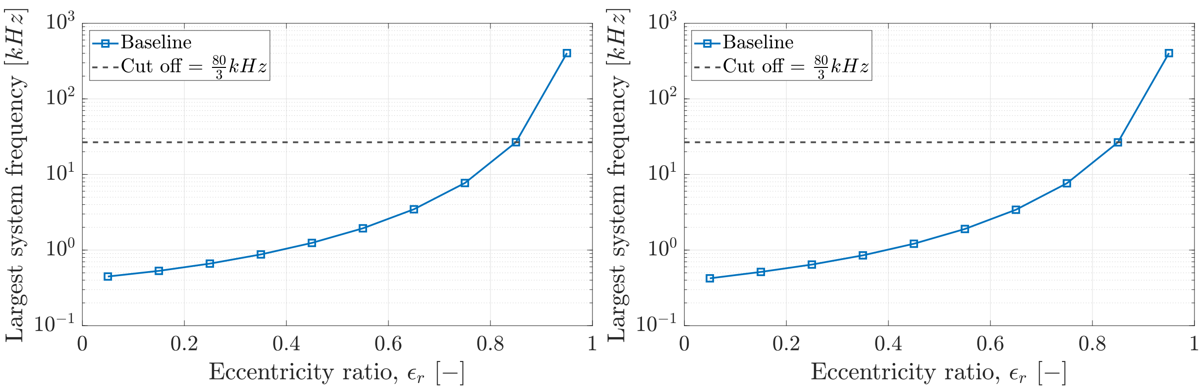

(a) $\omega = 100\,\text{rad/s}$ **(b)** $\omega = 500\,\text{rad/s}$

Figure 6.2: Largest system frequency as a function of eccentricity ratio for baseline model.

From the figure it is seen that when the eccentricity ratio is larger than 85 %, the largest system frequency is larger than the recommended frequency. It is from this believed, that if it is desired to apply the TSO to systems where the working point is outside this range, higher update rates is required or a redesign of the journal bearing is needed. In order to investigate how a redesign of the journal bearing affect the system dynamics, an analysis of the largest system frequency is seen in Figure 6.3 on the facing page, when the system parameters are double and half the baseline values. The figure also include the difference in largest system frequency for a change in viscosity, this is to determine how a change in temperature affect the system, but also shows how the analysis relates to the thermoviscous journal bearing model.

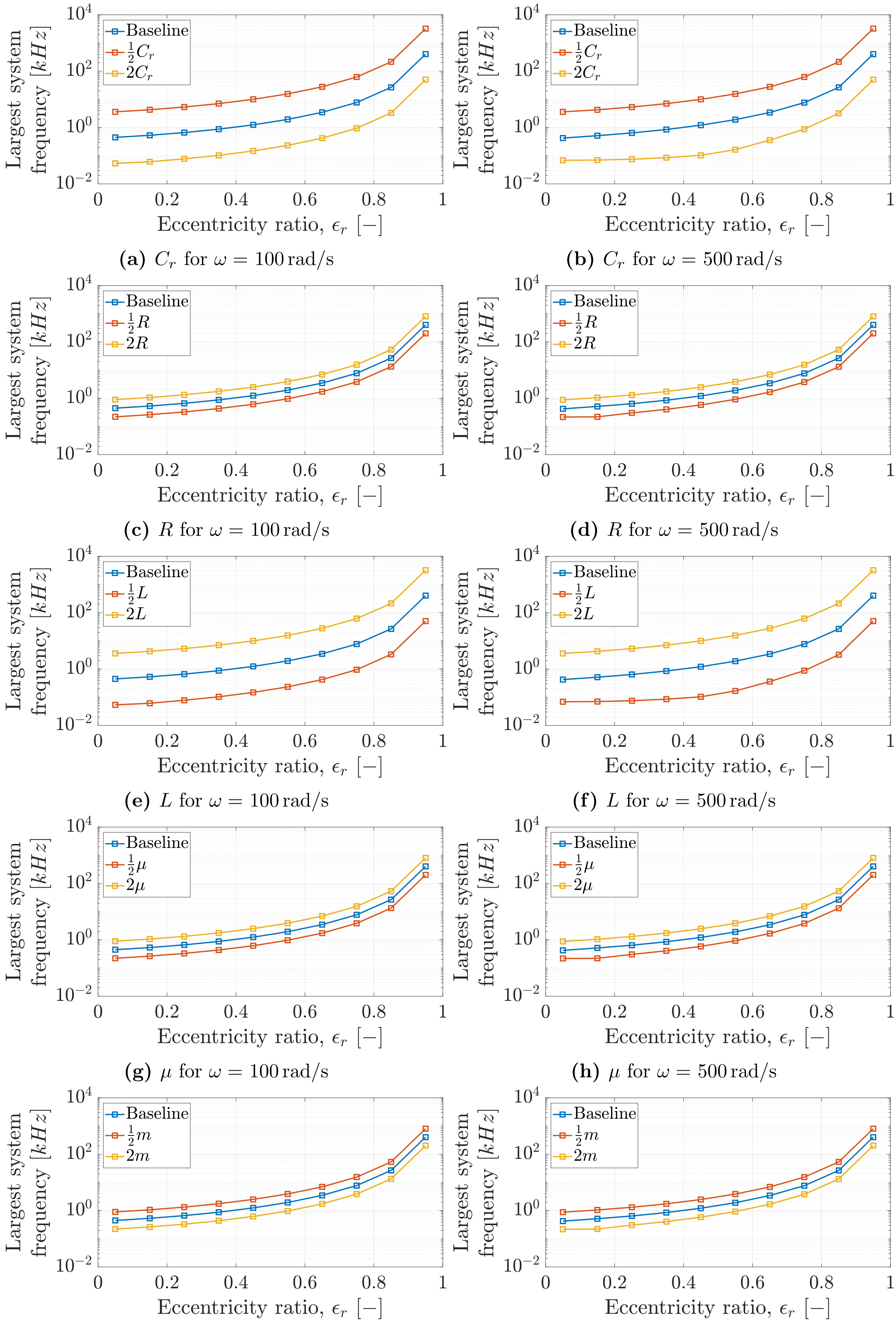

(a) C_r for $\omega = 100\,\mathrm{rad/s}$
(b) C_r for $\omega = 500\,\mathrm{rad/s}$
(c) R for $\omega = 100\,\mathrm{rad/s}$
(d) R for $\omega = 500\,\mathrm{rad/s}$
(e) L for $\omega = 100\,\mathrm{rad/s}$
(f) L for $\omega = 500\,\mathrm{rad/s}$
(g) μ for $\omega = 100\,\mathrm{rad/s}$
(h) μ for $\omega = 500\,\mathrm{rad/s}$
(i) m for $\omega = 100\,\mathrm{rad/s}$
(j) m for $\omega = 500\,\mathrm{rad/s}$

Figure 6.3: Largest system frequency as a function of epsilon ratio for a change in system parameters.

From Figure 6.3 on the previous page it is seen that a increase in bushing inner radius, fluid film length and viscosity, increases the largest system frequency and vice versa. It is also seen in the figure that a increase in radial clearance and mass reduces the largest system frequency and vice versa.

It is from this seen that it is possible to obtain a balance between the input and parameter fraction in the load number, eq. (6.9), such that the system can be operated at the same eccentricity ratio but with a lower largest system frequency.

$$L_N = 4\,\pi \underbrace{\frac{C_r^2}{\mu\,L^3\,R}}_{Parameters} \underbrace{\frac{|F_{ext}|}{\omega}}_{Inputs} \tag{6.9}$$

It is from the above equation and figure seen that if it is desired to change the largest system frequency but keep the same eccentricity ratio, it is most efficient to change the fluid film length, hereafter the radial clearance, with regards to the largest system frequency change per change in the variable.

6.2 Auto-calibration

The previous study from the same authors proposed using an auto-calibration algorithm in order to estimate the fluid film height, and then using this estimate of the fluid film height as the input to a TSO algorithm. [12] A flow diagram of this strategy is shown in Figure 6.4.

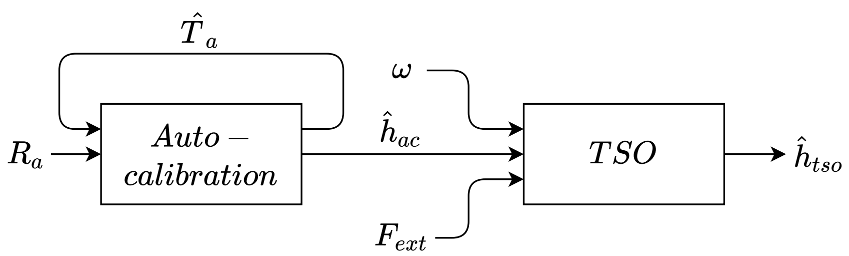

Figure 6.4: TSO strategy from the previous project.

In this strategy the proposed auto-calibration algorithm is an EKF algorithm, that uses a regression model based on the magnitude of the layer spectrum, in this report referred to as Layer spectrum magnitude evaluation (LSME). It is found in Chapter 5 on page 31 that the reflection coefficient spectrum is given as eq. (5.14), solving this equation for the layer spectrum the following equation is derived.

$$J(\omega) = e^{-i\omega\tau} = \frac{1}{R_{bc}} \frac{R_{ab} - R(\omega)}{R_{ab}\,R(\omega) - 1} \tag{6.10}$$

It is seen from eq. (6.10) that the magnitude of the layer spectrum is equal to one for all frequencies. It is from this property of the layer spectrum that the following equation is derived.

$$R_{bc}^2 |R_{ab}\,R(\omega) - 1|^2 = |R_{ab} - R(\omega)|^2 \tag{6.11}$$

In this equation the reflection coefficient spectrum is rewritten to take the following form.

$$R(\omega) = A(\omega)\ \left(cos(\gamma(\omega)) + i\,sin(\gamma(\omega))\right) \tag{6.12}$$

Where $A(\omega)$ is the magnitude and $\gamma(\omega)$ is the phase of the reflection coefficient spectrum. Inserting this relation into eq. (6.11), the following equation is found.

$$A(\omega)^2 \underbrace{\left(1 - R_{ab}^2 R_{bc}^2\right)}_{K_A} + \underbrace{\left(R_{ab}^2 - R_{bc}^2\right)}_{K_B} = 2\, A(\omega)\, cos(\gamma(\omega))\, \underbrace{\left(R_{ab}\left(1 - R_{bc}^2\right)\right)}_{K_c} \tag{6.13}$$

In this equation the magnitude and phase term are rewritten using the following two relations.

$$A|_{\omega=\omega_i} = \frac{|\vec{R}_a|}{|\vec{T}_a|} \tag{6.14}$$

$$cos(\gamma)|_{\omega=\omega_i} = \frac{\vec{R}_a^T \vec{T}_a}{|\vec{R}_a|\,|\vec{T}_a|} \tag{6.15}$$

Where $\vec{R}_a$ and $\vec{T}_a$ are the real and imaginary component of the frequency spectrum of the reflection and incident wave evaluated at a single frequency, ω_i, respectively.

$$\vec{R}_a = \begin{bmatrix} Re(\mathcal{F}[R_a(t)]) \\ Im(\mathcal{F}[R_a(t)]) \end{bmatrix} \Bigg|_{\omega=\omega_i} \tag{6.16}$$

$$\vec{T}_a = \begin{bmatrix} Re(\mathcal{F}[T_a(t)]) \\ Im(\mathcal{F}[T_a(t)]) \end{bmatrix} \Bigg|_{\omega=\omega_i} \tag{6.17}$$

Inserting eq. (6.14) and eq. (6.15) into eq. (6.13) the following equation is derived.

$$|\vec{R}_a|^2 = \left(2\frac{K_C}{K_A}\vec{R}_a^T - \frac{K_B}{K_A}\vec{T}_a^T\right)\vec{T}_a \tag{6.18}$$

This equation is the regression model based on the magnitude constraint of the layer spectrum. Assuming that the incident wave is slow varying compared to the fluid film height, as for the boundary fluidity term in eq. (6.7). This equation is implemented into a EKF algorithm, where the states are given as the following.

$$\vec{x}_{k,AC} = \vec{T}_a \tag{6.19}$$

The system output is given by the following equation.

$$\vec{y}_{k,AC} = |\vec{R}_a|^2 \tag{6.20}$$

This Auto-calibration algorithm estimates the frequency response of the incident wave, and this estimate is then reformulated to an estimate of the fluid film height using the layer phase lag (LPL) method.

The LPL method takes offset in eq. (6.10) and with the estimate of the frequency response of the incident wave together with the measurement of the reflection wave, it is possible to estimate the layer spectrum. This estimate is used to determine the phase lag of the layer spectrum, given as the following equation.

$$\angle J(\omega) = -\omega\tau \tag{6.21}$$

It is from this equation possible to compute τ and from this an estimate of the fluid film height, from the equation below.

$$h = \frac{\tau\, c_b}{2} \tag{6.22}$$

In the previous study this fluid film height estimate is used as an input for a TSO strategy using an analytical journal bearing model. This method of implementing a TSO is however assumed to be inferior compared to methods where the ultrasound measurements is directly linked to the mechanical states of the TSO. A flow diagram of this strategy is shown in Figure 6.5.

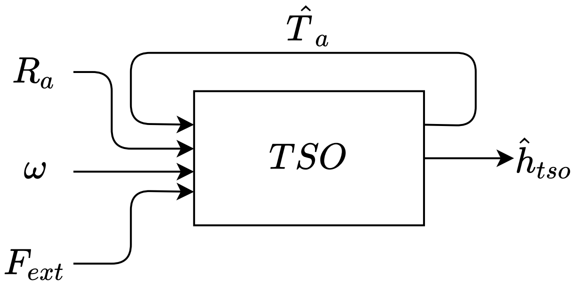

Figure 6.5: Combined TSO and auto-calibration strategy.

These types of TSO strategies have the advantage of linking the estimate of the incident wave to the estimate of mechanical states and therefore the theoretical benefit of increased robustness, since more information of the system is present in the algorithm. The LSME auto-calibration algorithm is in this study therefore compared to these types of TSO algorithms.

6.3 TSO based Auto-calibration

The concept of TSO based auto-calibration is based on linking a dynamic system model, describing the mechanical states, with known system inputs to the ultrasound measurements. In this study two different methods for linking the mechanical states to the ultrasound measurements are proposed.

6.3.1 Analysis of the complex components of the reflection coefficient spectrum

The first method is based on estimating the complex components of the incident wave, similarly to the LSME algorithm. This method is referred to as Complex component evaluation (CCE). The method is based on the reflection coefficient spectrum, where the layer spectrum is rewritten to the following form.

$$J(\omega) = e^{-i\omega\tau} = cos(\omega\tau) - i\, sin(\omega\tau) \tag{6.23}$$

Inserting this into the reflection coefficient spectrum, eq. (5.14), and isolating for the real and imaginary components, the following equation is derived.

$$R(\omega) = \underbrace{\frac{R_{bc}\,\left(R_{ab}^2+1\right)\cos\left(\omega\tau\right) + R_{ab}\,\left(R_{bc}^2+1\right)}{R_{ab}^2 R_{bc}^2 + 2\,\cos\left(\omega\tau\right) R_{ab}\, R_{bc} + 1}}_{X} + i\,\underbrace{\frac{R_{bc}\,\sin\left(\omega\tau\right)\left(R_{ab}^2-1\right)}{R_{ab}^2 R_{bc}^2 + 2\,\cos\left(\omega\tau\right) R_{ab}\, R_{bc} + 1}}_{Y} \tag{6.24}$$

The frequency response of the reflection wave is found from the following equation.

$$R_a(\omega) = R(\omega)\, T_a(\omega) \tag{6.25}$$

It is from an analysis of the real and imaginary components of this equation seen that the real component of the measured reflection wave is given as the following equation.

$$Re(R_a(\omega)) = X\, Re(T_a(\omega)) - Y\, Im(T_a(\omega)) \tag{6.26}$$

It is also seen that the imaginary component is given as the following equation.

$$Im(R_a(\omega)) = X\,Im(T_a(\omega)) + Y\,Re(T_a(\omega)) \tag{6.27}$$

It is from these equations seen that evaluating them at a fixed frequency and introducing the real and imaginary components of the incident wave as states to the TSO, it is possible to relate the mechanical states from the journal bearing model, to the ultrasound measurements. This is seen since τ from eq. (6.24), is a function of fluid film height, and this relates to the mechanical states using the fluid film height equation.

$$\tau = \frac{2h}{c_b} = \frac{2}{c_b}\left(C_r - \epsilon\, cos(\Omega - \theta)\right) \tag{6.28}$$

Where Ω is the measurement angle from the α-axis in the global coordinate frame, defined in Figure 3.1 on page 7, and describes the placement of the ultrasound transducer on the journal bearing. With the introduction of these output equations, it is possible to derive a TSO that estimates both the mechanical states and the incident wave.

6.3.2 Analysis of the phase of the reflection wave

The second method takes offset in the phase of the reflection wave frequency spectrum. The previously described methods for processing the ultrasound measurements is limited to the evaluation of the frequency spectrum at a single frequency. It is believed that methods that allow for the evaluation of the frequency spectrum at multiple frequencies allow for more consistent estimates. It is for this reason that this study proposes such a method. Figure 6.6 shows an illustration of the frequency response of a reflection wave.

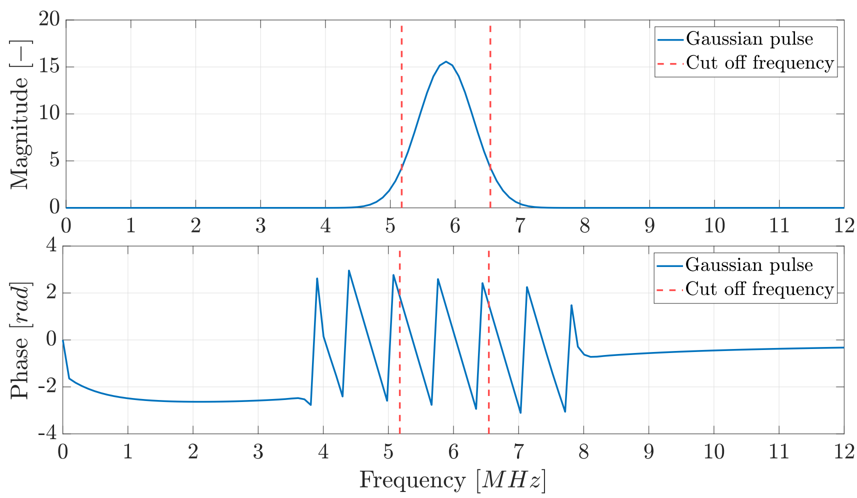

Figure 6.6: Frequency response of the reflection wave.

In Figure 6.6 it is seen that within the excited frequencies the slope of the reflection wave phase is constant. It is for this reason believed that it is possible to numerically derive the slope of the phase using the central difference approximation, eq. (6.29), on the points with a power level above 20 % of the maximum power.

$$\frac{d}{d\omega}\angle R_a(\omega_k) = \frac{\angle R_a(\omega_{k+1}) - \angle R_a(\omega_{k-1})}{\omega_{k+1} - \omega_{k-1}} \tag{6.29}$$

In Figure 6.7 the phase derivative of the reflection wave, found from the central difference approximation, is seen.

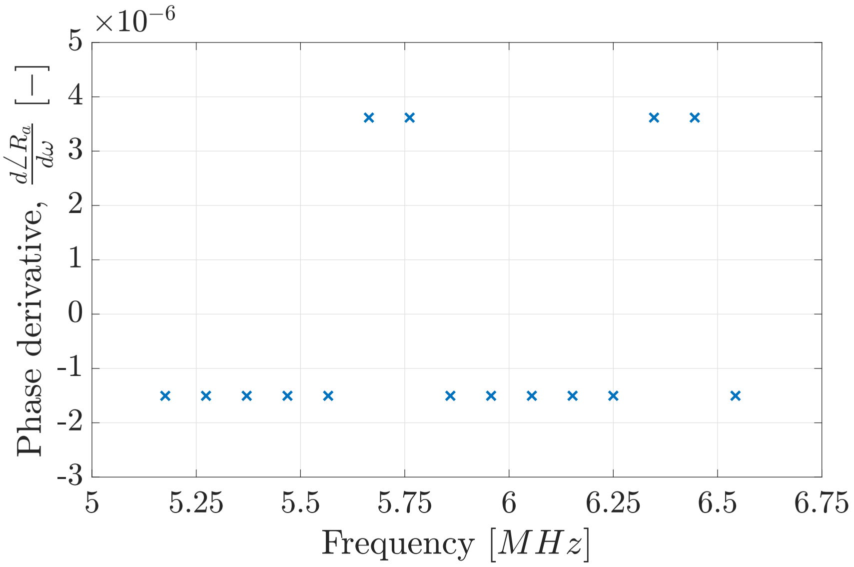

Figure 6.7: Central difference approximation

It is from the figure seen that due to wrapping of the phase, outliers with a positive slope occur. However, the remaining points show a constant negative slope of the phase. It is from this assumed that by excluding the outliers and taking the mean of the remaining points, an estimate of the slope of the phase derivative is found. This estimate might be less sensitive to noise on the measurements.

It is seen that the phase of the reflection and incident wave correlates through the phase lag of the reflection coefficient spectrum as seen in the following equation.

$$\angle R_a(\omega) = \angle R(\omega) + \angle T_a(\omega) \tag{6.30}$$

This relation results in the following equation for the slope of the phase lag.

$$\frac{d}{d\omega}\angle R_a = \frac{d}{d\omega}\angle R(\omega) + \frac{d}{d\omega}\angle T_a(\omega) \tag{6.31}$$

The slope of the phase lag of the reflection coefficient spectrum is found from eq. (5.14) on page 33 where the layer spectrum is rewritten as in eq. (6.23). This gives the following equation.

$$\frac{d}{d\omega}\angle R(\omega) = \frac{\left(R_{ab}^2 R_{bc} + \cos(\omega\tau)\, R_{ab}\, R_{bc}^2 + R_{bc} + \cos(\omega\tau)\, R_{ab}\right) R_{bc}\, \tau \left(R_{ab}^2 - 1\right)}{\left(R_{ab}^2 R_{bc}^2 + 2\, \cos(\omega\tau)\, R_{ab}\, R_{bc} + 1\right)\left(2\, \cos(\omega\tau)\, R_{ab}\, R_{bc} + R_{ab}^2 + R_{bc}^2\right)} \tag{6.32}$$

As for the other TSO algorithm proposed, the fluid film height is found from the mechanical states of the system. It is seen that this equation has to be evaluated at a single frequency, however, the point of measurements contain information from multiple frequencies. It is from this believed that assuming the slope of the phase of the incident wave is slow varying compared with the fluid film height, it is possible to implement this as a state in a TSO, and use eq. (6.31) as an output equation. This method is referred to Phase derivative evaluation (PDE).

6.4 Proposed TSO strategies for comparison

This study is concerned with the performance comparison of the LSME auto-calibration algorithm with the following TSO strategies.

Regular CCE

The Regular CCE method uses the regular analytical Reynolds pressure equation and the complex component evaluation method for ultrasound measurement processing.

Regular PDE

The Regular PDE method uses the regular analytical Reynolds pressure equation and the phase derivative evaluation method for ultrasound measurement processing.

Thermoviscous CCE

The Thermoviscous CCE method uses the thermoviscous analytical Reynolds pressure equation and the complex component evaluation method for ultrasound measurement processing, without temperature measurements.

Thermoviscous CCTE

The Thermoviscous complex component and temperature evaluation (CCTE) method uses the thermoviscous analytical Reynolds pressure equation and the complex component evaluation method for ultrasound measurement processing, with temperature measurements.

7 | Test of TSO strategies

The comparison of the proposed TSO strategies is based on data from the virtual experiments.

7.1 System inputs to the virtual experiments

The design of the system inputs to the virtual experiments is based on the assumption that an encoder is placed on the journal bearing such that the journal angle and angular velocity are recorded, and in many application this might be controlled to an acceptable accuracy. It is however assumed that the radial load on the journal bearing is inherently more random. A major assumption from the derivation of the TSO is that the states such as those describing the incident wave, is slow varying. This entails that a certain excitement of the fluid film height is required. It is from this believed that a fully random signal is not ideal for the test of the TSO, since this might cause an unprecedented level of excitement in the fluid film height, that does not occur in real-world applications. It is for these reasons believed that a better input signal, for the test of the TSOs, is made with a white noise driven band-pass filter.

7.1.1 System excitement

It is believed that in order for the TSO to properly estimate the system states enough excitement has to occur in the fluid film height measurements. It is for this reason of interest to investigate at which force inputs the most excitement in the fluid film height occur. An analysis of the system dynamics in the frequency domain is for this reason proposed. This analysis is based on the linearisation of the regular hydrodynamic system model at the S.S. solutions presented by G.B. DuBois and F.W. Ocvirk. As for the linear analysis in Chapter 6 on page 37, the linearisation points is evaluated by varying the force for ten epsilon ratios between 5 % and 95 % and two journal angular velocities of 100 rad/s and 500 rad/s. Furthermore, the viscosity is swept from half to double the baseline value in order to indicate how the system reacts to a temperature change. The system transfer function is then derived as a linear time independent (LTI) single input single output (SISO) system, where the input is assumed to be the external force and the output is the eccentricity. The eccentricity is considered the system output since this is directly linked to the fluid film height. Figure 7.1 on the following page shows the bandwidth, which is defined as the frequency at which the system gain is below 3 dB of the DC-gain, and DC-gain of the system since it is assumed that these are the most describing properties of the system response.

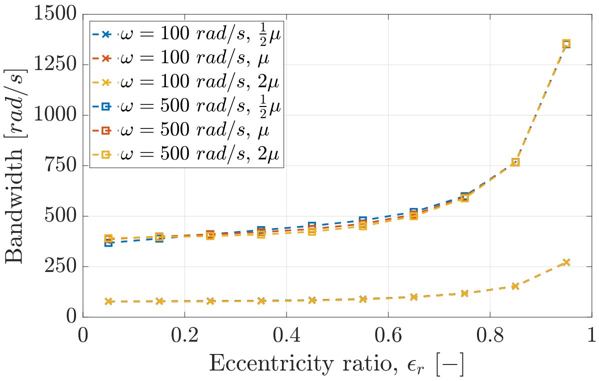

(a) Bandwidth

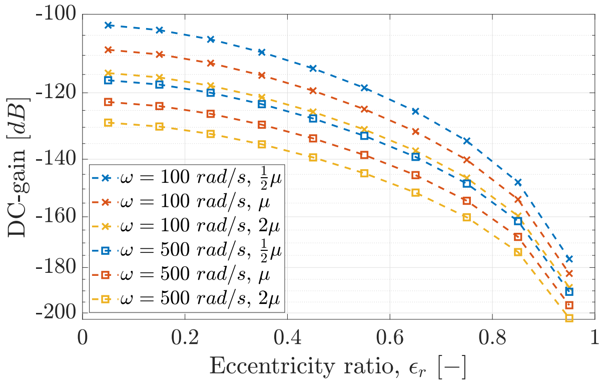

(b) DC-gain

Figure 7.1: System bandwidth and DC-gain as a function of eccentricity ratio.

From Figure 7.1a it is seen that the viscosity has a negligible effect on the system bandwidth. It is however seen that the journal angular velocity has a significant effect on the system bandwidth, where an increase in journal angular velocity increases the system's bandwidth. It is from the figure also seen that the system has larger bandwidth at large eccentricity ratios. It is from Figure 7.1b seen that an increase in both journal angular velocity and viscosity decreases the dc-gain. This is expected from the load number where an increase in journal angular velocity and viscosity results in the need for a larger change in force to get the same absolute change in load number, and heron same absolute change in S.S. eccentricity ratio. It is from the figure also seen that the DC-gain decreases for large eccentricity ratios. It should be noted that this analysis is based on the eccentricity ratio instead of the fluid film height. This means that depending on the ultrasound transducer placement, the DC-gain shown in Figure 7.1 might not depict the DC-gain to a satisfying degree.

It is from Section 6.1.2 on page 39 seen that the discrete system representation is representative up to a eccentricity ratio of 85 %. In this range of eccentricity ratios it is, from Figure 7.1a, seen that the system has a mean bandwidth of 87.9 rad/s and 452 rad/s for a journal angular velocity of 100 rad/s and 500 rad/s, respectively.

7.1.2 Bandpass force input

The tests of the TSOs are based on data where the force input is modelled as a white noise applied to a bandpass filter and the journal angular velocity is 500 rad/s. Section 6.1.2 on page 39 discusses that the discretization of the system is limited to eccentricity ratios up to 85 %. The force input is for this reason modelled such that the mean value is 63 N corresponding to an eccentricity ratio of 50 %. The above bandwidth analysis of the system shows that the system has a bandwidth of around 452 rad/s for a journal angular velocity of 500 rad/s. In order to make sure the system is excited within this region the bandpass filter is designed to have the lower cut-off frequency at 10 rad/s and upper cut-off frequency at 100 rad/s. The force input is shown in Figure 7.2 on the next page.

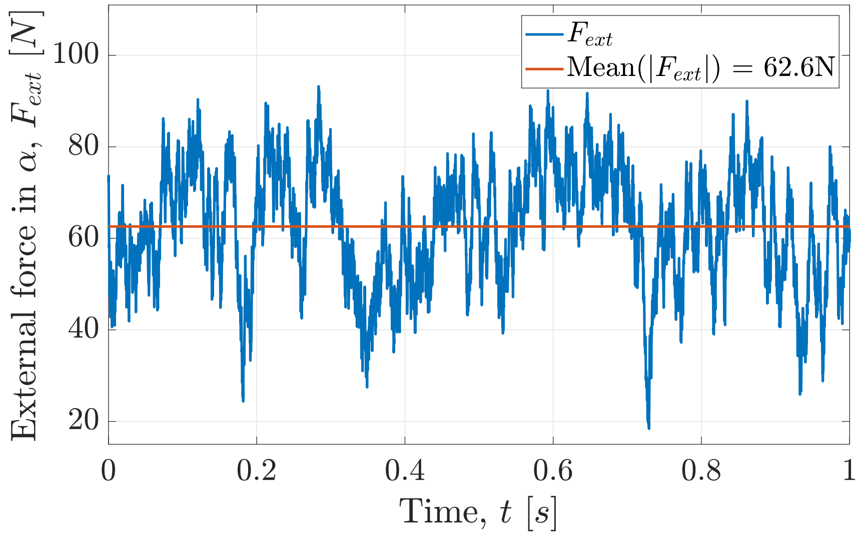

Figure 7.2: External force input used for the virtual experiments.

This force is chosen to be aligned with the α-axis during the tests of the TSOs.

7.2 Tuning

In the EKF algorithm several tuning parameters has to be found, these are the values in the covariance matrices of the sensor noise, process disturbance, and initial guess, $\underline{C}_n$, $\underline{C}_d$ and $\underline{P}_{c0}$, respectively. However, it is possible to quantify the values of $\underline{C}_n$ from experimental data, in order to simplify the tuning process.

7.2.1 Variance on ultrasound measurements

In order to determine the variance on the ultrasound measurements an acoustic simulation of the system, at different fluid film heights, is performed. The data has an added Gaussian white noise signal with a standard deviation of 1, since this is the noise added to the reflection wave measurements in the virtual experiments. The analysis takes offset in the variance between the frequency analysis of the data from a 1000 simulations for each fluid film height. The average variance at each fluid film height is seen in Figure 7.3 on the following page.

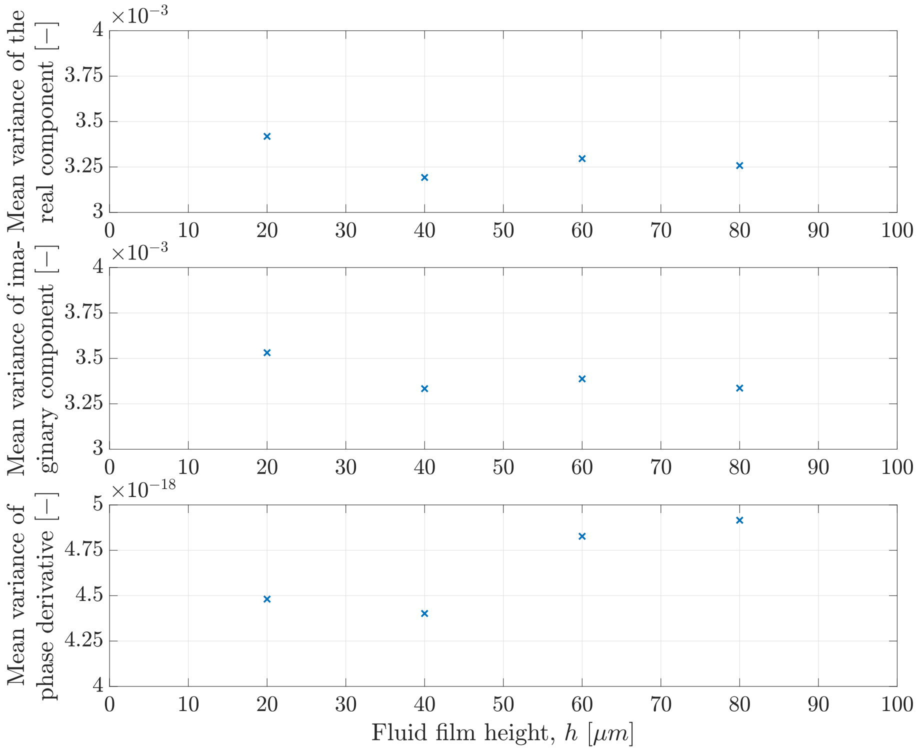

Figure 7.3: Variance analysis of the frequency response of the reflection wave measurements.

From the figure it is found that the average variance of the complex components are in the order of $\mathcal{O}(10^{-3})$ and the average variance of the phase derivative is in the order of $\mathcal{O}(10^{-18})$. These values are used in the tuning of $\underline{C}_n$.

7.2.2 Variance on temperature measurements

The temperature sensor used for the Thermoviscous CCTE TSO has an added Gaussian white noise with a standard deviation of 5 K. The variance of this is used in the tuning of $\underline{C}_n$.

7.2.3 Tuning parameters used for the TSOs

The tuning parameters for the TSOs are the diagonal elements of the covariance matrix of the sensor noise, process disturbance, and initial guess. The tuning has been limited to the diagonal elements of these matrices since it is assumed that no cross correlation is present between the states. The diagonal elements of the noise disturbance matrix is based on the parameters presented in the subsections above. The diagonal elements of C_d and P_{c0} are chosen such that the tracking capabilities of the TSO follows the fluid film height from the virtual experiments. The initial guess of the states are chosen to be in the same order of magnitude as the expected values.

The parameters used in the five different TSOs are given in Table 7.1 on the next page in vector form where the corresponding matrices are found from the equations below.

$$\underline{P}_{c0} = \underline{\mathcal{I}}\,\vec{P}_{c0} \quad (7.1) \qquad \underline{C}_d = \underline{\mathcal{I}}\,\vec{C}_d \quad (7.2) \qquad \underline{C}_n = \underline{\mathcal{I}}\,\vec{C}_n \quad (7.3)$$

Where $\mathcal{I}$ is the identity matrix.

Table 7.1: TSO tuning values.

	LSME	R. CCE	R. PDE	T. CCE	T. CCTE
$\vec{x}$	$\begin{bmatrix} Re(T_a) \\ Im(T_a) \end{bmatrix}$	$\begin{bmatrix} Re\left(T_{a,\alpha}\right) \\ Im\left(T_{a,\alpha}\right) \\ Re\left(T_{a,\beta}\right) \\ Im\left(T_{a,\beta}\right) \\ \epsilon \\ \dot{\epsilon} \\ \theta \\ \dot{\theta} \end{bmatrix}$	$\begin{bmatrix} \frac{d\angle T_{a,\alpha}}{d\omega} \\ \frac{d\angle T_{a,\beta}}{d\omega} \\ \epsilon \\ \dot{\epsilon} \\ \theta \\ \dot{\theta} \end{bmatrix}$	$\begin{bmatrix} Re\left(T_{a,\alpha}\right) \\ Im\left(T_{a,\alpha}\right) \\ Re\left(T_{a,\beta}\right) \\ Im\left(T_{a,\beta}\right) \\ \epsilon \\ \dot{\epsilon} \\ \theta \\ \dot{\theta} \\ \delta_b \end{bmatrix}$	$\begin{bmatrix} Re\left(T_{a,\alpha}\right) \\ Im\left(T_{a,\alpha}\right) \\ Re\left(T_{a,\beta}\right) \\ Im\left(T_{a,\beta}\right) \\ \epsilon \\ \dot{\epsilon} \\ \theta \\ \dot{\theta} \\ \delta_b \end{bmatrix}$
$\vec{x}_0$	$\begin{bmatrix} 1 \\ 1 \end{bmatrix}$	$\begin{bmatrix} 1 \\ 1 \\ 1 \\ 1 \\ 1 \cdot 10^{-5} \\ 0 \\ 1 \\ 0 \end{bmatrix}$	$\begin{bmatrix} 1 \cdot 10^{-6} \\ 1 \cdot 10^{-6} \\ 1 \cdot 10^{-5} \\ 0 \\ 1 \\ 0 \end{bmatrix}$	$\begin{bmatrix} 1 \\ 1 \\ 1 \\ 1 \\ 1 \cdot 10^{-5} \\ 0 \\ 1 \\ 0 \\ 11.9 \end{bmatrix}$	$\begin{bmatrix} 1 \\ 1 \\ 1 \\ 1 \\ 1 \cdot 10^{-5} \\ 0 \\ 1 \\ 0 \\ 11.9 \end{bmatrix}$
$\vec{y}$	$\begin{bmatrix} \lvert\vec{R_a}\rvert^2 \end{bmatrix}$	$\begin{bmatrix} Re\left(R_{a,\alpha}\right) \\ Im\left(R_{a,\alpha}\right) \\ Re\left(R_{a,\beta}\right) \\ Im\left(R_{a,\beta}\right) \end{bmatrix}$	$\begin{bmatrix} \frac{d\angle R_{a,\alpha}}{d\omega} \\ \frac{d\angle R_{a,\beta}}{d\omega} \end{bmatrix}$	$\begin{bmatrix} Re\left(R_{a,\alpha}\right) \\ Im\left(R_{a,\alpha}\right) \\ Re\left(R_{a,\beta}\right) \\ Im\left(R_{a,\beta}\right) \end{bmatrix}$	$\begin{bmatrix} Re\left(R_{a,\alpha}\right) \\ Im\left(R_{a,\alpha}\right) \\ Re\left(R_{a,\beta}\right) \\ Im\left(R_{a,\beta}\right) \\ T_{eq} \end{bmatrix}$
$\vec{P}_{c0}$	$\begin{bmatrix} 1 \\ 1 \end{bmatrix}$	$\begin{bmatrix} 1 \cdot 10^{6} \\ 1 \cdot 10^{6} \\ 1 \cdot 10^{6} \\ 1 \cdot 10^{6} \\ 0 \\ 0 \\ 0 \\ 0 \end{bmatrix}$	$\begin{bmatrix} 3 \cdot 10^{-6} \\ 3 \cdot 10^{-6} \\ 0 \\ 0 \\ 0 \\ 0 \end{bmatrix}$	$\begin{bmatrix} 1 \cdot 10^{6} \\ 1 \cdot 10^{6} \\ 1 \cdot 10^{6} \\ 1 \cdot 10^{6} \\ 0 \\ 0 \\ 0 \\ 0 \\ 1 \end{bmatrix}$	$\begin{bmatrix} 1 \cdot 10^{6} \\ 1 \cdot 10^{6} \\ 1 \cdot 10^{6} \\ 1 \cdot 10^{6} \\ 0 \\ 0 \\ 0 \\ 0 \\ 1 \end{bmatrix}$
$\vec{C}_d$	$\begin{bmatrix} 1 \cdot 10^{-6} \\ 1 \cdot 10^{-6} \end{bmatrix}$	$\begin{bmatrix} 1 \cdot 10^{-8} \\ 1 \cdot 10^{-8} \\ 1 \cdot 10^{-8} \\ 1 \cdot 10^{-8} \\ 0 \\ 1 \cdot 10^{-6} \\ 0 \\ 1 \end{bmatrix}$	$\begin{bmatrix} 0 \\ 0 \\ 0 \\ 1 \cdot 10^{-5} \\ 0 \\ 1 \end{bmatrix}$	$\begin{bmatrix} 1 \cdot 10^{-8} \\ 1 \cdot 10^{-8} \\ 1 \cdot 10^{-8} \\ 1 \cdot 10^{-8} \\ 0 \\ 1 \cdot 10^{-6} \\ 0 \\ 1 \\ 1 \cdot 10^{-6} \end{bmatrix}$	$\begin{bmatrix} 1 \cdot 10^{-8} \\ 1 \cdot 10^{-8} \\ 1 \cdot 10^{-8} \\ 1 \cdot 10^{-8} \\ 0 \\ 1 \cdot 10^{-6} \\ 0 \\ 1 \\ 1 \cdot 10^{-6} \end{bmatrix}$
$\vec{C}_n$	$\begin{bmatrix} 1 \end{bmatrix}$	$\begin{bmatrix} 3.5 \cdot 10^{-3} \\ 3.5 \cdot 10^{-3} \\ 3.5 \cdot 10^{-3} \\ 3.5 \cdot 10^{-3} \end{bmatrix}$	$\begin{bmatrix} 4.5 \cdot 10^{-18} \\ 4.5 \cdot 10^{-18} \end{bmatrix}$	$\begin{bmatrix} 3.5 \cdot 10^{-3} \\ 3.5 \cdot 10^{-3} \\ 3.5 \cdot 10^{-3} \\ 3.5 \cdot 10^{-3} \end{bmatrix}$	$\begin{bmatrix} 3.5 \cdot 10^{-3} \\ 3.5 \cdot 10^{-3} \\ 3.5 \cdot 10^{-3} \\ 3.5 \cdot 10^{-3} \\ 25 \end{bmatrix}$

7.3 Regular TSO and LSME

The first test is based on the comparison of the Reguler CCE and PDE versus the LSME algorithm. The tests also consider how the placement of the ultrasound transducer might affect the state estimation abilities.

7.3.1 Ultrasound transducer placement

An important part of the TSO strategies proposed is that the incident wave have to be slow varying compared to the fluid film height. It is for this reason that two instances of ultrasound placement on the journal bearing is analysed. The previous study of the same authors proposed placing the ultrasound transducer on the outside of the bushing at 90° apart as seen in Figure 7.4a [12]. A study from Beamish et al. [1] however proposed placing the ultrasound transducer within the journal. This study therefore also investigates this scenario where two ultrasound transducers are placed 90° apart within the journal as seen in Figure 7.4b.

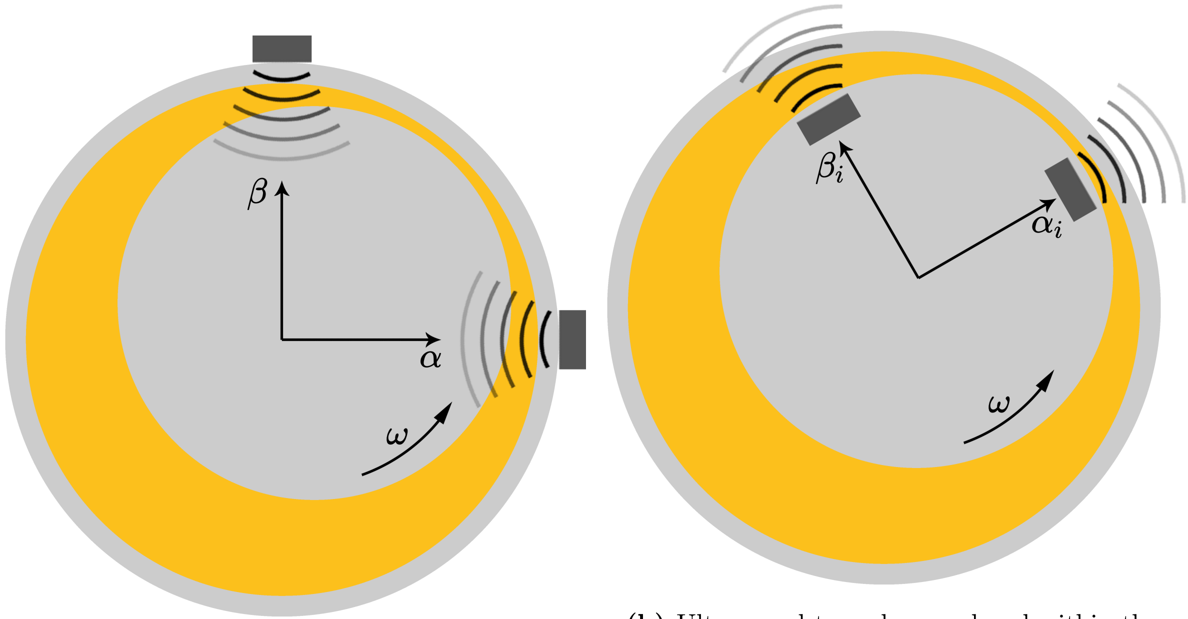

(a) Ultrasound transducers placed on the bushing

(b) Ultrasound transducers placed within the journal

Figure 7.4: Ultrasound transducer placement strategies.

The apparent advantage of placing the ultrasound transducer within the journal is that even though there might be limited mechanical dynamics, the fluid film height seen from the ultrasound transducer varies by twice the eccentricity for a full rotation of the journal. The apparent disadvantage is that depending on the application of interest it might be more difficult or implausible to install the ultrasound transducers within the journal. It is for these reasons that both strategies are investigated in this study.

7.3.2 Results from ultrasounds transducer placed on the bushing

In the test of the TSOs, the TSOs are given the baseline system values. This means that the dynamic viscosity and reflection coefficient used in the TSOs are evaluated at 313.2 K, where the virtual experiments have an average fluid film temperature of 316.0 K. The fluid film height estimate in the α- and β-direction when the ultrasound transducer is placed on the bushing is seen in Figure 7.5.

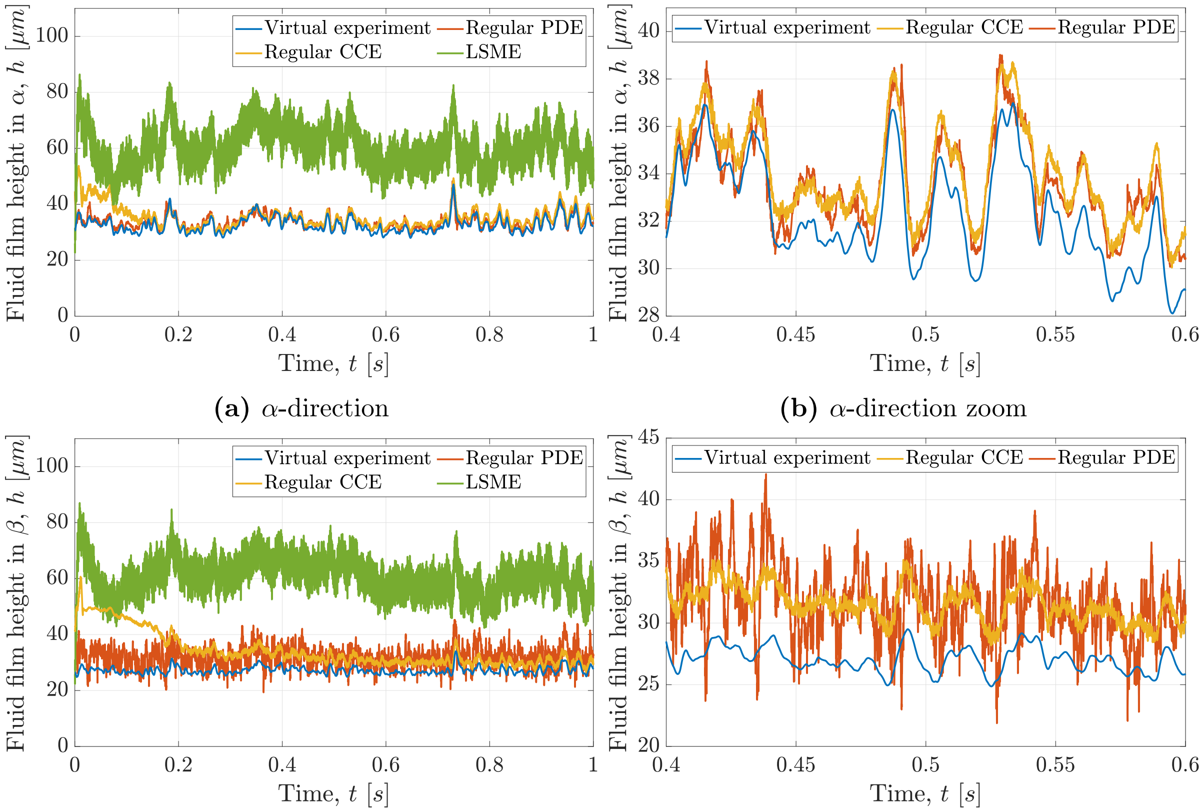

(a) α-direction **(b)** α-direction zoom

(c) β-direction **(d)** β-direction zoom

Figure 7.5: Fluid film height in the α- and β-direction.

Figure 7.5 shows that of the methods presented the LSME algorithm has the largest deviation from the virtual experiment. It is seen that the LSME deviates around 30 µm but the dominant fluctuations are present, such as the large spike at around 0.75 s. It is from Figure 7.5a and Figure 7.5c seen that the Regular PDE algorithm has a significantly larger noise level in the β-direction compared to the α-direction. This might be due to the excitation in the fluid film height is larger in the α-direction, and the algorithm is for this reason more likely to properly converge. It is from Figure 7.5b seen that in the α-direction the Regular PDE deviates less than the Regular CCE. From Figure 7.5d the Regular CCE is however seen to be more robust than the Regular PDE, where the noise level is significantly lower. It is from the figure seen that the Regular CCE has less deviation from the virtual experiment in the α-direction compared to the β-direction. This might be due to the larger excitation in the fluid film height in the α-direction, making the incident wave estimate more consistent.

Figure 7.6 on the following page shows the eccentricity and eccentricity angle for the Regular CCE and Regular PDE algorithm. These algorithms are TSO algorithms and for this reason outputs estimates of these states.

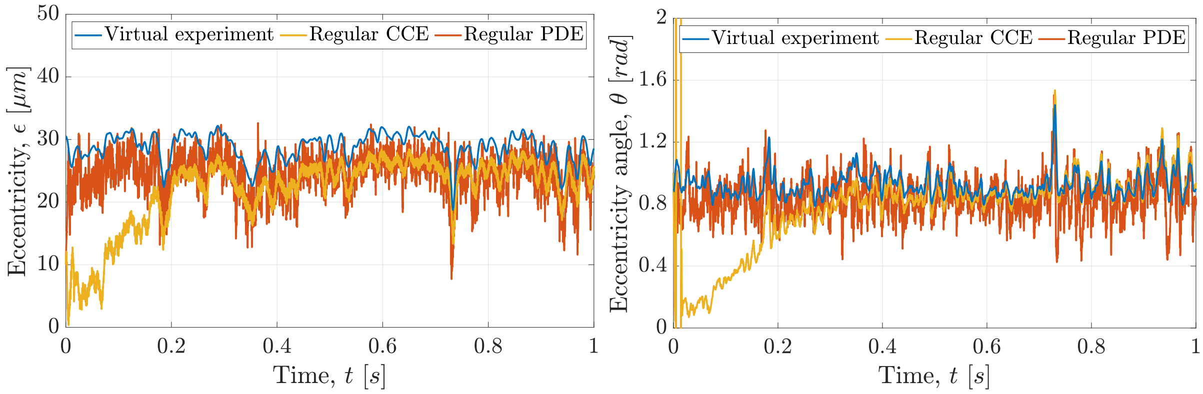

(a) Eccentricity **(b)** Eccentricity angle

Figure 7.6: Eccentricity and eccentricity angle when the ultrasound transducer is placed on the bushing.

Figure 7.6 shows significantly less noise levels on the Regular CCE algorithm compared to the Regular PDE algorithm. It is from the figure seen that eccentricity angle fits the virtual experiment well, especially for the Regular CCE algorithm. A slight offset in the eccentricity is however present. This might be due to the analytical models predicting the eccentricity angle better than the eccentricity as discussed in Section 4.6 on page 28.

Figure 7.7 on the next page shows the percent deviation of the incident wave estimate for the different algorithms.

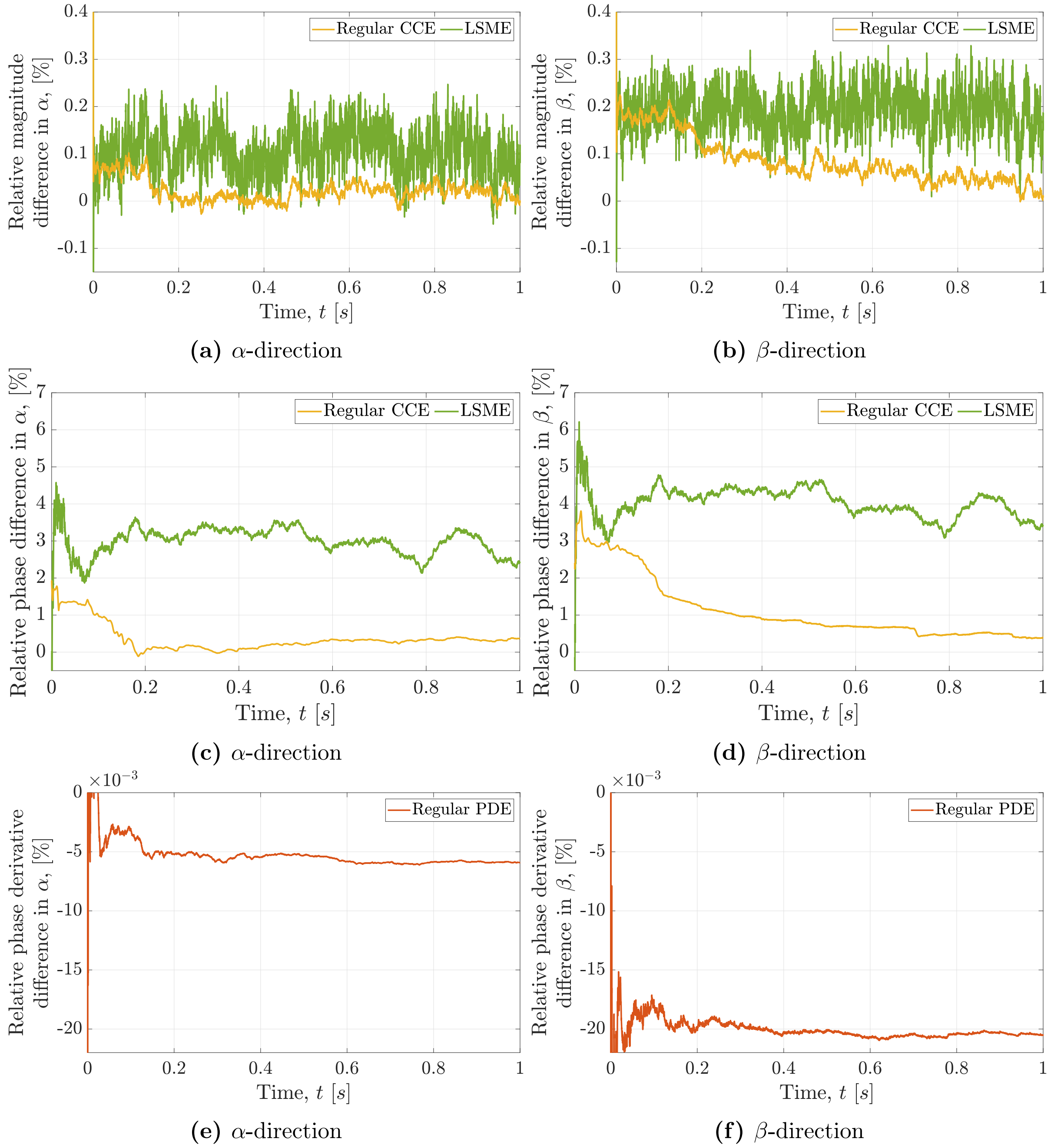

(a) α-direction **(b)** β-direction **(c)** α-direction **(d)** β-direction **(e)** α-direction **(f)** β-direction

Figure 7.7: Error in incident wave estimation.

Figure 7.7a to Figure 7.7d, shows that the LSME algorithm has significantly smaller deviations in estimating the magnitude of the incident wave than the phase estimate. It is also seen that the LSME algorithm has significantly worse estimate of the incident wave compared to the Regular CCE algorithm. Figure 7.7e and Figure 7.7f shows that the percentage deviation in the phase derivative estimate of the incident wave from the Regular PDE is in the order of $\mathcal{O}(10^{-2})$ in the β-direction. However, due to the large noise levels on fluid film height in the β-direction it is believed that a small deviation has a large affect.

7.3.3 Results from ultrasound transducer placed in the journal

Figure 7.8 shows the fluid film height in the α_i- and β_i-direction when the ultrasound transducer is placed within the journal.

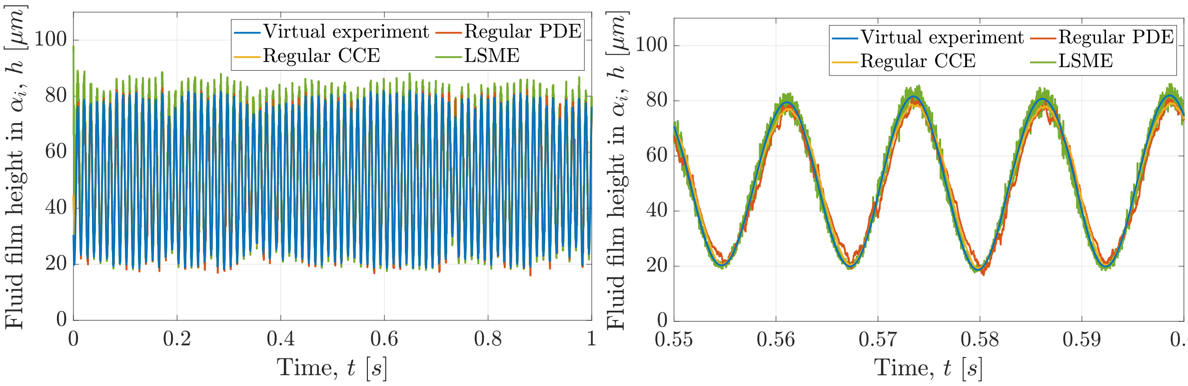

(a) α_i-direction **(b)** α_i-direction zoom

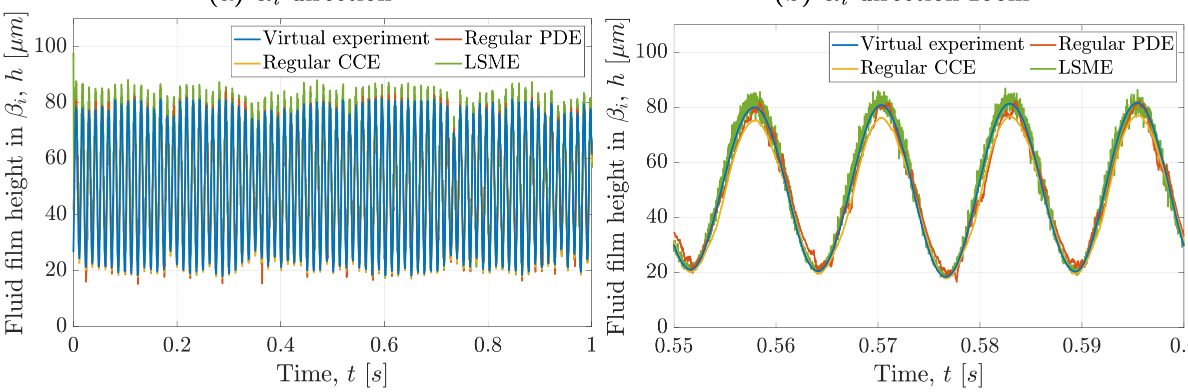

(c) β_i-direction **(d)** β_i-direction zoom

Figure 7.8: Fluid film height in the α_i- and β_i-direction.

Figure 7.8 show that placing the ultrasound transducer within the journal causes a significant change in the fluid film height which results in fluid film height estimates from the LSME algorithm to have a max deviation of around 10 µm. This deviation is especially notable when the fluid film height is large. It is from Figure 7.8b and Figure 7.8d seen that the deviation of the fluid film height estimate from the Regular CCE is also larger when the fluid film height is large. This tendency is however not noticeable for the Regular PDE algorithm. It is from Figure 7.8, seen that placing the ultrasound transducer within the journal result in improved fluid film height estimates from all three algorithms, compared to placing the ultrasound transducer on the bushing.

Figure 7.9 on the next page shows the eccentricity and eccentricity angle estimates when the ultrasound transducer is placed inside the journal.

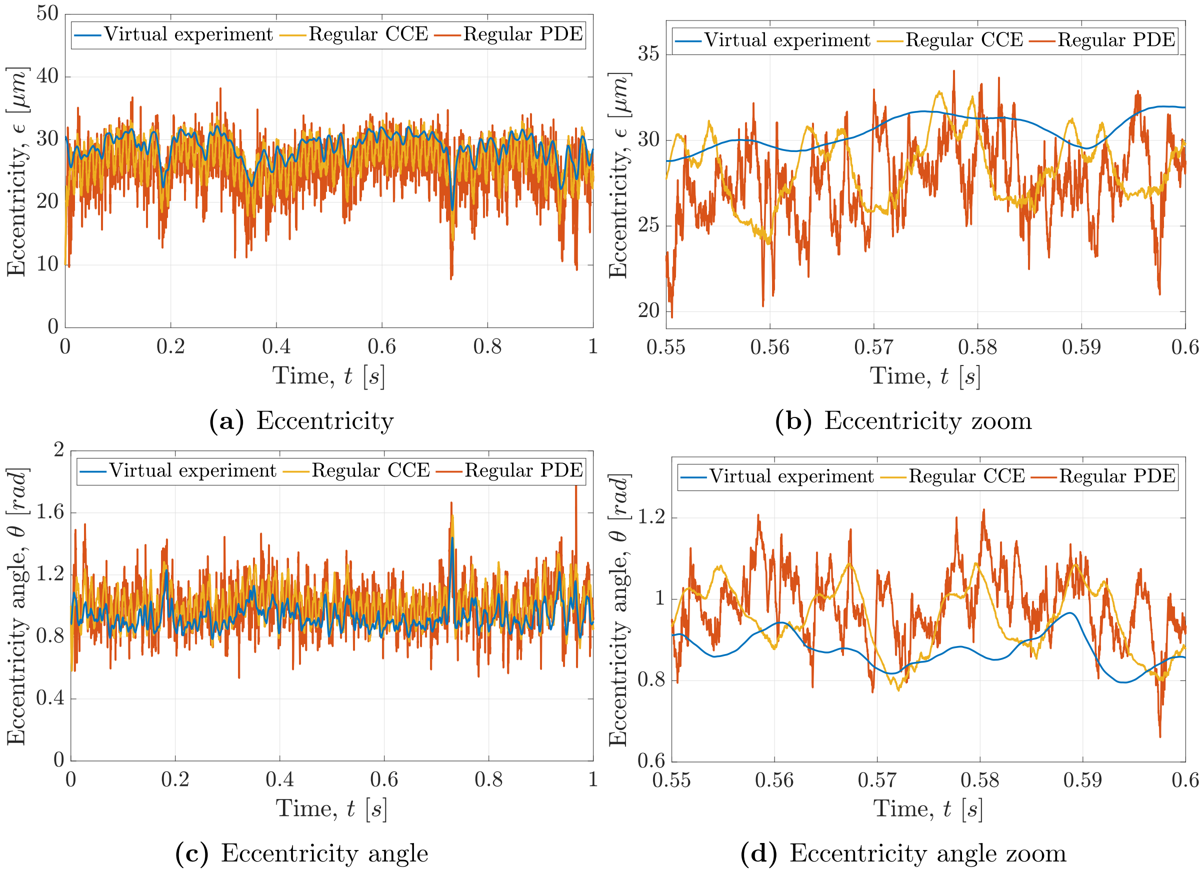

(a) Eccentricity **(b)** Eccentricity zoom

(c) Eccentricity angle **(d)** Eccentricity angle zoom

Figure 7.9: Eccentricity and eccentricity angle when the ultrasound transducer is placed inside the journal.

It is from the figure seen that both the Regular CCE and PDE has significantly larger noise levels on the eccentricity and eccentricity angle estimates, compared to the estimates where the journal is placed on the bushing. It is however seen from Figure 7.8b, Figure 7.8d on the facing page, and Figure 7.9b, that when the fluid film height is small, for either sensor, the eccentricity estimate from the Regular CCE is seen to fit the virtual experiment, especially notable at 0.59 s. When the fluid film height is large, the eccentricity estimate is seen to generally be lower than in the virtual experiment. This indicates that the Regular CCE might be better at estimating the incident wave when the fluid film height is small, and otherwise tends to the pure model output found, in Section 4.6 on page 28, to estimate a too small eccentricity.

From Figure 7.9c and Figure 7.9d it is seen that deviations in the eccentricity estimates are smaller when the fluid film height is large. This might be due to the TSO output tends to the pure model output found, in Section 4.6 on page 28, to estimate the eccentricity angle to a satisfying degree.

Figure 7.10 on the following page shows the percent deviation of the incident wave estimate for the different algorithms.

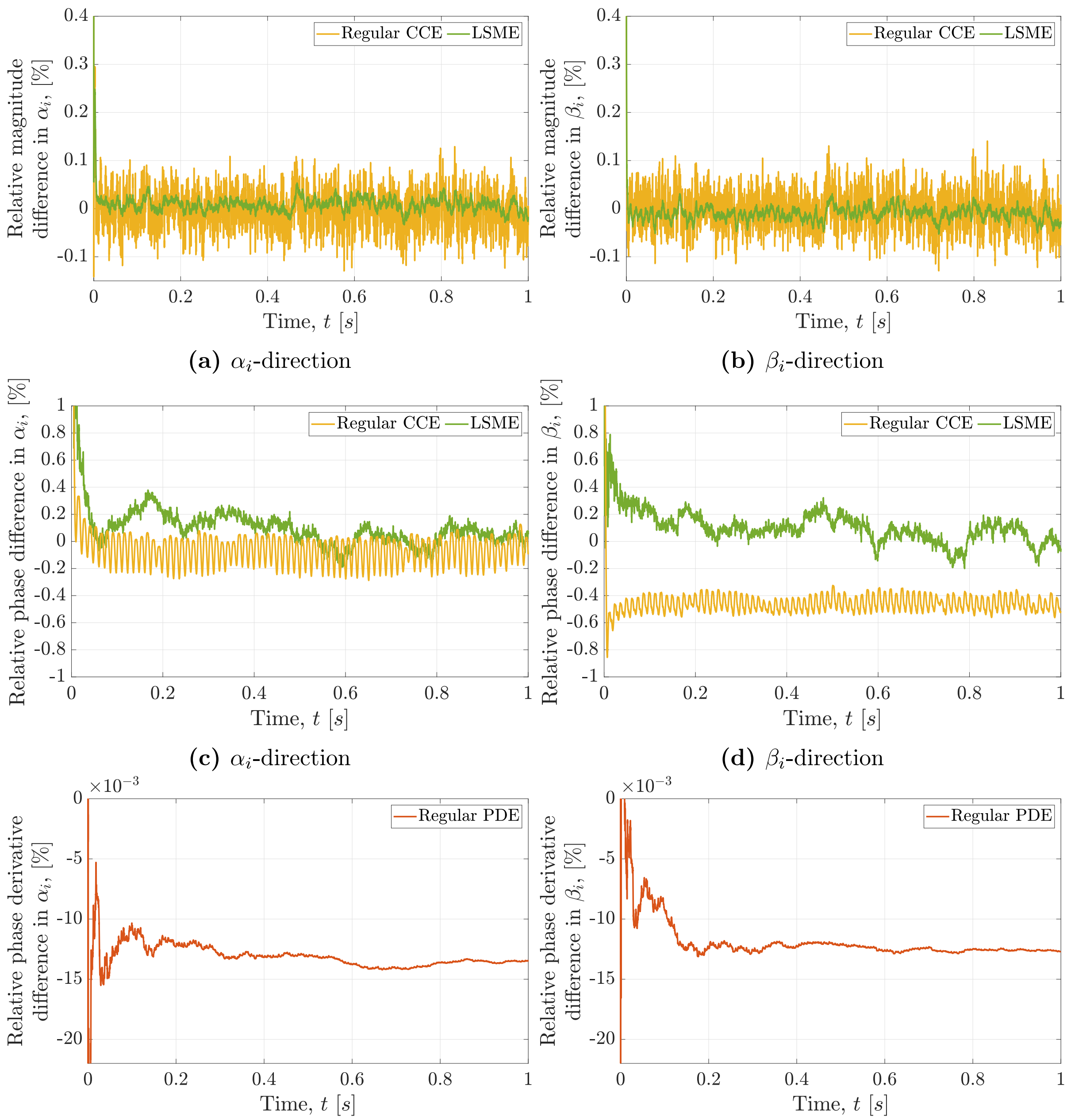

(a) α_i-direction

(b) β_i-direction

(c) α_i-direction

(d) β_i-direction

(e) α_i-direction

(f) β_i-direction

Figure 7.10: Incident wave estimation error.

Comparing Figure 7.10a - 7.10d to Figure 7.7a - 7.7d on page 57, it is seen that LSME algorithm has significantly lower deviations in the phase and magnitude estimate of the incident wave when the ultrasound transducer is placed inside the journal. This is likely due to the larger level of excitation in the fluid film height that occur when the ultrasound transducer is placed inside the journal. These figures also show that the Regular CCE has a much lower transient period in the incident wave estimate when the ultrasound transducer is placed inside the journal, compared to when it is placed on the bushing. Figure 7.10e and Figure 7.10f show that the Regular PDE has a similar deviation in phase derivative estimate of the incident wave regardless of whether the ultrasound transducer is placed inside or on the journal bearing.

The previous study from the same authors shows a sensitivity analysis of the phase of the layer spectrum that is able to explain why the LSME and Regular CCE have difficulties estimating the fluid film height when it becomes too large. [12]

7.3.4 Sensitivity analysis of the layer spectrum

The sensitivity analysis takes offset in the formulation of the reflection coefficient spectrum given in the following equation.

$$R(\omega) = A(\omega)\ (cos(\gamma(\omega)) + i\, sin(\gamma(\omega))) = \frac{T_a(\omega)}{R_a(\omega)} \tag{7.4}$$

In this equation the magnitude and phase of the reflection coefficient spectrum is given as $A(\omega)$ and $\gamma(\omega)$, respectively. It is from the above equation seen that the magnitude and phase of the reflection coefficient spectrum relates to the error in estimating the incident wave but also noise on the measured reflection wave.

It is from the following equation seen that the reflection coefficient spectrum relates to the layer spectrum.

$$J(\omega) = e^{-i\omega\tau} = \frac{1}{R_{bc}} \frac{R_{ab} - R(\omega)}{R_{ab}\, R(\omega) - 1} \tag{7.5}$$

It is from this equation seen that it is the phase of the layer spectrum that relates to the fluid film height and it is for this reason the sensitivity function is defined as the following equation.

$$S = \frac{\left|\frac{\partial \angle J(\omega)}{\partial \gamma(\omega)}\right|}{\left|\frac{\partial \angle J(\omega)}{\partial A(\omega)}\right|} \tag{7.6}$$

This equation is related to the sensitivity of the CCE and LSME algorithms, since these algorithms is based on determining the angle of the layer spectrum for use in determining the complex components of the incident wave.

The logarithmic sensitivity function is shown in Figure 7.11. In the figure the logarithmic sensitivity is plotted as a function of fluid film height. This relation is found from the regression model used in LSME methods, eq. (6.13), and the full derivation is shown in Appendix F on page 111.

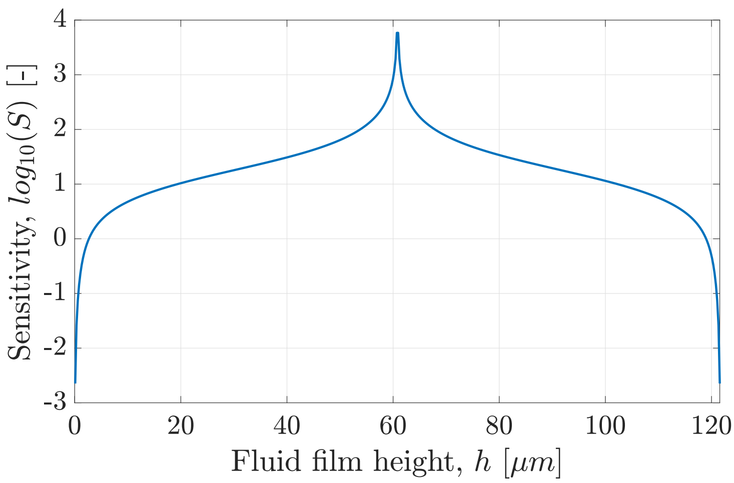

Figure 7.11: Sensitivity analysis with the baseline values.

Figure 7.11 on the previous page shows that the layer phase lag is more sensitive to error in the phase of the reflection coefficient spectrum, for fluid film heights in range of around 5 µm to around 115 µm. The figure also show that sensitivity peaks at approximately half the resonance height. The resonance height is defined from the layer spectrum, when the layer spectrum equals one.

Figure 7.11 on the preceding page explains why the fluid film height estimates from the LSME and CCE algorithms worsen as the fluid film height becomes large. This is due to phase of the layer spectrum becomes more sensitive to errors in the phase of the reflection coefficient spectrum.

7.3.5 Sub conclusion

This preliminary analysis of the placement of the ultrasound transducers shows that for the LSME algorithm, placing the transducer within the journal, and hereby increasing the excitement level of the fluid film height, increases accuracy and robustness of the fluid film height estimation. It is from the results seen that the estimate worsens as the fluid film height increases, thought to be due to the sensitivity of the LPL algorithm.

This analysis shows that generally the Regular CCE has lower noise levels than the Regular PDE and LSME algorithms. It is from the results with the ultrasound transducer placed on the bushing seen that when there is not enough excitement in the fluid film height the Regular CCE tends towards the pure system model output, and disregards the ultrasound measurements. Depending on the accuracy of the system model, this is a more robust solution for determining the fluid film height compared to the LSME algorithm. This is because when there is not enough excitement in the fluid film height the LSME algorithm is seen to have large deviation from the virtual experiment.

The Regular CCE and PDE methods are found to have very accurate fluid film height measurements when the ultrasound transducer is placed inside the journal. It is however found that both methods have difficulties determining small fluctuations in the mechanical state estimates. With the exception of the Regular CCE algorithm, that depicts the eccentricity accurately when the fluid film height is small. A probable explanation to this is that when the fluid film height is small the ultrasound transducer points in the direction with least fluid film height, which is the direction from which the eccentricity is defined.

It is from the tuning of the Regular PDE found that the fluid film height estimate is largely dependent on an accurate depiction of the system parameters, such as the dynamic viscosity, within the system model. This is not found to be a problem for the Regular CCE method. Furthermore, it has not from tuning and design process of the TSO been possible to use joint state and parameter estimation for determining the dynamic viscosity from the Regular CCE and PDE algorithm.

It is from this analysis assessed that the CCE criterion is superior compared to the PDE criterion. However, this analysis and conclusion is based on a complex tuning process for the TSO strategies, and further investigation into the PDE algorithm might be required. Furthermore an investigation into combining the CCE and PDE algorithm might be of interest to enhance the accuracy and robustness of the algorithm.

7.4 Thermoviscous TSO

The CCE criterion is used for the thermoviscous system model, since this criterion is deemed superior. Furthermore the thermoviscous TSO strategies are only tested with the ultrasound transducer placed inside the journal. The thermoviscous TSO test includes a strategy with and without temperature sensor measurements, Thermoviscous CCTE and CCE, respectively.

Figure 7.12 show the fluid film height estimate from both the Thermoviscous CCE and CCTE algorithm.

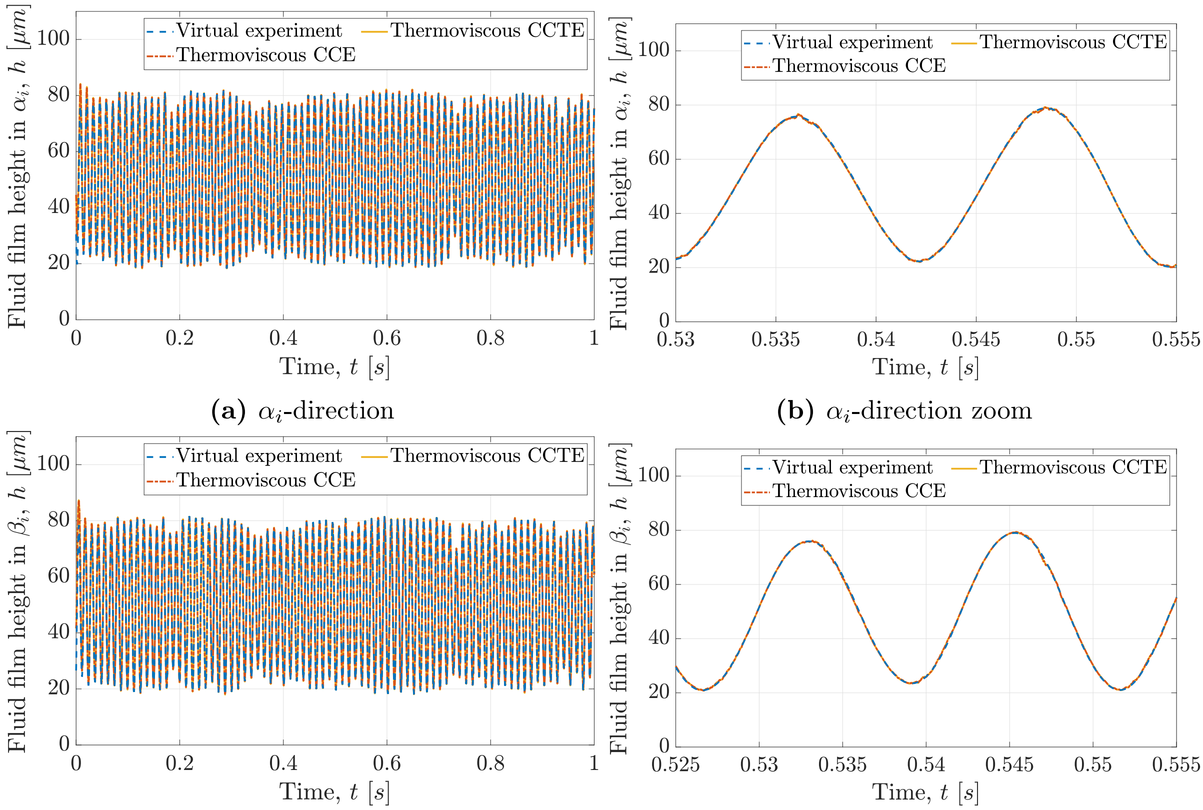

(a) α_i-direction
(b) α_i-direction zoom
(c) β_i-direction
(d) β_i-direction zoom

Figure 7.12: Fluid film height estimate in the α_i- and β_i-direction using the thermoviscous system model.

It is from Figure 7.12 seen that both the Thermoviscous CCE and CCTE algorithm estimates the fluid film height with great accuracy, compared to the Regular CCE algorithm.

Figure 7.13 on the next page shows the eccentricity and eccentricity angle estimate for the Thermoviscous CCE and CCTE algorithm.

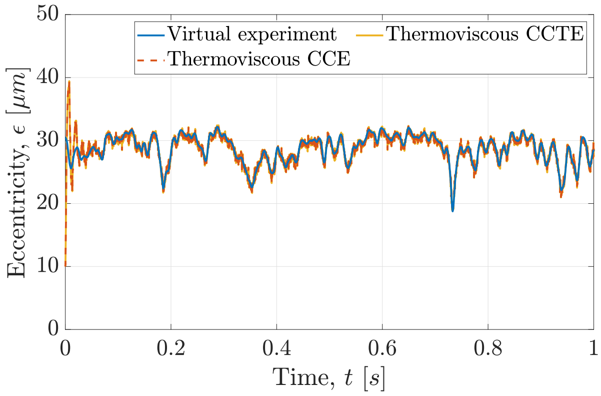

(a) Eccentricity

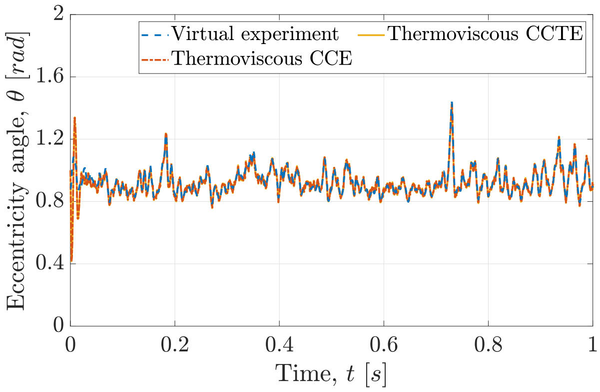

(b) Eccentricity angle

Figure 7.13: Eccentricity and eccentricity angle when the ultrasound transducer is placed inside the journal and using the thermoviscous system model.

It is from Figure 7.13 seen that after the initial transient period the state estimates are similar to those of the virtual experiment. It is seen that there is a slight noise level on the eccentricity estimate, but comparably better than those using the regular Reynolds pressure equation. A reason for the very similar system dynamics might be that the thermoviscous TSO strategies allow for a change in boundary fluidity that compensates for the difference between the dynamics is the virtual experiment and the system model.

Figure 7.14 shows the boundary fluidity estimate from the TSO strategies. It is notable that in the figure the fluidity is represented as dynamic viscosity and that the estimate is compared to the spacial average viscosity from the virtual experiment.

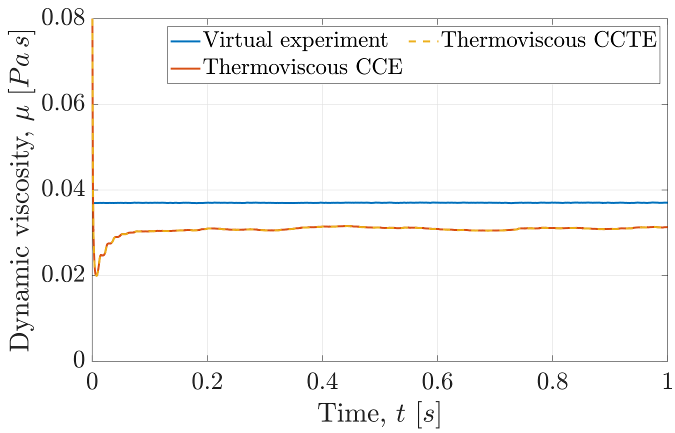

Figure 7.14: Dynamic viscosity estimate compared to the mean viscosity of the virtual experiment.

It is from Figure 7.14 seen that the viscosity estimates from the Thermoviscous CCE and CCTE are very similar. This might be due to the tuning of the algorithms. Since the CCTE has relatively large standard deviation on the temperature sensor noise and uses Reynold's viscosity model, the temperature estimate might be so inaccurate, that the algorithm is fitted such that the best results are achieved by not trusting the measurement data.

It is from Figure 7.14 seen that there is an offset between the estimated viscosity and the one from the virtual experiment. This offset might be due to the TSO strategies compensating for discrepancies between the models used for the virtual experiment and the analytical thermoviscous system model, such as the short bearing approximation and thermally thin approximation. Even though there is an offset in the viscosity estimate, it might still be possible to track changes in the viscosity using the Thermoviscous TSO strategies.

Figure 7.15 shows the percent deviation in magnitude and phase estimate of the incident wave in the α_i- and β_i-direction.

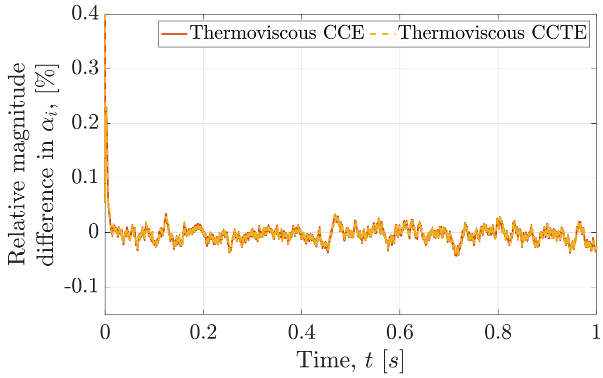

(a) α_i-direction

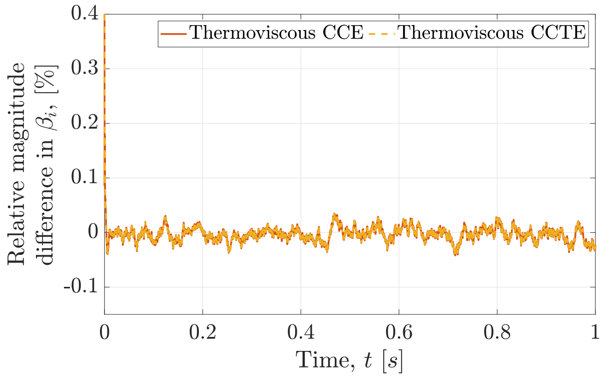

(b) β_i-direction

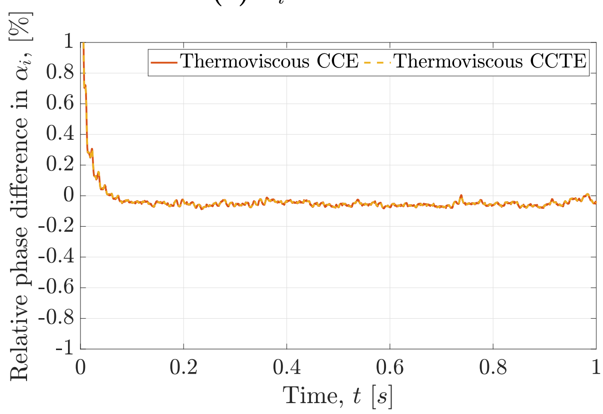

(c) α_i-direction

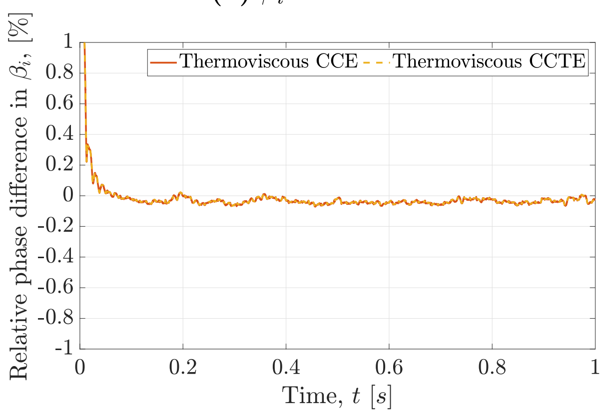

(d) β_i-direction

Figure 7.15: Percent deviation in magnitude and phase estimate of the incident wave, using the thermoviscous system model.

Figure 7.15 shows that compared to the Regular CCE algorithm the thermoviscous TSO strategies have small deviations and noise levels on the incident wave estimate. The difference between the Thermovicous CCE and CCTE is again shown to be insignificant.

This analysis of the thermoviscous TSO strategies show no significant difference between the CCE and CCTE criteria. Due to this and since the CCE algorithm is more simple compared to the CCTE algorithm, the CCTE algorithm is excluded from further analysis in this study.

7.4.1 Varying dynamic viscosity

In order to test if the Thermoviscous CCE algorithm is able to detect a change in dynamic viscosity a virtual experiment is conducted where the a_{bv} parameter in the Barus-Vogel model, given in the equation below, is ramped to twice the default value.

$$\mu_{bv} = a_{bv}\, e^{A(T)}\, e^{B(T,p)} \tag{7.7}$$

Figure 7.16 shows the spatially mean viscosity from the virtual experiment and the boundary viscosity estimate from the Thermoviscous CCE algorithm.

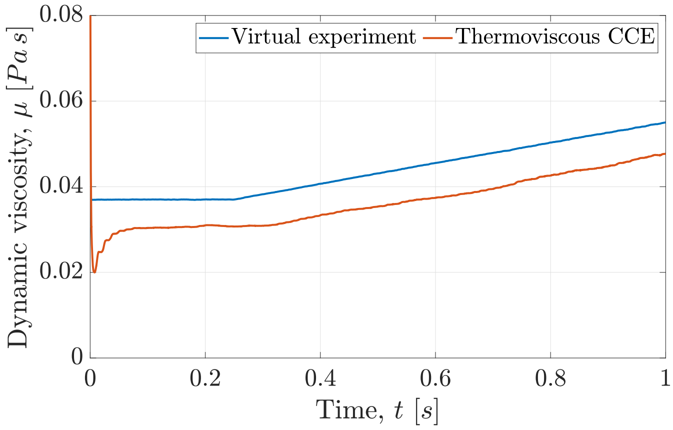

Figure 7.16: Virtual experiment where the dynamic viscosity is varied.

It is seen from Figure 7.16 that after the initial transient period the viscosity is underestimated with at constant offset, as for the previous experiment. It is seen that when the viscosity start to increase, the viscosity estimate also increases with the approximately same slope.

Figure 7.17 shows the fluid film height from the virtual experiment and the estimate from the Thermoviscous CCE algorithm.

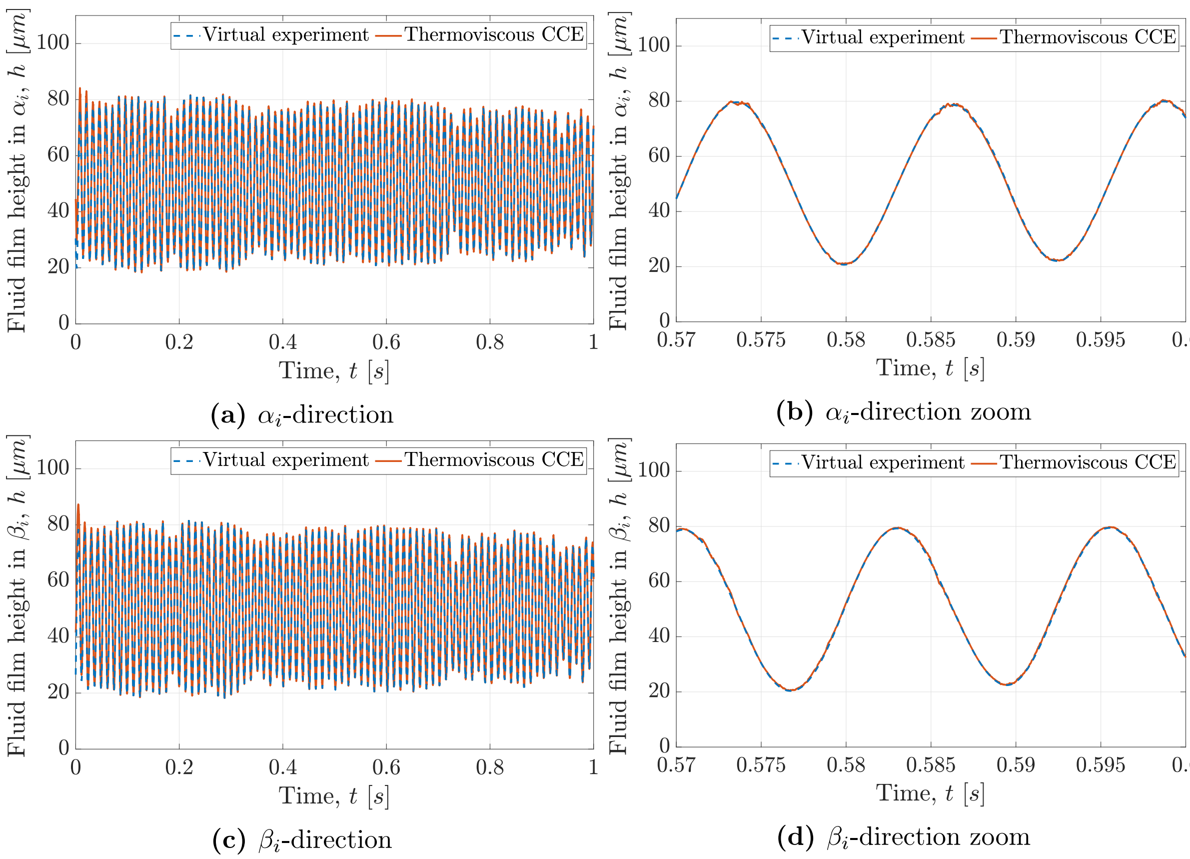

Figure 7.17: Fluid film height for the virtual experiment with varying viscosity.

Figure 7.17a on the preceding page and Figure 7.17c on the facing page show that when the viscosity changes the peaks of the fluid film height decreases. It is from Figure 7.17 on the preceding page seen that after the initial transient period the Thermoviscous CCE algorithm estimates the fluid film height to a satisfying degree.

Figure 7.18 shows the eccentricity and eccentricity angle from the virtual experiment and the estimate from the Thermoviscous CCE.

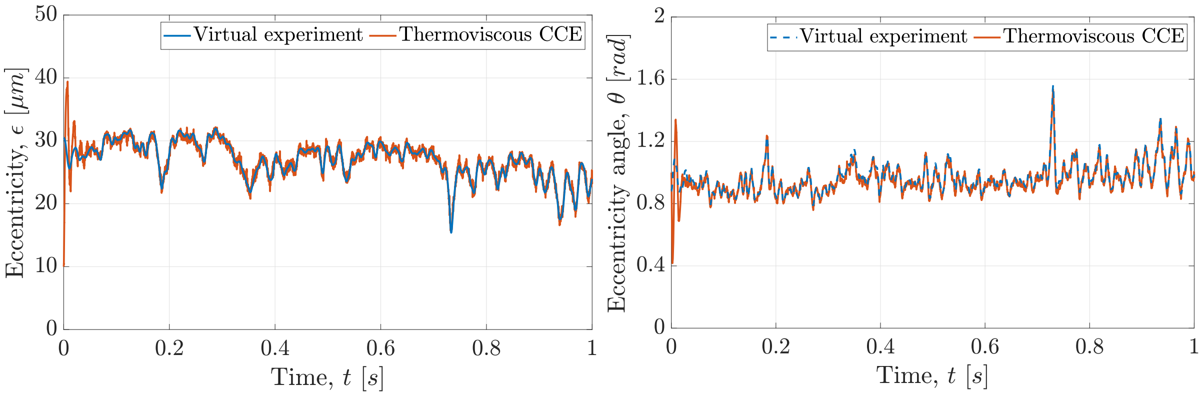

(a) Eccentricity **(b)** Eccentricity angle

Figure 7.18: Eccentricity and eccentricity angle for the virtual experiment with varying viscosity.

It is from Figure 7.18 seen that after the initial transient period the eccentricity and eccentricity angle are estimated to a satisfying degree. It is from Figure 7.18a seen that similar to the other test of the Thermoviscous TSO strategies that the eccentricity estimate has a slight noise level.

It is from this analysis seen that the Thermoviscous CCE is able to track changes in the dynamic viscosity, and it is for this reason believed that the algorithm shows great promise for use in prognostic control schemes and predictive maintenance. However, since the boundary fluidity is seen to compensate for model differences, wear on other system parameters is also seen to affect this estimate.

7.4.2 Varying the radial clearance

The radial clearance is another system parameter that is susceptible to wear. A virtual experiment where the radial clearance changes from 50 µm to 60 µm is for this reason conducted. The radial clearance and the corresponding dynamic viscosity estimate is seen in Figure 7.19 on the next page.

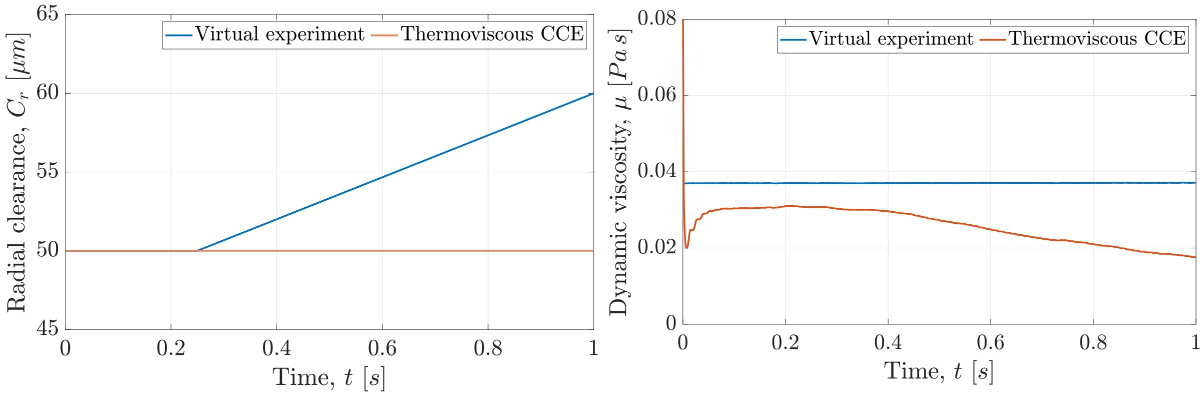

(a) Radial clearance **(b)** Dynamic viscosity

Figure 7.19: Clearance and dynamic viscosity estimate, for the virtual experiment with varying radial clearance.

It is from Figure 7.19 seen that when the radial clearance increases the Thermoviscous CCE algorithm compensated for this by lowering the viscosity estimate. This is an inherent problem with the proposed Thermoviscous CCE algorithm.

Figure 7.20 shows the fluid film height from the virtual experiment and the corresponding estimate from the Thermoviscous CCE algorithm.

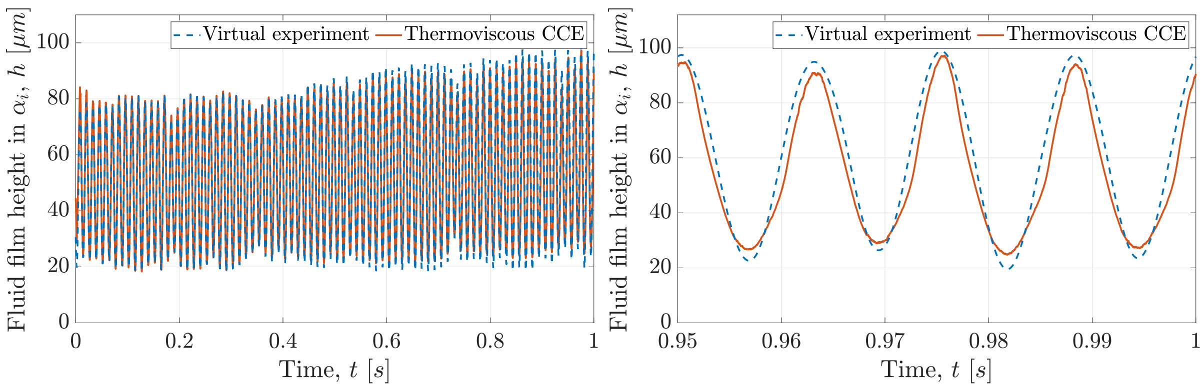

(a) α_i-direction **(b)** α_i-direction zoom

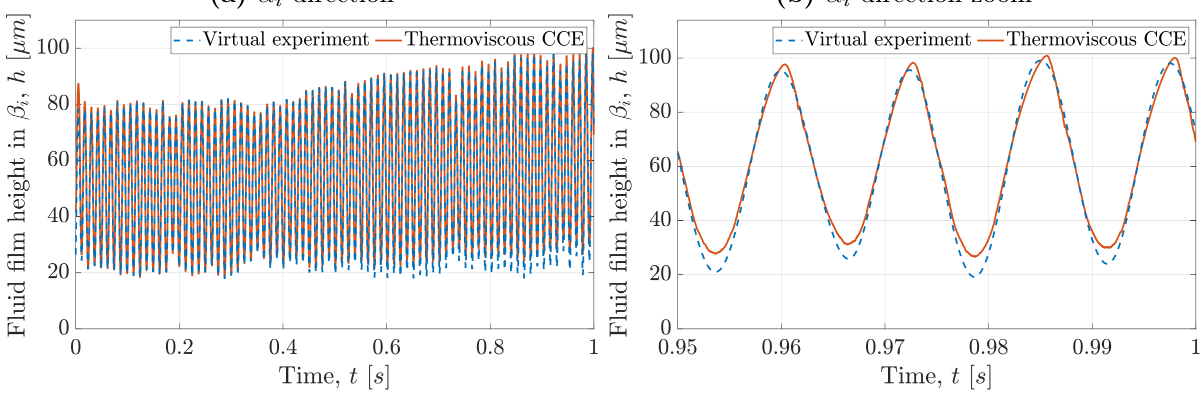

(c) β_i-direction **(d)** β_i-direction zoom

Figure 7.20: Fluid film height for the virtual experiment with varying radial clearance.

It is from Figure 7.20 seen that when the radial clearance becomes significantly different from the parameter used in the Thermoviscous CCE algorithm, the fluid film height estimate starts to deviate significantly from the actual fluid film height. This indicates that the Thermoviscous CCE algorithm might be sensitive to error in the radial clearance estimate given to the system model.

Figure 7.21 shows the eccentricity and eccentricity angle from the virtual experiment and the corresponding estimate from the Thermoviscous CCE algorithm.

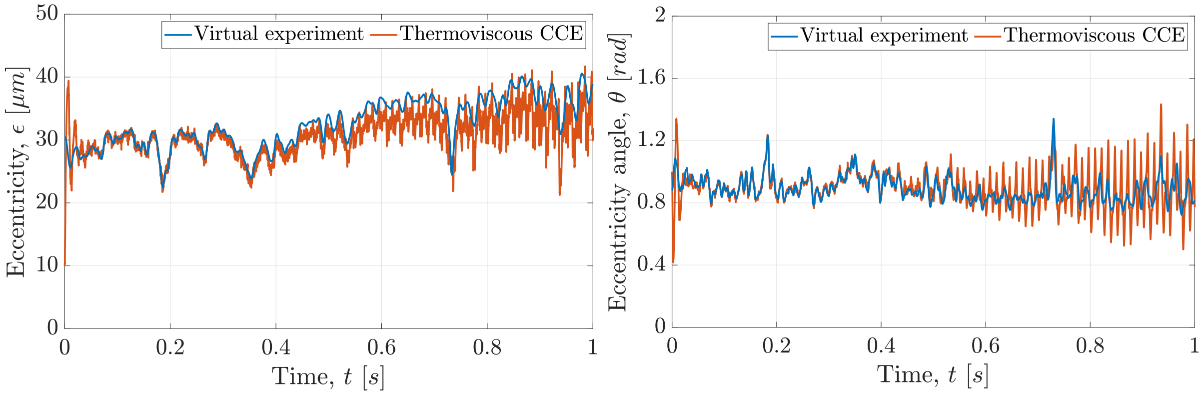

(a) Eccentricity

(b) Eccentricity angle

Figure 7.21: Eccentricity and eccentricity angle for the virtual experiment with varying radial clearance.

It is from Figure 7.21 seen that when the radial clearance start to change the eccentricity and eccentricity angle estimates significantly deviates from the actual states. It is from this seen that the radial clearance changes the system dynamics in a way where the changing boundary viscosity is not able to compensate for the model differences. Since the radial clearance changes the system dynamics in a way that can not be compensated by adjusting the boundary fluidity, it might be possible to add the radial clearance as a slow varying state in the Thermovisouc CCE algorithm, and from this estimate both boundary fluidity and radial clearance based on observation of the mechanical system dynamics.

7.4.3 Sub conclusion

It is from this analysis seen that the thermoviscous system model greatly improves the CCE algorithm, compared to the regular Reynolds model. In this analysis it is found that adding temperature measurements to the algorithm does not increase the accuracy or robustness of the TSO. However, both the viscosity model and temperature measurements might be less than ideal, compared to the performance of the TSO strategies on an experimental setup, where other viscosity models might be more accurate. The Thermoviscous CCTE methods require for these reason a more in-depth investigation.

It is from the analysis seen that the Thermoviscous CCE algorithm uses the boundary viscosity estimate to compensate for model differences. This means that if the viscosity of the system is changed, for example from wear of the hydraulic oil, it is possible to track changes in the viscosity. It is however also found that if other parameters are changed, such as the radial clearance, the viscosity estimate also tries to compensate for this. It is found that these changes of other parameters are indistinguishable from an actual change in viscosity. A change in radial clearance is found to cause changes to the system dynamics that is not fully compensated with a change in the viscosity estimate. This means that it might be possible to add the radical clearance as a slow varying state to the TSO algorithm and estimate both boundary viscosity and radial clearance.

7.5 State estimation algorithm using LSME

In Section 7.3.3 on page 58 it is found advantageous to place the transducers inside the journal. By placing the transducers inside the journal the fluid film height is measured at different angles during one revolution of the journal. This allows for the estimation of the clearance, eccentricity, and eccentricity angle from the LSME and encoder measurements, as seen in the flow diagram of the LSME state estimation algorithm in Figure 7.22. The apparent advantage of using the LSME algorithm for state estimation, is that it does not require any information of the system inputs. Furthermore, there is fewer system parameters needed for the algorithm than those required for the TSO strategies, and there is fewer tuning parameters.

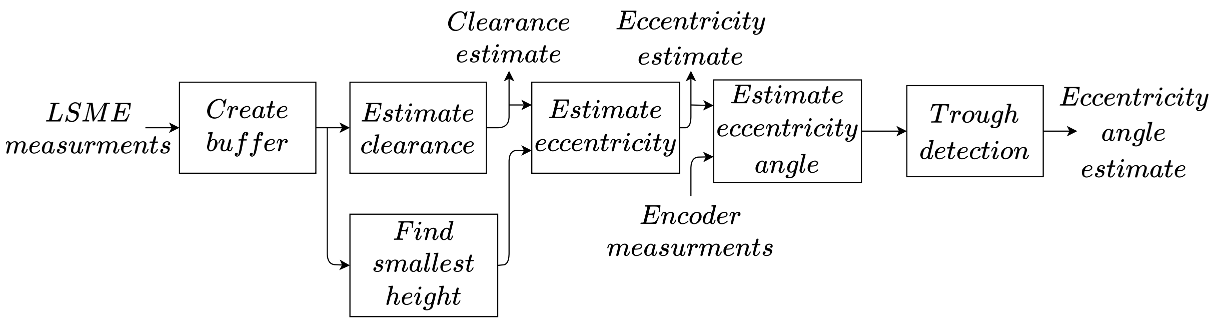

Figure 7.22: LSME state estimation algorithm.

The LSME state estimation algorithm uses a buffer with all the fluid film height estimates from a revolution of the journal, this means the buffers size changes with the rotational angular velocity and the pulse rate of the ultrasound transducer, as shown in equation (7.8).

$$Buffer\ size = \left\lceil \frac{2\,\pi}{\omega\, T_{pr}} \right\rceil \tag{7.8}$$

With a buffer containing all the height measurement from one revolution, the average height is equal to the radial clearance as seen in eq. (7.9), assuming the eccentricity and eccentricity angle does not vary significantly during a revolution.

$$h_{mean} = \frac{1}{2\pi} \int_0^{2\pi} C_r - \epsilon\, cos\,(\Omega - \theta)\ d\Omega = C_r \tag{7.9}$$

By applying this LSME state estimation algorithm on the data from the virtual experiment presented in Section 7.1.2 on page 50, the algorithm is capable of estimating the radial clearance as seen in Figure 7.23 on the facing page.

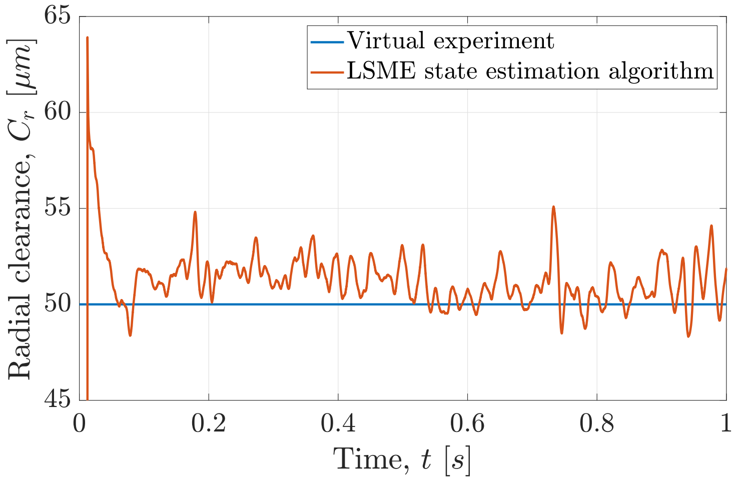

Figure 7.23: Clearance estimation of the LSME state estimation algorithm.

In Figure 7.23 the LSME state estimation algorithm is seen to have an initial transient period, before 0.1 s. This is due to the LSME having to determine the incident wave before it is capable of estimating the fluid film height, furthermore the LSME state estimation algorithm need to fill the buffer before it is able to estimate the radial clearance. When examining the radial clearance after 0.1 s, it is seen to be overestimated and the average clearance from 0.1 s to 1 s is found to be 51.2 μm. This overestimation is expected to be due to the LSME overestimating the height at the crest of the fluid film height measurements, this is seen in Figure 7.8 on page 58.

To estimate the eccentricity eq. (7.10) is used.

$$h = C_r - \epsilon \, cos\,(\Omega - \theta) \tag{7.10}$$

It is in eq. (7.10) seen that the smallest fluid film height occurs when the sine term equals one. This corresponds to the troughs of the fluid film height estimates and is given by the following equation.

$$\epsilon = C_r - h_{min} \tag{7.11}$$

It is from this equation seen that an estimate of the eccentricity is achieved, using the radial clearance estimate, and finding the lowest fluid film height during a revolution of the journal. Due to measurement noise the algorithm underestimates the eccentricity, as the lowest fluid film height is often an outlier. To mitigate this the average of the n lowest fluid film heights are used to suppress any outliers. It is found sufficient to use the 40 lowest height measurements to estimate the eccentricity.

It is in eq. (7.10) seen that the sine terms equals one when the measurement angle equals the eccentricity angle. Using this, an estimation of the eccentricity angle is found by using the mean encoder angle to the n lowest points used in the eccentricity estimation. However, this method possess a problem when the buffer is between two troughs, as seen in Figure 7.24a on the next page, the minimum heights might not be in the trough. This causes an error in the estimation of the eccentricity angle resulting in the spikes seen in Figure 7.24b on the following page.

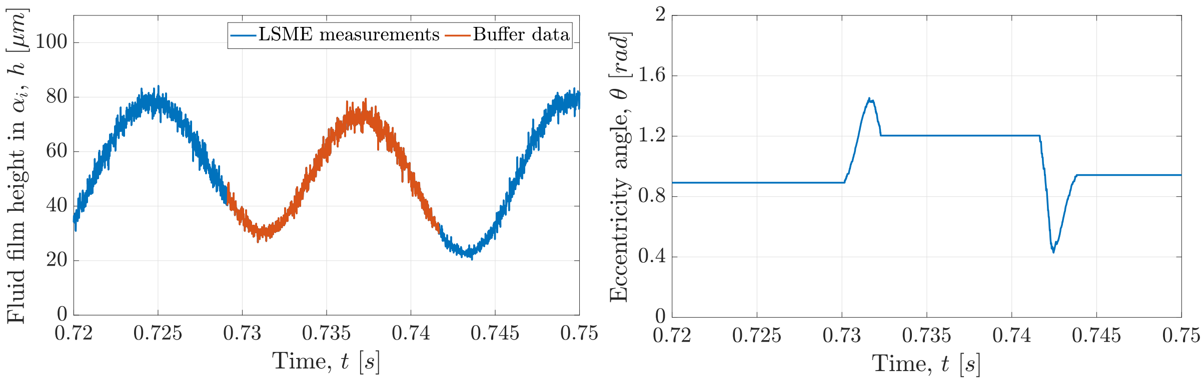

(a) Algorithm buffer **(b)** Eccentricity angle estimation

Figure 7.24: LSME state estimation algorithm without trough detection.

This phenomenon happens as the eccentricity is able to change during the time period logged in the buffer. As seen in Figure 7.24a the trough in the buffer is located close to 0.73 s, however the lowest height in the buffer is located at 0.74 s. This means the eccentricity angle estimate is based on points outside the trough. To mitigate this problem a trough detection algorithm is implemented to ensure the eccentricity angle is calculated at a trough. The trough detection works by checking whether the eccentricity angle changes at every iteration as the angle should only change when a new trough enters the buffer. This means if the eccentricity angle changes at every iteration the eccentricity angle is not found in a trough and the previous eccentricity angle is used instead. When the eccentricity angle then settles at a new value the eccentricity angle is updated by the trough detection. This results in the eccentricity angle only being updated once per revolution, this is also seen in Figure 7.25, showing both the eccentricity and eccentricity angle estimate.

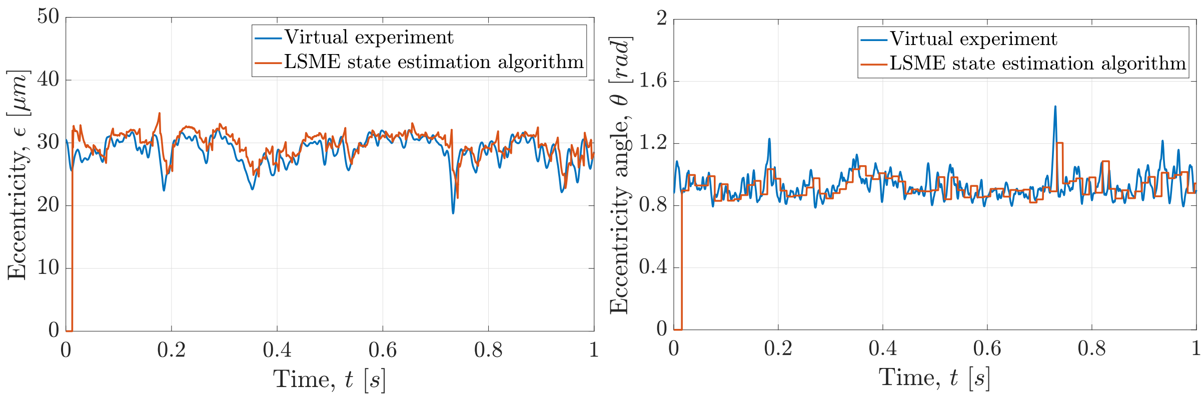

(a) Eccentricity **(b)** Eccentricity angle

Figure 7.25: State estimation using the LSME state estimation algorithm.

In Figure 7.25a the LSME state estimation algorithm is seen to track the eccentricity with a phase shift, this is to be expected as the algorithm used the height measurements in the troughs to estimate the eccentricity. The update rate of the troughs is determined by the angular velocity of the journal, creating a delay between every trough.

The phase shift is also evident in Figure 7.25b on the facing page. From the figure it seem as if the update rate of the eccentricity estimate is faster than that of the eccentricity angel. The reason for the seemingly faster update rate is that the eccentricity uses the radial clearance, as seen in eq. (7.10), which is updated at every iteration. However, the accuracy of the eccentricity and eccentricity angle estimates is reliant on information from the troughs, limiting the update rate.

If a faster update rate is necessary multiple transducers can be installed inside the journal to increase the number of troughs during a single revolution. From this it is seen that two transducers doubles the update rate of the LSME state estimation algorithm. However, the LSME state estimation algorithm's update rate is still dependent on the angular velocity of the journal.

7.5.1 State estimation algorithm using LSME, with varying clearance

The LSME state estimation algorithm is also tested on the data from the virtual experiment, where the radial clearance is changed during the simulation, presented in Section 7.4.2 on page 67. Figure 7.26 shows the radial clearance from the virtual experiments and the estimate from the LSME state estimation algorithm.

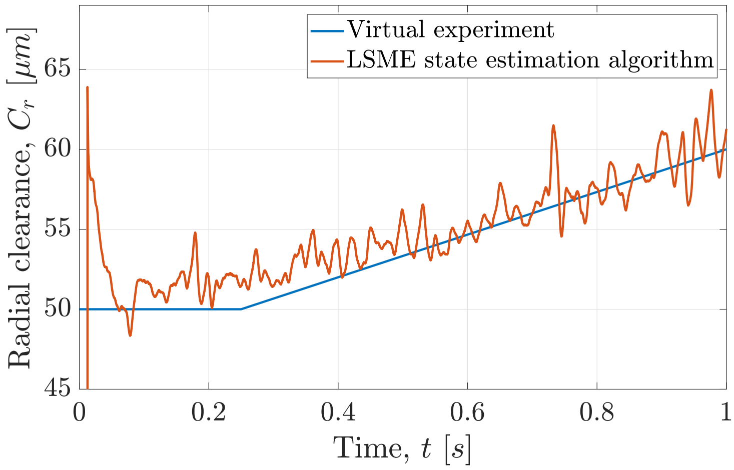

Figure 7.26: Radial clearance estimation with varying radial clearance.

In Figure 7.26 the LSME state estimation algorithm is seen to track the change in the radial clearance. The performance of the LSME state estimation algorithm at estimating the radial clearance is seen to be equal with the performance of the LSME state estimation algorithm with constant clearance.

The states estimate from the LSME state estimation algorithm is seen in Figure 7.27 on the following page.

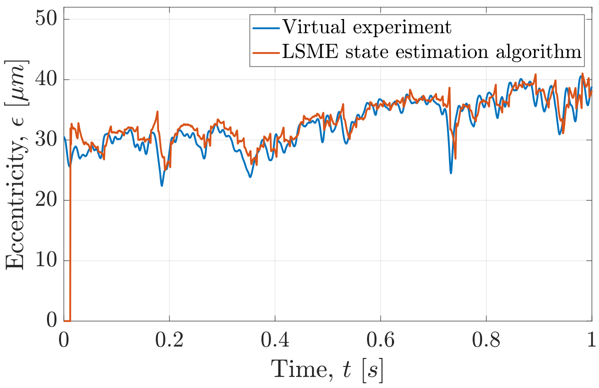

(a) Eccentricity

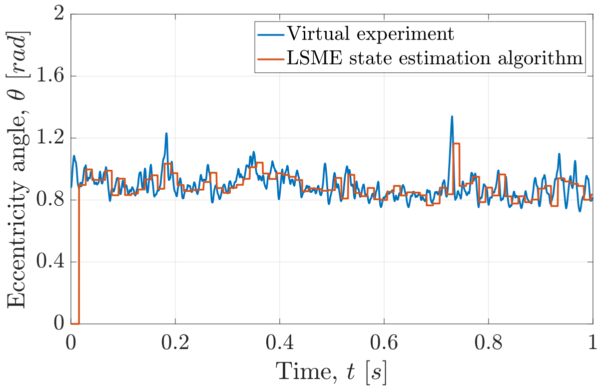

(b) Eccentricity angle

Figure 7.27: State estimation with varying clearance.

It is from Figure 7.27 seen that the LSME state estimation algorithm is able to track the states when the radial clearance is changing. It is notable that this LSME state estimation algorithm is based on the assumption that the change in the eccentricity and eccentricity angle is limited between each revolution, whereas the other algorithms thrives on the excitement.

8 | Robustness analysis

In Chapter 7 on page 49 the LSME and CCE algorithm are found to show great potential when the ultrasound transducers are placed within the journal. This is assessed to be due to the inherent high level of excitement in the fluid film height seen from the transducer. However, this level of excitement is both dependent on a large eccentricity and journal angular velocity. It is for this reason of interest to investigate the robustness toward the level of excitement. Another significant assumptions made in Chapter 7 on page 49 is that the TSO algorithms has a direct measurement of the external force on the system. This assumption is in real-life hard to fulfil, and the robustness toward uncertainties in the force input is for this reason investigated. Furthermore, the ultrasound reflection coefficients used in the test of the TSO are found close to the true value using the material models described in Chapter 4 on page 21 and Chapter 5 on page 31. It is for this reason of interest to investigate the algorithms robustness toward errors in these parameters. Lastly, in the derivation of the acoustic model in Chapter 5 on page 31 it is assumed that infinite scattering occurs in the fluid film layer. However due to practical issues when implementing the technology in real-life applications this might not be reasonable, and the validity of the assumption is for this reason investigated.

8.1 Analysis of the fluid film height excitement level

The analysis of the excitement level is based on analysing at which steady state eccentricities and journal angular velocity the LSME and CCE algorithms is able to converge. Furthermore, it is found in Chapter 7 on page 49 that if the eccentricity and angular velocity are large enough the algorithms are able to converge. It is for this reason of interest to investigate whether the algorithms continues to have accurate estimates, if the excitement level goes from large to small.

8.1.1 Eccentricity and journal angular velocity variation

The fluid film height seen from a ultrasound transducer is described by eq. (8.1).

$$h = C_r - \epsilon\, cos(\Omega - \theta) \qquad (8.1) \qquad\qquad \Omega = \omega\, t + \Omega_0 \qquad (8.2)$$

Where Ω is the measuring angle defined from the global coordinate frame. This angle is described by eq. (8.2) when the ultrasound transducer is placed inside the journal, assuming the journal rotates at a constant velocity. Where Ω_0 is the initial angle at which the transducer points when the measuring is initiated.

It is from eq. (8.1) seen that the time derivative of the fluid film height is given as the following equation.

$$\dot{h} = -\dot{\epsilon}\, cos(\omega\, t - \theta) + \epsilon\,(\omega - \dot{\theta})\, sin(\omega\, t - \theta) \qquad (8.3)$$

Assuming that the system is close to steady state, letting the time derivative of the states go to zero, the change in fluid film height, seen from the ultrasound transducer, is given as the following equation.

$$\dot{h}_{ss} = \epsilon \, \omega \, sin(\omega \, t - \theta) \tag{8.4}$$

It is from this equation seen that the magnitude of the change in fluid film height is determined from the eccentricity and journal angular velocity.

The investigation of the excitement level is based on eq. (8.1) for a journal angular velocity of 10 rad/s, 50 rad/s, 100 rad/s, and 500 rad/s. The eccentricity is varied for ten eccentricity ratios from 5 % to 95 %. The eccentricity angle is found from G.B. DuBois and F.W. Ocvirk steady state solution, eq. (2.3). The simulation time is equal to the time it takes five revolutions of the journal, and therefore the simulation time depends the journal angular velocity. The force input required for the CCE algorithms is found from the load number, eq. (2.2). The results from the test are shown in Figure 8.1.

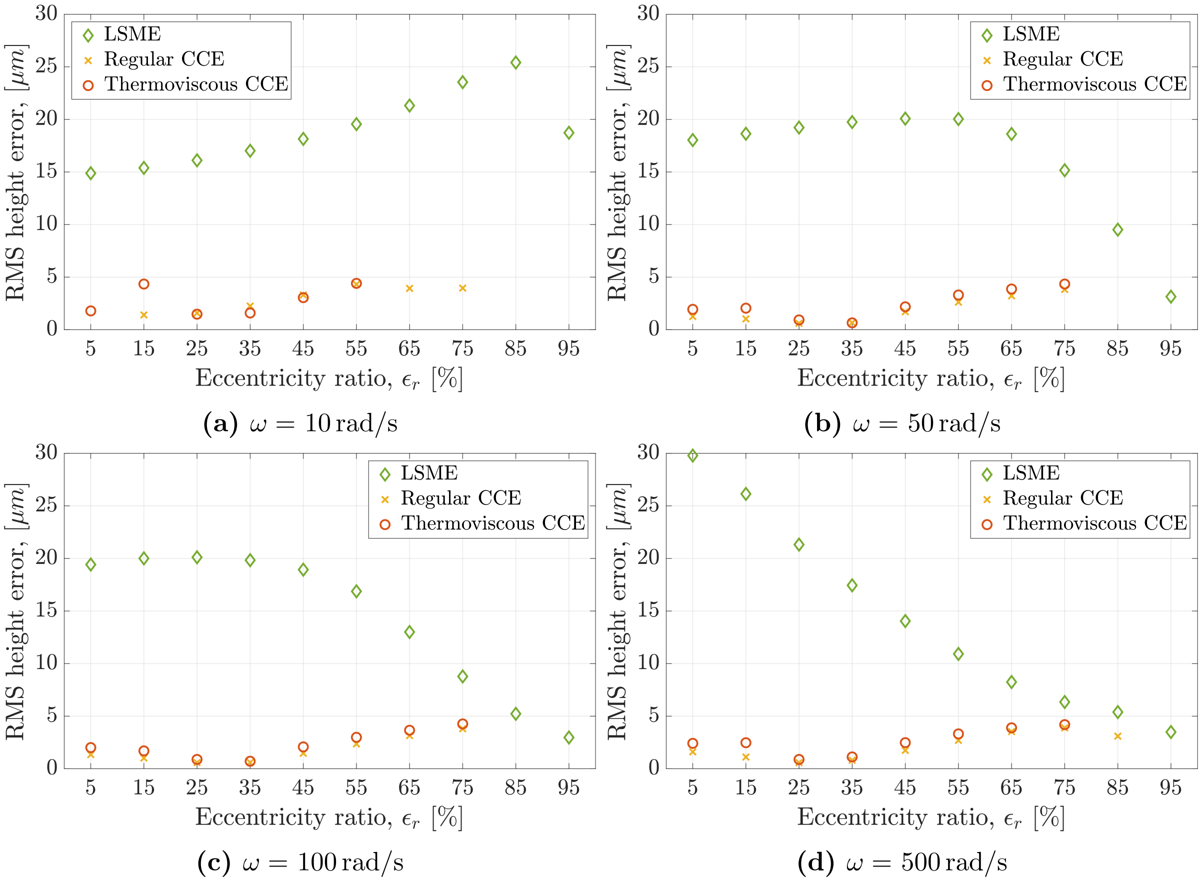

(a) $\omega = 10\,\mathrm{rad/s}$ **(b)** $\omega = 50\,\mathrm{rad/s}$

(c) $\omega = 100\,\mathrm{rad/s}$ **(d)** $\omega = 500\,\mathrm{rad/s}$

Figure 8.1: RMS error of the fluid film height estimate.

It is notable that some of the RMS values are not shown for the CCE algorithms, at small and large eccentricity ratios. The large eccentricity ratios are not included due to the largest system frequency becoming too large compared to the sampling frequency, resulting in unstable discretization of the system models, as discussed in Section 7.1.1 on page 49. The small eccentricity ratios that are excluded is because the oil whirl phenomenon occurs in the system models used for the CCE algorithms. It is here notable that for this reason some of the small eccentricity ratios might not be possible to achieve in real life systems.

It is from Figure 8.1 on the facing page seen that the CCE algorithms have similar performances and that they in general have less error regardless of excitement level compared to the LSME algorithm.

It is from Figure 8.1b on the preceding page, Figure 8.1c on the facing page, Figure 8.1d on the preceding page seen that the LSME algorithm tends to deviate less as the eccentricity ratio increases. It is from these figures also seen that the eccentricity ratio at which the deviation start to decrease is dependent on the journal angular velocity. This tendency is described by eq. (8.4) where the product of the angular journal frequency and the eccentricity determines the fluid film height excitement level.

Figure 8.1a on the facing page shows an opposite trend for the LSME algorithm compared to the other figures. It is here seen that the deviation starts to increase as the eccentricity ratio increases, except for a eccentricity ratio of 95 %. This is due to the inconsistency of using RMS at the determining criteria. Figure 8.2 shows a selection of the simulations.

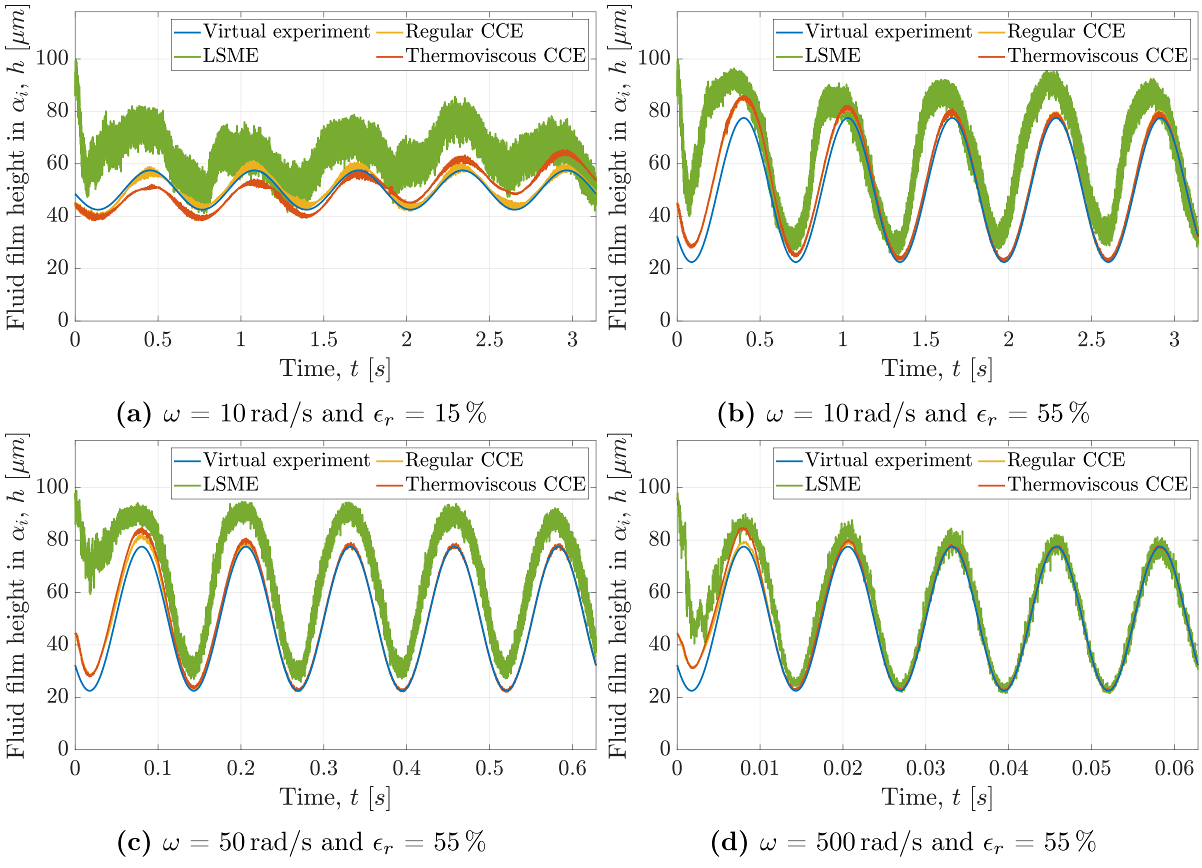

(a) $\omega = 10\,\mathrm{rad/s}$ and $\epsilon_r = 15\,\%$

(b) $\omega = 10\,\mathrm{rad/s}$ and $\epsilon_r = 55\,\%$

(c) $\omega = 50\,\mathrm{rad/s}$ and $\epsilon_r = 55\,\%$

(d) $\omega = 500\,\mathrm{rad/s}$ and $\epsilon_r = 55\,\%$

Figure 8.2: Example of fluid film height estimates at different excitement levels.

It is from Figure 8.1a on the facing page seen that for a journal angular velocity of 10 rad/s the RMS error of the LSME algorithm is smaller at a eccentricity ratio of 15 % compared to eccentricity ratio of 55 %. It is however from Figure 8.2a and Figure 8.2b seen that the algorithm arguably is better at estimating the fluid film height for a eccentricity ratio of 55 %. The RMS error is from Figure 8.2a seen to be small, not because the estimation follows the true fluid film height but simply because the large noise levels puts the estimate in the vicinity of the true fluid film height.

It is from Figure 8.2a on the preceding page seen that for low excitement levels the CCE algorithms still estimate the fluid film height to a satisfying degree. It is from the figure seen that the Thermovicous CCE is slightly worse than the Regular CCE. This might be due to the lack of system dynamics resulting in difficulties for the Themoviscous CCE to estimate the boundary viscosity, where as the Regular CCE is given the correct parameter.

8.1.2 Analysis of force step

In order to test whether the LSME and CCE algorithms are capable of estimating the fluid film height when the excitement level goes from large to small, a virtual experiment is conducted where a step in the external force occurs. This step in the external force is seen in Figure 8.3. It is notable that this experiment is conducted for a journal angular velocity of 100 rad/s.

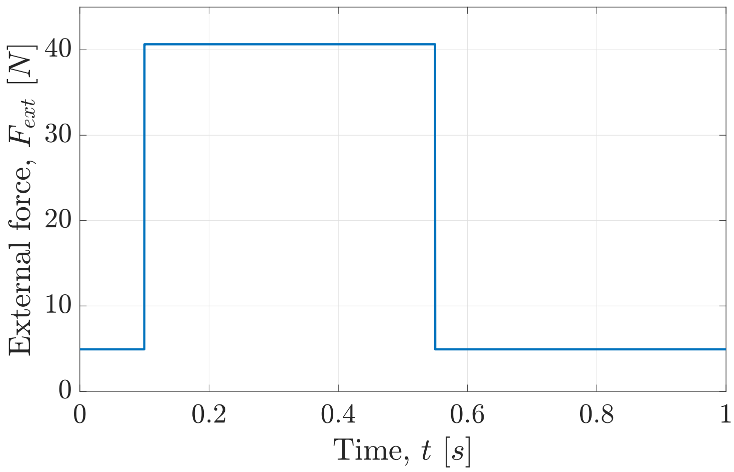

Figure 8.3: Force step input.

The force step shown in Figure 8.3 makes it such that the eccentricity ratio varies from around 20 % to 60 %. It is notable that due to a journal angular velocity of 100 rad/s there is less viscous dissipation in this experiment, compared to those at 500 rad/s. This also means that the average temperature of the fluid film is 295.4 K, but the CCE and LSME algorithms still use the baseline values evaluated at 313.2 K.

The fluid film height corresponding to this force step is seen in Figure 8.4.

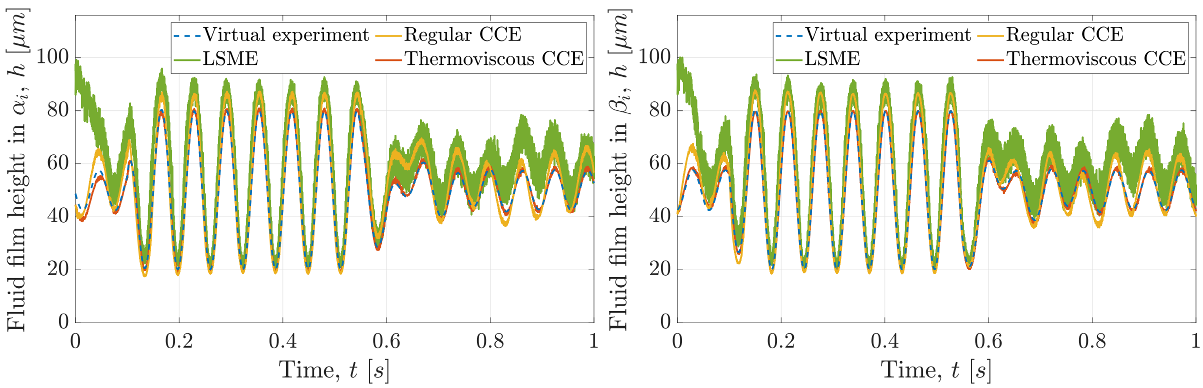

(a) α_i-direction **(b)** β_i-direction

Figure 8.4: Fluid film height with force step inputs.

It is from Figure 8.4 on the facing page seen that the Thermoviscous CCE has a short transient period but manages to estimate the fluid film height closely before the excitement level increases. It is from the figure seen that Regular CCE has generally worse tracking capabilities compared to the Thermoviscous CCE algorithm. It is in the figure seen that the Regular CCE and LSME has similar tracking capabilities in the region with large excitement levels, but in the region with small excitement level the Regular CCE is more accurate. The LSME algorithm is seen to track the fluid film height to a satisfying degree when the external force is large, but does not keep the tracking capabilities when the force is decreased. This effect might be mitigated in the tuning of the LSME algorithm. Here it is possible to reduce the rate at which the incident wave estimate changes after the initial transient period. However, this might also mitigate the effect at which the algorithm is able to track changes in the incident wave, and in the long run negatively affect the fluid film height estimates.

8.2 Analysis of robustness toward error in the reflection coefficients

An uncertainty present in all the proposed TSOs and LSME algorithms is that the reflection coefficients is estimated to a satisfying degree. It is for this reason of interest to investigate the performance of the proposed algorithms when the reflection coefficient are modelled incorrectly. This analysis assumes that both the bushing and journal are made of the same material. Furthermore, the analysis varies the acoustic impedance of the fluid film layer and the journal bearing separately. Each parameter is varied from 70 % to 130 % of its original value, and the resulting RMS percent deviation in the fluid film height compared to the virtual experiment is seen in Figure 8.5.

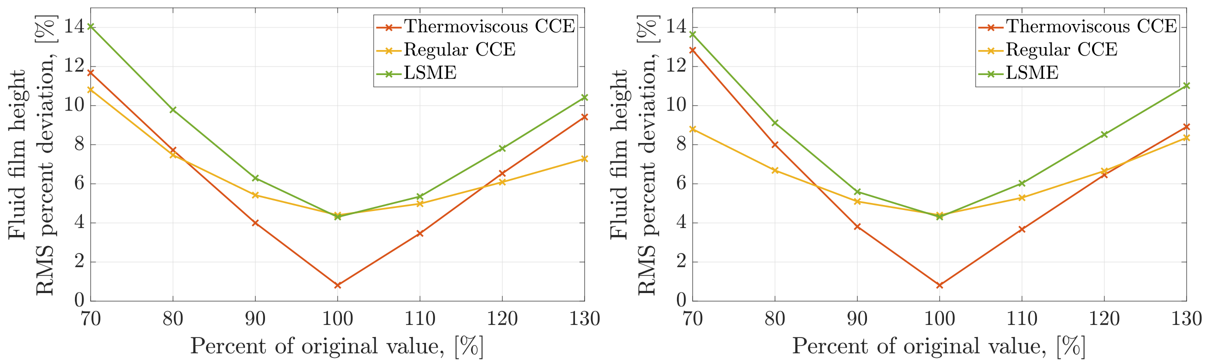

(a) Variance in z_a and z_c **(b)** Variance in z_b

Figure 8.5: Variance in the specific acoustic impedance.

Figure 8.5 shows that the LSME algorithm generally has larger deviations compared to the CCE algorithms. A notable tendency seen in figure is that the Regular CCE has smaller deviation for large errors in the acoustic impedances compared to the Thermoviscous CCE. This might be due to the worsened ultrasound measurements affecting the boundary viscosity estimate, whereas the Regular CCE uses the correct viscosity found from the virtual experiments. This might for this reason be an unfair comparison, due to the uncertainty in determining the viscosity for the Regular CCE in real-life applications. Another notable tendency seen from the figure is, that it is generally worse to underestimate the acoustic impedances, compared to overestimating.

8.3 Analysis of robustness toward error in force estimate

A major assumption for the TSO algorithms tested in Chapter 7 on page 49 is that the TSOs receives the exact external force applied to the journal. However, in many applications the external force might be difficult to determine. It is for this reason of interest to investigate the robustness of the TSO strategies with limited knowledge of the external force. This analysis is based on the Thermoviscous CCE algorithm, shown in Chapter 7 on page 49 to have the most accurate state estimates. In real-life applications it might be difficult to know the exact external force, it is however believed that it is still possible to give an estimate of the magnitude and direction of the force.

The virtual experiment data used for this test is the same as that presented in Chapter 7 on page 49, where the viscosity is varied. This force input is applied in the α-direction and is modelled using a bandpass filter on a Gaussian white noise signal. The force is seen to have a mean value of approximately 63 N and varies from around 20 N to 90 N.

The force input used in the Thermoviscous CCE during this test is a constant force input. In the analysis the magnitude of the force is varied from 50 % to 150 % of the mean force used in the virtual experiment. Furthermore, the angle of the force is varied from $-45°$ to $45°$ of the force angle used in the virtual experiment.

Figure 8.6 shows examples of the fluid film height and corresponding estimate when the Thermoviscous CCE receives the altered force inputs.

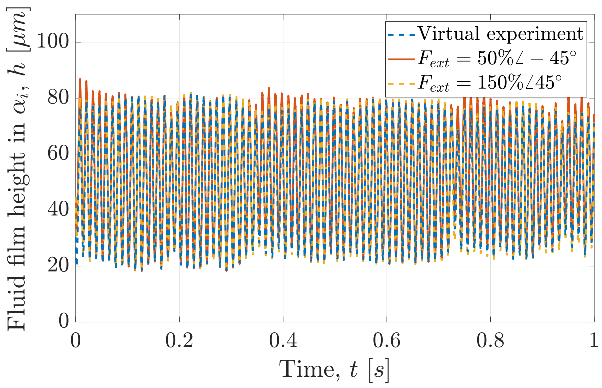

(a) Virtual experiment compared to the two force inputs

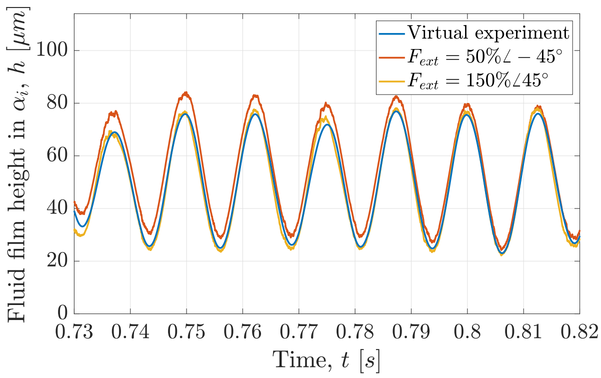

(b) Zoom of the virtual experiment compared to the two force inputs

Figure 8.6: Fluid film height estimate using the altered force input.

Figure 8.6 shows two extreme cases where the estimate of the force angle and magnitude are far from the values used for the virtual experiments. The figure shows that there are certain periods where the fluid film height estimate is seen to have large deviations, such as from 0.73 s to 0.82 s. It is in this period seen that the deviation of the largest fluid film height is greater than that at the smallest fluid film height. This might be due to the sensitivity of the CCE algorithm as described in Section 7.3.4 on page 61. It is from the figure seen that even in these extreme scenarios the fluid film height is estimated to a satisfying degree for most of the simulation.

Figure 8.7 shows the percent RMS deviation in the fluid film height estimate.

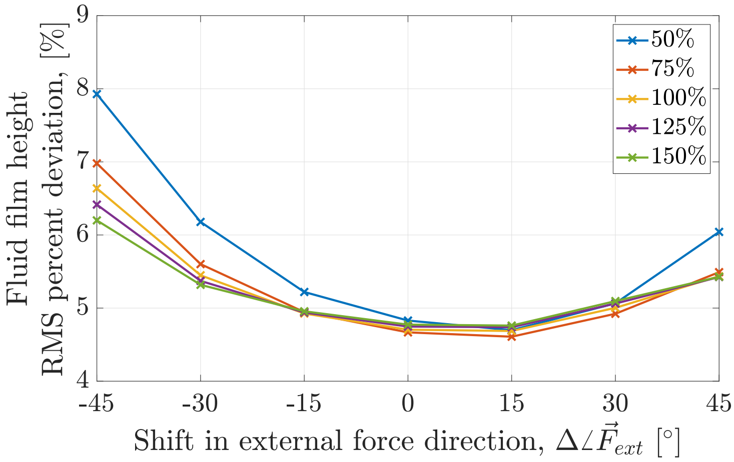

Figure 8.7: Percent RMS deviation in the fluid film height.

Figure 8.7 shows that except for the 50 % estimate of the external force, the magnitude estimate does not significantly affect the Thermovisous CCE's ability to estimate the fluid film height. It is from the figure seen that the angle estimate of the external force has a larger influence on the the ability to estimate the fluid film height. The different force inputs tested in this analysis is seen to worsen the percent RMS fluid film height estimate less than 3.5 % points. This indicates that with regards to the fluid film height estimate the algorithm seems robust.

Figure 8.8 on the next page shows the boundary viscosity estimates from the Thermoviscous CCE algorithm, at the different force inputs.

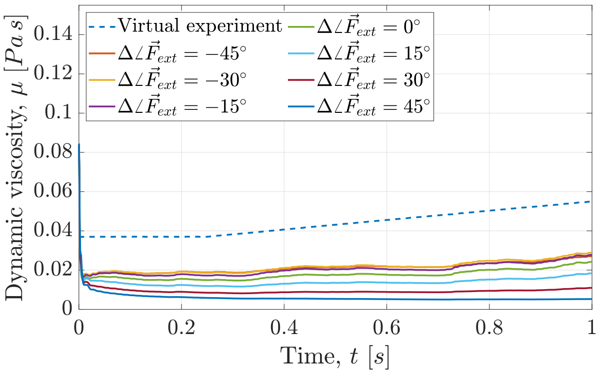

(a) 50 % of the mean force

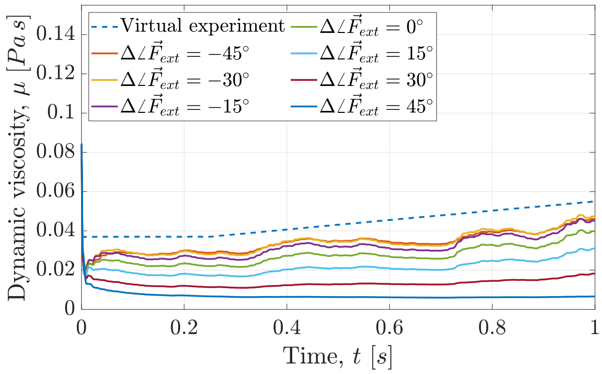

(b) 75 %of the mean force

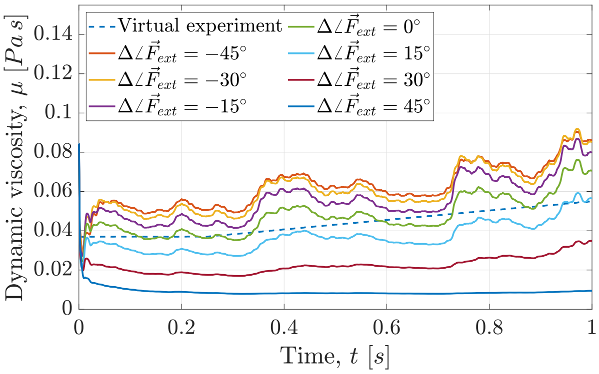

(c) 125 % of the mean force

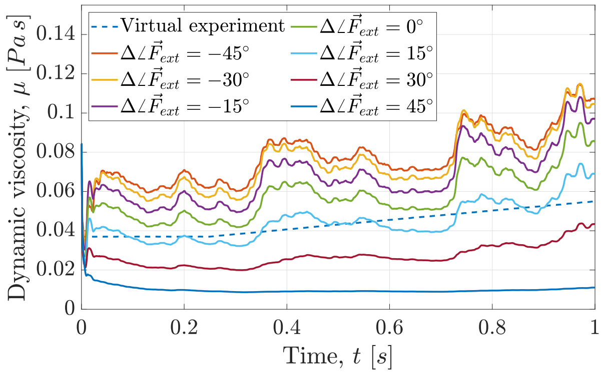

(d) 150 % of the mean force

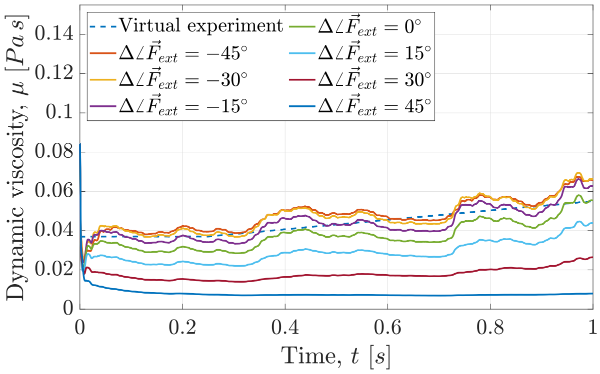

(e) 100 % of the mean force

Figure 8.8: Viscosity estimate with altered force inputs.

It is from Figure 8.8 seen that the viscosity is less robust towards errors in the force estimate, compared to the fluid film height. This is because a change in boundary viscosity is not able to compensate for the differences in the dynamics, similar to the virtual experiment where the radial clearance is varied, Section 7.4.2 on page 67. It is from Figure 8.8 seen that for most of the force estimates it is still possible to see the upwards trend of the viscosity in the estimates. It is also seen that large force magnitude estimates causes large fluctuation in the viscosity estimate.

Figure 8.8 also shows that the viscosity estimates seems to worsen when the force angle estimate is positive shifted, compared to those negative shifted. This might be due to the relation between the attitude angle and eccentricity ratio, eq. (2.3), described by G.B. DuBois and F.W. Ocvirk, shown in Figure 8.9 on the facing page.

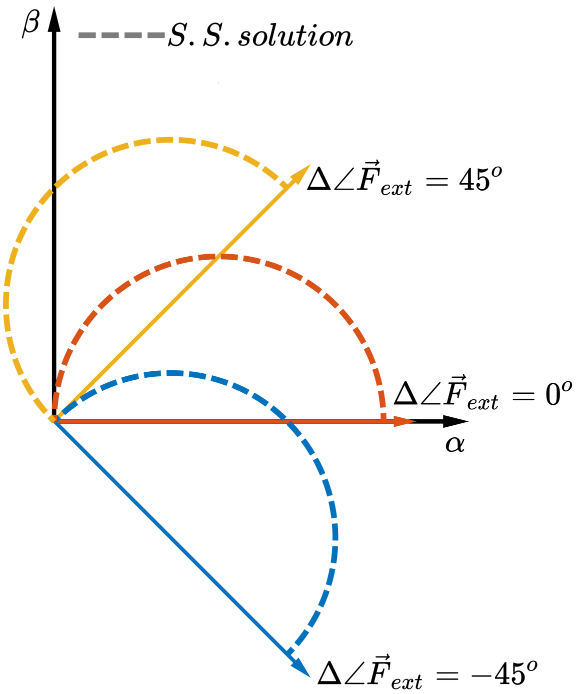

Figure 8.9: S.S solution presented by G.B. DuBois and F.W. Ocvirk.

It is from Figure 8.9 seen that for a positive journal angular velocity, the eccentricity angle moves counter clockwise from the force direction applied, toward the S.S solution. This means that for the negative shifted forces the model estimate and the correction from the measurement agree of polarity of the time derivative of the states. Whereas, for the positive shifted forces, the model and correction from the measurements disagree, this means that the EKF algorithm has to compensate more, compared to the negative shifted forces.

It is from this analysis seen that it is possible to estimate both fluid film height and boundary viscosity even though the external force applied to the journal is not directly known. The robustness towards this is a great concern from the previous study [12]. The results from this analysis is for this reason a great indication of the potential of the TSO algorithms.

8.4 Cluster study

In the derivation of the acoustic model, Chapter 5 on page 31, it is assumed that the scattering of the incident wave can be represented as an infinite sum. However, in practice the time in which the reflection wave is able to be measured is limited. This measuring time is among other limited by the pulse rate of the transducer. However, the most dominant limitation is assessed to be due to the time it takes the reflection wave to travel from the fluid film layer boundary to the boundary on which the ultrasound transducer is placed and back, referred to as clusters. This is illustrated in Figure 8.10 on the next page.

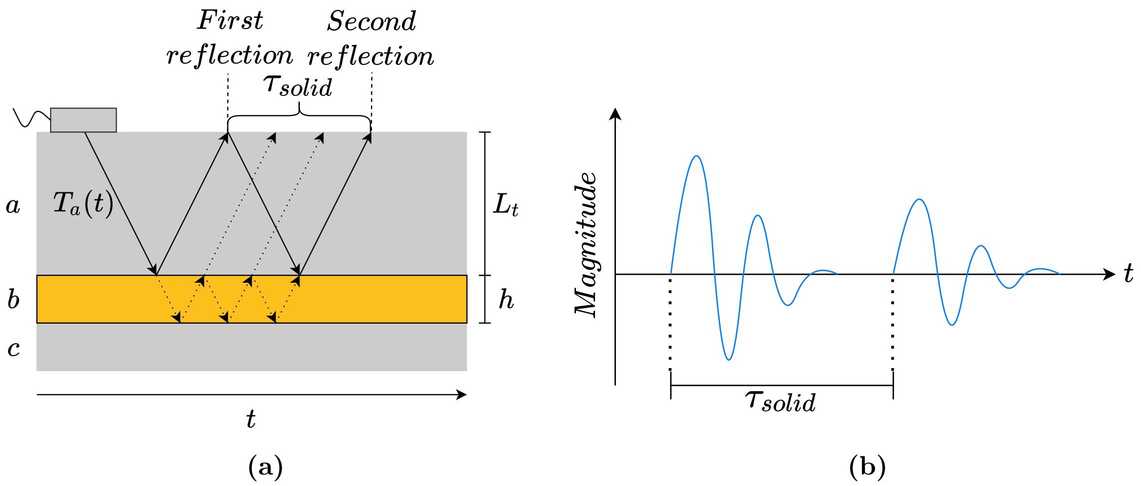

Figure 8.10: Cluster illustration.

Figure 8.10 shows how the second reflection wave interferes with the amount of time it is possible to measure the first reflection wave. It is believed that if the energy of the signal within the fluid layer is significantly damped before the disturbance, from the second reflection, occurs the assumption of infinite scattering is still valid.

It is in Chapter 5 on page 31 seen that the time it takes the ultrasound wave to travel from boundary ab to bc is given as the equation below.

$$\tau_{fluid} = \frac{h}{c_b} \tag{8.5}$$

It is from figure 8.10a, seen that the critical time before the reflections in the fluid layer gets disturbed is given as the equation below.

$$\tau_{solid} = \frac{2L_t}{c_a} \tag{8.6}$$

Where L_t is the distance from the ultrasound transducer to boundary ab. It is from this seen that the number of times the ultrasound wave in the fluid film layer scatters before the critical time is given as.

$$n_{scat} = \frac{\tau_{solid}}{\tau_{fluid}} = \frac{2\,L_t\,c_b}{h\,c_a} \tag{8.7}$$

Since it is assumed that material a and c are the same, the amount of energy that is kept in the signal after each scattering is given by the reflection coefficient, R_{ab}. It is here seen that percentage energy in the signal as a function of times scattered is given by the following equation.

$$P_e = 100\,|R_{ab}|^{n_{scat}} \tag{8.8}$$

Figure 8.11 on the next page shows the percentage of energy still in the signal, when the second wave occurs, as a function of fluid film height when the transducer is placed 2.5 mm, 5 mm, 10 mm and 20 mm away from ab boundary.

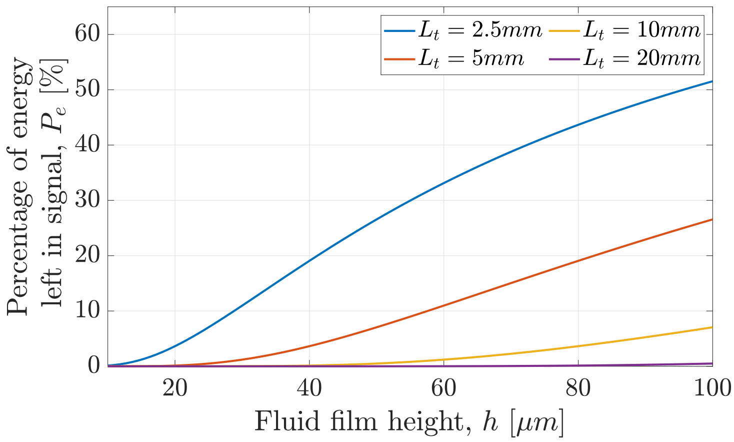

Figure 8.11: Percentage of energy left in the signal as a function of fluid film height.

It is from Figure 8.11 seen that the amount of energy left in the signal when the disturbance occurs is largely dependent on both the fluid film height and the distance from the transducer to the ab boundary. It is from the figure seen that for a fluid film height of 100 µm and a transducer placement of 2.5 mm, 50 % of the energy is left in the signal and if this is the case the assumption of infinite scattering might not be valid. However, it is also seen from the figure that if the journal is placed longer than 10 mm away from the boundary there is only around 8 % energy left, for the largest fluid film heights investigated. This indicates that in this region the assumption of infinite scattering might still be valid.

It is from this analysis found that if it is the pulse rate that is the limiting factor, there is only 0.0062 % energy left in the signal, at a fluid film height of 100 µm and pulse rate of 80 kHz. It is from this seen that the pulse rate of the transducer has a negligible effect compared to the clusters.

It is from this analysis seen that the length at which the transducer is placed from the ab boundary largely affects the amount of energy left in the signal before the new cluster occurs. It is from this believed that depending on the type of application, an investigation into another acoustic model might be beneficial. This might be the investigation into an acoustic system representation that considers more than the two boundaries of the fluid film, but also the boundary on which the ultrasound transducer is placed.

9 | Discussion

9.1 Force estimation algorithms

In Section 8.3 on page 80 it is seen that it is possible to estimate both fluid film height and boundary viscosity if the Thermoviscous CCE strategy is provided with an estimate of the force magnitude and direction. This is believed achievable from the LSME algorithm. In Section 7.5 on page 70 it is seen that it is possible to derive algorithms that estimate the mechanical system states and radial clearance based on the fluid film height estimates from the LSME algorithm. These state estimates makes it possible to estimate the attitude angle, using the following equation.

$$\xi = tan^{-1}\left(\frac{\pi\sqrt{1-\left(\frac{\epsilon}{C_r}\right)^2}}{4\left(\frac{\epsilon}{C_r}\right)}\right) = \theta - \angle\vec{F}_{ext} \tag{9.1}$$

It is from this equation seen that by estimating the eccentricity and radial clearance it is possible to determine the attitude angle. With estimates of the attitude angle and the eccentricity angle it is then possible to determine the angle of attack from the external force, that is usable in the TSO algorithms. This algorithm does assume that the steady state relation between eccentricity ratio and attitude angle is usable in a dynamic environment, which adds a level of uncertainty to the algorithm. Furthermore, the developed algorithm for estimating the mechanical system states using LSME is based on placing the ultrasound transducer within the journal, and the update rate of the state estimates heron depends on the angular velocity of the journal.

It is also possible to estimate the magnitude of the external force from the load number, the following equation.

$$L_N = 4\,\pi\,\frac{|\vec{F}_{ext}|\,C_r^2}{\mu\,\omega\,L^3\,R} = \frac{\pi\,\frac{\epsilon}{C_r}\sqrt{\pi^2\left(1-\left(\frac{\epsilon}{C_r}\right)^2\right)+16\,\left(\frac{\epsilon}{C_r}\right)^2}}{\left(1-\left(\frac{\epsilon}{C_r}\right)^2\right)^2} \tag{9.2}$$

It is here seen that an estimate of the eccentricity ratio allows for an estimate of the load number. If the fluid film length and inner radius of the bushing is known together with measurement of the angular velocity of the journal, the only parameter needed for force estimation is the dynamic viscosity of the fluid. A possible estimate of the dynamic viscosity is measuring the temperature close to the fluid layer and relating this to dynamic viscosity with a viscosity model such as the Vogel model. This gives an estimate of the magnitude of the external force for use in the TSO algorithms.

The robustness of the TSO algorithms might be further increased with knowledge of the frequency span of the external force. If a data set of the expected external force is available it is possible to derive a white noise driven disturbance model for use in the EKF algorithm, used in the TSOs. The EKF algorithm assumes model disturbances to be Gaussian white noise and the white noise disturbance model explains the variation from the mean force as a white noise input to the disturbance model. With the system model expanded by the disturbance model, the EKF algorithm is more robust towards changes to the force input, and might for this reason increase the robustness of the TSO algorithms.

9.2 Radial clearance estimates

It is in Section 7.4.2 on page 67 seen that the boundary viscosity estimate from the Thermoviscous CCE algorithm varies when other system parameters are varied, such as the radial clearance. This makes it difficult to determine wear on the oil, since wear on other system parameters affects this estimate. It is from the section however seen that radial clearance affect the system dynamics in a way that is not fully compensated for from adjusting the viscosity estimate. This means that it might be possible to add the radial clearance as a slow varying system state to the TSO, similar to the boundary viscosity. This strategy might be further improved from adding the clearance estimate, from the LSME state estimation algorithm, as an input to the Thermoviscous CCE.

9.3 Number and placement of ultrasound transducers

It is in this study proposed placing two ultrasound transducers 90° apart within the journal. However this might not be the optimal placement nor amount of ultrasound transducers for fluid film height estimation, when they are placed inside the journal. It is in Section 7.3 on page 54 seen that the CCE and LSME algorithms have more accurate fluid film height estimates when the fluid film height is small. It might be more beneficial to place the ultrasound transducers such that the longest time between each sensor passes the region of least fluid film height is minimised, when two ultrasound transducers or more is to be used. This is especially notable for the proposed LSME state estimation algorithm, in order to increase the update frequency. The update frequency can also be increased by adding more than two sensors to the system. It is seen that the LSME algorithm that only uses one ultrasound transducer is able to estimate the fluid film height. This also indicates that the proposed TSO strategies can work with only one ultrasound transducer. This might be of interest to investigate in application where there is not enough space within the journal for two ultrasound transducer or if it is desired to lower the cost of the application.

9.4 Data extraction from the transducer

It is in Section 8.1 on page 75 seen that placing the ultrasound transducer inside the journal increases the fluid film excitement level even without system dynamics. It is for this reason believed that this way of placing the ultrasound transducers are superior with regards to the robustness of the algorithms. However, this way of placing the transducers might be more complicated or implausible depending on the application of interest, compared to placing them on the bushing. A primary concern from this method is the data extraction from the transducers. In the study Beamish et al. [1] this is achieved by using multi-channel slip rings. However, it might be of interest to investigate wireless ultrasound transducers. This study would both entail wireless data transfer and power transfer, or ways of generating power within the journal. Furthermore, since placing the transducer inside the journal might not be appropriate for some applications, it is still of interest to investigate the applicability of TSOs when the transducers is placed on the bushing.

9.5 Multi-frequency auto-calibration algorithms

It is in this study found that the LSME algorithm has a generally worse accuracy and robustness compared to the proposed CCE algorithms. However, the LSME algorithm is significantly less complex and only requires ultrasound measurement, compared to the system inputs required for the TSO algorithms. Standalone auto-calibration algorithms is for this reason still of interest to investigate. A general concern with the LSME algorithm is that it only consider the frequency response of the reflection wave at a single frequency. An interesting topic is for this reason multi-frequency auto-calibration algorithms. It is in this study found that the PDE algorithm that uses evaluation of multiple frequencies is not as sensitive to large fluid film heights, compared to the LSME and CCE algorithms, and this is an indication of the potential of multi-frequency algorithms. Furthermore the evaluation strategies for TSOs might also use any developed multi-frequency algorithms, to have the benefits from both methods.

9.5.1 Excitement study

When investigating standalone auto-calibration algorithms it might be of interest to do a study of the excitement level required for the algorithms to properly work. In Section 8.1 on page 75 it is seen that when placing the ultrasound transducer inside the journal, the fluid film height is excited even without changes to the eccentricity and eccentricity angle. It is in the section described how the magnitude of this excitement is the product of the eccentricity and journal angular velocity. It is from this proposed that if a excitement study is to be made this product can become a measure of the level of excitement.

$$E = \omega \, \epsilon \tag{9.3}$$

$$E_{norm} = \omega \, \epsilon_r \tag{9.4}$$

It is seen in Section 8.1 on page 75 that using the RMS error from the fluid film height estimate is an inconsistent measure of the tracking capabilities of the algorithms. Less inconsistent measures might be found, these could be measures based on a frequency analysis, auto-correlation, or others of the residual between estimate and true height. Measures based on frequency analysis might also be able to consider noise on the estimate.

9.6 Combining TSO evaluation strategies

It is in Section 7.3 on page 54 seen that the Regular PDE algorithm is generally less robust and accurate than the CCE algorithm. It is however seen that the PDE algorithm does not have the same problem with sensitivity at large fluid film heights. It might for this reason be of interest to combine the two evaluation strategies in a single TSO. This has the potential of the robustness of the CCE algorithm but less sensitive estimates at large fluid film heights.

9.7 Tuning

All the results presented in this study is highly dependent on the tuning of the algorithms. This tuning process is highly complicated due to the large amount of tuning parameters and the tuning parameters found might be biased toward the experiments used for the tuning. It is for this reason of interest to investigate methods for simplifying the tuning process. Furthermore, any algorithms neglected can have potential performance undiscovered in this study.

9.7.1 Expansion of virtual experiments

In a real-life application, the tuning of the parameters is even more complicated since it is not possible to compare the estimate with the true variable. It is therefore still of great interest to develop more advanced virtual experiments such that the data from these can be used as the basis for comparison when tuning. The expansion of the virtual experiments could be considering effects such as air cavitation in the fluid film, thermal expansion, and deflection of the solid components.

The pressure forces is in the virtual experiments found from only integrating the area of the journal with positive pressure forces. This contradicts the assumption of mass conservation within the system, because of the abrupt pressure changes. An algorithm for maintaining the assumption of mass conservation is the Elrod and Adams algorithm. The Elrod and Adams algorithm is found to be a good compromise between an accurate physics representation of the system and computational time. [20] This algorithm could be a good inclusion into the virtual experiment. This is not considered in this report due to solver difficulties when also considering thermoviscous effects.

It is in the derivation of the analytical thermoviscous pressure equation found that the heat transfer in the fluid film due to conduction is dominant in the cross film direction, Section 3.3.2 on page 14. However, due to computational difficulties with the numerical solvers used for the virtual experiments in this study, this had to be excluded from the virtual experiment using the thermally thin approximation of the fluid. Since it is found that the heat transfer in the cross film direction might not be negligible it is still of interest to include this in the virtual experiments.

It is in this study found that the thermodynamics within the solids have much slower transients than the mechanical states of the system. However, these dynamics are still simulated using a time dependent solver. Due to the slow nature of the thermodynamics of the solids it might be beneficial to calculate these using a S.S. solver. This would significantly reduce the computational time of the simulation. Furthermore, when excluding the thermodynamics of the solids from the time dependent solver, it might be possible to add some of the previously mentioned physics to the virtual experiment. Another benefit from this simulation strategy, is that it might be possible to simulate more than 1 s of dynamics, and from this see a greater influence of the thermodynamics in the fluids effect on the system. It is here notable, that if the simulation time becomes significantly large, the assumption of slow varying thermodynamics in the solids might not be valid.

9.8 Critical assumptions

In the derivation of both the analytical hydrodynamic models and virtual experiments, several assumptions are made, that might be critical to the performance of the proposed algorithms and for this reason need further investigation.

Firstly, the pressure at both ends of the fluid film are assumed zero. This assumption might not be valid for hydraulic applications, where the fluid film is connected to a load bearing flow, such as power displacement units. An investigation into whether this has a significant effect on the hydrodynamics is for this reason needed. Furthermore, if it is found to have a significant effect, a way of introducing it into the analytical journal bearing models is needed. It is in the derivation of the analytical pressure equations, Chapter 3 on page 7, seen that this might not be trivial.

Secondly it is assumed that the fluid film height does no vary in the longitudinal direction of the bearing. This might not be true both when considering deflection of the journal and also asymmetric loading. The proposed TSO algorithms are based on journal bearings where the short bearing approximation is applicable, and the variation of fluid film height in the longitudinal direction might be negligible for this reason. However, if this is not found to be the case, or if the technology is to be applied to other types of bearings, it is of great interest to expand upon the analytical models to include this.

9.9 Experimental validation

Compared to the previous study of the same authors [12] the virtual experiments are more advanced. However, it is still believed that in order to fully explore the applicability of the proposed TSO algorithms, it is required to experimentally validate the methods in a laboratory environment where it is possible to compare the TSO estimates with sensor measurements. The sensor measurements used for comparison could be optical, mechanical or electric resistance and capacitance methods, found to work in laboratory environments but too invasive for use in real-life applications. [8] [16]

10 Conclusion

In this study a virtual experimental setup is developed. This setup includes thermo- and piezoviscous effects, thermo- and hydrodynamics both in the fluid and solids, and does not use the short bearing approximation. The virtual experiment does use the thermally thin approximation due to computational difficulties, which means the temperature is constant with regards to the cross film direction, even though it is assessed that conduction in this direction is dominant. However, it is believed that the virtual experimental setup represents real-life applications to a greater extend than the developed analytical hydrodynamic models. The data from the virtual experiments are for this reason used for the validation of the developed tribological state observer strategies, and from this the following results are found.

This study showed that tribological state observer strategies that include ultrasound reflectometry are achievable either by evaluating the complex components of the frequency response of the reflection wave at a single frequency, or by evaluating the phase derivative at multiple frequencies. In this study the complex component evaluation criterion is shown to be superior to the phase derivative evaluation criterion. However, the result might be biased by the complicated tuning process of the strategies, and it is still believed that the phase derivative criterion can be used in combination with the complex component criterion. In this study it is found that tribological state observes with the complex component evaluation criterion has superior robustness and accuracy compared to the proposed standalone auto-calibration algorithm, that only evaluates the frequency response of the reflection wave at a single frequency.

This study also shows that both standalone ultrasound reflectometry and tribological state observer strategies have increased robustness when the ultrasound transducers are placed inside the journal. This is assessed to be due to the increased excitement level of the fluid film height seen from the ultrasound transducer. Furthermore, it is seen that when placing the ultrasound transducer inside the journal it is possible to estimate the eccentricity, eccentricity angle, and radial clearance simply from the fluid film height estimation of the standalone ultrasound reflectometry method.

It is in this study found that including thermoviscous effects into the proposed tribological state observer not only increased robustness and accuracy of the fluid film height estimates, it also allowed for estimating the dynamic viscosity. This estimate is able to detect changes to the dynamic viscosity but also varies if other system parameters are changed, such as the radial clearance. It is from the study found that when including thermoviscous effects in the tribological state observers, it is possible to estimate the fluid film height and dynamic viscosity even though limited information of the external force applied to the system is known.

It is from this study believed that in order to fully explore the applicability of the proposed tribological state observer strategies, experimental validation of the methods in a laboratory environment is required.

Bibliography

[1] S. Beamish, X. Li, H. Brunskill, A. Hunter, and R. Dwyer-Joyce. Circumferential film thickness measurement in journal bearings via the ultrasonic technique. *Tribology international*, 148:106295–, 2020. ISSN 0301-679X.

[2] C. M. Bender. *Advanced Mathematical Methods for Scientists and Engineers I : asymptotic methods and perturbation theory.* Springer, New York, N.Y, 2010. ISBN 9781441931870.

[3] D. D. Bonneau. Hydrodynamic bearings, 2014.

[4] C. K. Chui and G. Chen. *Kalman Filtering: with Real-Time Applications.* Springer Berlin Heidelberg, Berlin, Heidelberg, 4 edition, 2009. ISBN 3540878483.

[5] COMSOL. *COMSOL Multiphysics Version 5.6*, 2021. URL `www.comsol.com`.

[6] COMSOL. *Improving convergence of transient models*, 2021. URL `https://www.comsol.com/support/knowledgebase/1262`. Last visited: 15/04/2021.

[7] V. S. Darko Knežević. Mathematical modeling of changing of dynamic viscosity, as a function of temperature and pressure, of mineral oils for hydraulic systems. *FACTA UNIVERSITATIS, Mechanical Engineering Vol. 4, No 1*, pages 27 – 34, 2006.

[8] G. B. DuBois and F. W. Ocvirk. *Analytical Derivation and Experimental Evaluation of Short-Bearing Approximation for Full Journal Bearing*, 1953. Report: NACA-TR-1157, NASA.

[9] B. J. Hamrock, S. R. Schmid, and B. O. Jacobsen. *Fundamentals of Fluid Film Lubrication.* McGraw-Hill, second edition edition, 2004. ISBN: 0-8247-5371-2.

[10] Y. Jia, T. Wu, P. Dou, and M. Yu. Temperature compensation strategy for ultrasonic-based measurement of oil film thickness. *Wear*, page 203640, 2021. ISSN 0043-1648. doi: https://doi.org/10.1016/j.wear.2021.203640. URL `https://www.sciencedirect.com/science/article/pii/S0043164821000296`.

[11] P. Johansen, D. B. Roemer, T. O. Andersen, and H. C. Pedersen. Asymptotic approximation of laminar lubrication thermal field at low reduced peclet and brinkman number. *Journal of tribology*, 136(4):041706–, 2014. ISSN 0742-4787.

[12] A. F. Laustsen, D. Ø. Pedersen, E. V. Hansen, and M. Nielsen. *Investigation of a tribological state observer using an ultrasound reflectometry method for measurement of the fluid film height in journal bearings*, 2020.

[13] F. W. Ocvirk. *Short-bearing approximation for full journal bearings*, 1952. Report: NACA-TN-2808, NACA.

[14] Olympus. *Material Sound Velocities.* URL `https://www.olympus-ims.com/en/ndt-tutorials/thickness-gauge/appendices-velocities/`. Last visited: 17/03/2021.

[15] A. D. Pierce. *Acoustics An Introduction to Its Physical Principles and Applications.* Springer International Publishing, Cham, 3rd ed. 2019. edition, 2019. ISBN 3-030-11214-4.

[16] T. Reddyhoff, R. Dwyer-Joyce, J. Zhang, and B. Drinkwater. Auto-calibration of ultrasonic lubricant-film thickness measurements, 2007.

[17] L. W. Schmerr Jr. *Fundamentals of Ultrasonic Nondestructive Evaluation: A Modeling Approach.* Springer Series in Measurement Science and Technology. Springer International Publishing AG, Cham, 2nd ed. 2016 edition, 2016. ISBN 9783319304618.

[18] M. R. Spiegel, S. Lipschutz, and J. Liu. *Mathematical Handbook of Formulas and Tables.* McGraw-Hill Companies, fourth edition, 2013. ISBN: 978-0-07-179537-1.

[19] M. W. Spong, M. Vidyasagar, and S. Hutchinson. *Robot Modeling and Control.* John Wiley And Sons Ltd, first edition edition, 2005. ISBN-13:9780471649908.

[20] A. Z. Szeri. *Fluid Film Lubrication.* Cambridge Univeristy Press, second edition edition, 2011. ISBN-13:978-0-521-89823-2.

A Derivation of the velocity profiles in the fluid film

This appendix derives the velocity profile for the fluid film in bothin the circumferential direction, x, and the longitudinal direction, z, which are denoted u and w, respectively.

Derivation of the circumferential velocity profile, u

The velocity profile in the x-direction, u, is found in Section 3.3.2 on page 14 to be given as stated below.

$$u = C_{u1} \int \frac{1}{\mu}\, dy + C_{u2} \tag{A.1}$$

This equation contains two integration constants. These constants are found trough the known boundary conditions of the fluid film layer, as stated below.

$$u(0) = u_c \quad \textbf{and} \quad u(h) = u_a \tag{A.2}$$

The two boundary conditions gives the following two equations.

$$u(0) = u_c = C_{u1} \int \frac{1}{\mu}\, dy \bigg|_{y=0} + C_{u2} \tag{A.3}$$

$$u(h) = u_a = C_{u1} \int \frac{1}{\mu}\, dy \bigg|_{y=h} + C_{u2} \tag{A.4}$$

Solving for C_{u2} in (A.3) gives the following equation.

$$C_{u2} = u_c - C_{u1} \int \frac{1}{\mu}\, dy \bigg|_{y=0} \tag{A.5}$$

Inserting this equation into (A.4) gives the following equation.

$$u_a = C_{u1} \int \frac{1}{\mu}\, dy \bigg|_{y=h} + u_c - C_{u1} \int \frac{1}{\mu}\, dy \bigg|_{y=0} \tag{A.6}$$

This equations is then solved for the integration constant C_{u1}.

$$C_{u1} = \frac{u_a - u_c}{\int \frac{1}{\mu}\, dy|_{y=h} - \int \frac{1}{\mu}\, dy|_{y=0}} \tag{A.7}$$

The integrals in the denominator can be rewritten to a definite integral, this gives eq. (A.8).

$$C_{u1} = \frac{u_a - u_c}{\int_0^h \frac{1}{\mu}\, dy} \tag{A.8}$$

Inserting both (A.5) and (A.8) into (A.1) the following velocity profile is derived.

$$u = \underbrace{\left(\frac{u_a - u_c}{\int_0^h \frac{1}{\mu}\, dy}\right)}_{C_{u1}} \int \frac{1}{\mu}\, dy + \underbrace{\left(u_c - \underbrace{\left(\frac{u_a - u_c}{\int_0^h \frac{1}{\mu}\, dy}\right)}_{C_{u1}} \int \frac{1}{\mu}\, dy \Bigg|_{y=0}\right)}_{C_{u2}} = \frac{u_a - u_c}{\int_0^h \frac{1}{\mu}\, dy} \int_0^y \frac{1}{\mu} ds + u_c \tag{A.9}$$

Where s is a substitute variable for y.

Derivation of longitudinal velocity profile, w

The velocity profile in the z-direction, w, is found in Section 3.3.2 on page 14 to be given as stated below.

$$w = \int \frac{1}{\mu} \left(\frac{\partial p}{\partial z} y + C_{w1}\right) dy + C_{w2} \tag{A.10}$$

The integration constants are found through the following know boundary conditions.

$$w(0) = 0 \quad \textbf{and} \quad w(h) = 0 \tag{A.11}$$

These boundary conditions are based on no movement of the journal in the z-direction. These boundary condition gives the following two equations.

$$w(0) = 0 = \int \frac{1}{\mu} \left(\frac{\partial p}{\partial z} y + C_{w1}\right) dy \Bigg|_{y=0} + C_{w2} \tag{A.12}$$

$$w(h) = 0 = \int \frac{1}{\mu} \left(\frac{\partial p}{\partial z} y + C_{w1}\right) dy \Bigg|_{y=h} + C_{w2} \tag{A.13}$$

Solving for C_{w2} in eq. (A.12) gives the following equation.

$$C_{w2} = -\int \frac{1}{\mu} \left(\frac{\partial p}{\partial z} y + C_{w1}\right) dy \Bigg|_{y=0} \tag{A.14}$$

Inserting this equation into eq. (A.13) gives the following equation.

$$0 = \int \frac{1}{\mu} \left(\frac{\partial p}{\partial z} y + C_{w1}\right) dy \Bigg|_{y=h} + \left(-\int \frac{1}{\mu} \left(\frac{\partial p}{\partial z} y + C_{w1}\right) dy \Bigg|_{y=0}\right) \tag{A.15}$$

Solving for C_{w1} and redefining the integrals to definite integrals gives the following equation.

$$C_{w1} = -\frac{\partial p}{\partial z} \frac{\int_0^h \frac{y}{\mu}\, dy}{\int_0^h \frac{1}{\mu}\, dy} \tag{A.16}$$

Inserting eq. (A.14) and eq. (A.16) into eq. (A.10) The following expression is derived.

$$
\begin{aligned}
w &= \int \frac{1}{\mu}\left(\frac{\partial p}{\partial z} y + \underbrace{\left(-\frac{\partial p}{\partial z}\frac{\int_0^h \frac{y}{\mu}\,dy}{\int_0^h \frac{1}{\mu}\,dy}\right)}_{C_{w1}}\right) dy + \underbrace{\left(-\int \frac{1}{\mu}\left(\frac{\partial p}{\partial z}y + \underbrace{\left(-\frac{\partial p}{\partial z}\frac{\int_0^h \frac{y}{\mu}\,dy}{\int_0^h \frac{1}{\mu}\,dy}\right)}_{C_{w1}}\right) dy\Bigg|_{y=0}\right)}_{C_{w2}} \\
&= \frac{\partial p}{\partial z}\int \frac{y}{\mu}\,dy - \frac{\partial p}{\partial z}\frac{\int_0^h \frac{y}{\mu}\,dy}{\int_0^h \frac{1}{\mu}\,dy}\int \frac{1}{\mu}\,dy - \frac{\partial p}{\partial z}\int \frac{y}{\mu}dy\Bigg|_{y=0} + \frac{\partial p}{\partial z}\frac{\int_0^h \frac{y}{\mu}\,dy}{\int_0^h \frac{1}{\mu}\,dy}\int \frac{1}{\mu}\,dy\Bigg|_{y=0} \\
&= \frac{\partial p}{\partial z}\int_0^y \frac{s}{\mu}ds - \frac{\partial p}{\partial z}\frac{\int_0^h \frac{y}{\mu}\,dy}{\int_0^h \frac{1}{\mu}\,dy}\int_0^y \frac{1}{\mu}ds
\end{aligned}
\tag{A.17}
$$

Where s is a substitute variable for y.

B Extended Kalman filter algorithm

The EKF algorithm takes offset in the nonlinear discrete state space representation of the system, shown in the following equations.

$$\vec{x}_{k+1} = \mathcal{H}\left(\vec{x}_k, \vec{u}_k\right) + \vec{d}_k \tag{B.1}$$

$$\vec{y}_k = \mathcal{G}\left(\vec{x}_k\right) + \vec{n}_k \tag{B.2}$$

Where $\vec{x}$ is the state vector. $\vec{y}$ is the system output vector. $\vec{u}$ is the system input vector. $\mathcal{H}$ and $\mathcal{G}$ represents nonlinear vector functions of the system process and output, respectively. $\vec{d}$ and $\vec{n}$ are the system disturbance and noise vector, respectively. It is assumed that both disturbance and noise is described by Gaussian white noise, where the covariance matrices of $\vec{d}$ and $\vec{n}$ are given as $\underline{C}_d$ and $\underline{C}_n$, respectively.

The EKF algorithm consist of two main part, prediction and correction. The first part is based on the prediction of the future step based on system models and system input. This step of the algorithm is shown by the following equation.

$$\hat{\vec{x}}_{k+1|k} = \mathcal{H}_k\left(\hat{\vec{x}}_{k|k}, \vec{u}_k\right) \tag{B.3}$$

It is notable for this equation that the prediction step is denoted as $\hat{\vec{x}}_{k+1|k}$, since it is the prediction of $\vec{x}_{k+1}$ based on information given at the k'th time step. The EKF algorithm also uses an estimate of the covariance of the predicted state given by the following equation.

$$\underline{Pp}_{k+1} = \underline{A}_k\, \underline{Pc}_k\, \underline{A}_k^T + \underline{C}_d \tag{B.4}$$

Where $\underline{Pc}_k$ is the covariance of the corrected state at the previous time step. $\underline{A}_k$ is the linearised system process matrix and is found by the following equation.

$$\underline{A}_k = \left.\frac{\partial \mathcal{H}}{\partial \vec{x}}\right|_{\vec{x}=\hat{\vec{x}}_{k|k}} \tag{B.5}$$

It is in this equation seen that the linearisation point changes based on the estimated states. This is the inherent advantage of the EKF algorithm. The covariance matrix of the predicted state allows for the calculation of the Kalman gain using the following equation.

$$\underline{K}_{k+1} = \underline{Pp}_{k+1}\, \underline{C}_k^T \left[\underline{C}_k\, \underline{Pp}_{k+1}\, \underline{C}_k^T + \underline{C}_n\right]^{-1} \tag{B.6}$$

Where C_k is the linearised system output process given by the following equation.

$$\underline{C}_k = \left.\frac{\partial \mathcal{G}}{\partial \vec{x}}\right|_{\vec{x}=\hat{\vec{x}}_{k|k}} \tag{B.7}$$

The second part of the EKF algorithm concern the correction of the predicted state based on system measurements. This is achieved by firstly correcting the state estimate as given below.

$$\hat{\vec{x}}_{k+1|k+1} = \hat{\vec{x}}_{k+1|k} + \underline{K}_{k+1}\,\vec{r}_{k+1} \tag{B.8}$$

It is in this equation seen that the predicted state is corrected by multiplying the Kalman gain with the residual between the system output and the predicted system output, given by the following equation.

$$\vec{r}_{k+1} = y_{k+1} - \mathcal{G}\left(\hat{\vec{x}}_{k+1|k}\right) \tag{B.9}$$

The EKF algorithm is designed such that the Kalman gain reduces the covariance of the corrected step given by the following equation.

$$\underline{Pc}_{k+1} = \left[\underline{I} - \underline{K}_{k+1}\,\underline{C}_k\right]\,\underline{Pp}_{k+1} \tag{B.10}$$

As seen from the correction part of the algorithm, if the Kalman gain is large the algorithm uses more information from the system measurements, compared to the predicted state from the system process models. [4]

C | Derivation of the continuity equation

The derivation of the continuity equations takes offset in an arbitrary finite volume of fluid, seen in Figure C.1, with the flows in the x-direction illustrated.

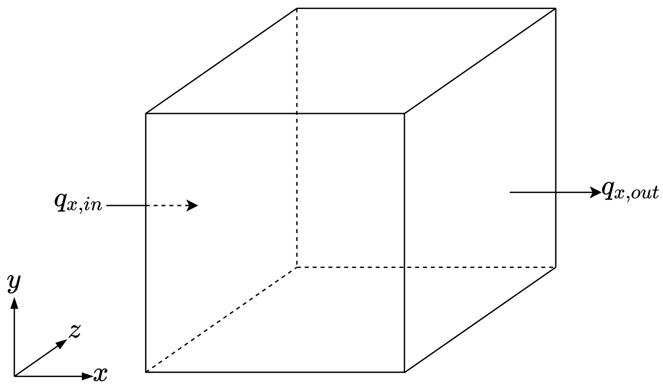

Figure C.1: Arbitrary finite fluid volume.

The net sum of the flows in all three spacial directions is given as stated below.

$$\dot{q}_x = q_{x,out} - q_{x.in} = (\rho \cdot u(x + \Delta x, y, z) - \rho \cdot u(x, y, z))\, \Delta y \Delta z \tag{C.1}$$

$$\dot{q}_y = q_{y,out} - q_{y.in} = (\rho \cdot u(x, y + \Delta y, z) - \rho \cdot u(x, y, z))\, \Delta x \Delta z \tag{C.2}$$

$$\dot{q}_z = q_{z,out} - q_{z.in} = (\rho \cdot u(x, y, z + \Delta z) - \rho \cdot u(x, y, z))\, \Delta x \Delta y \tag{C.3}$$

Considering mass conservation in the finite volume it is seen that a change in mass is caused by the flow in either of the 3 directions or a change in the density. This leads to the following equation.

$$\dot{m} = 0 = \dot{q}_x + \dot{q}_y + \dot{q}_z + \frac{d}{dt}\int \rho\, dV \tag{C.4}$$

The 3 flows are rewritten using the following Taylor approximation which is given for the x direction and where higher order terms are neglected.

$$u(x + \Delta x, y, z) - u(x, y, z) = \frac{d\, u(x, y, z)}{dx}\Delta x \tag{C.5}$$

The mass conservation, eq. (C.4), is then rewritten to the following equation.

$$0 = \frac{d}{dt}\int \rho\, dV + \frac{\partial}{\partial x}(u\, \rho)\, \Delta x\, \Delta y\, \Delta z + \frac{\partial}{\partial y}(v\, \rho)\, \Delta y\, \Delta x\, \Delta z + \frac{\partial}{\partial z}(w\, \rho)\, \Delta z\, \Delta x\, \Delta y \tag{C.6}$$

Assuming that the volume of the fluid element does not change over time eq. (C.4) is rewritten to the continuity equation which is given below.

$$\frac{\partial \rho}{\partial t} + \frac{\partial}{\partial x}(u\, \rho) + \frac{\partial}{\partial y}(v\, \rho) + \frac{\partial}{\partial z}(w\, \rho) = 0 \tag{C.7}$$

D | Virtual experiments

This appendix investigates the mesh and relative tolerance convergence used for the simulation of the virtual experiments.

Simulation Hardware

The hardware used for the virtual experiments are given in the following table.

Table D.1: The hardware used for the virtual experiments.

CPU	GPU	Memory	Storage
2 x Intel Xeon CPU E5-2660 v4 @ 2.00 GHz	NVIDIA Quadro K620	8x32 GB RAM @ 2400MHz	1 TB SSD

Solver convergence

To ensure a sufficient accuracy of the virtual experiments the relative tolerance and mesh have been altered to ensure convergence. The mesh convergence has been determined in a S.S. solver, this has been done as a more time efficient method compared to using a time dependent solver. This means a sufficient relative tolerance for the S.S. solver has to be found. The relative tolerance is related to the allowed error from the model, and it is therefore of interest to investigate the relative tolerance to ensure a low error from the S.S. solver.

The convergence of the relative tolerance of the S.S. solver is found from an external force of 50 N and an angular velocity of 100π rad/s.

The mesh of the model is separated into two parts a fluid film region and a solid region, as discussed is Section 4.4 on page 26. The initial maximum length between nodes in the fluid film region and the solid region is chosen to be 0.3 mm and 2.5 mm, respectively. This mesh size is further evaluated later when a sufficient relative tolerance has been determined. The initial mesh used to determine the relative tolerance is deemed to be more dense than the expected mesh needed for the model. This is done to mitigate the mesh affecting the result when determining the relative tolerance for the S.S. solver. [6]

To evaluate a sufficient relative tolerance for the S.S. solver the percentage deviation of the eccentricity from the result with the lowest tolerance is calculated with the following equation

$$\epsilon_{error} = \left| \frac{\epsilon - \epsilon_{fine}}{\epsilon_{fine}} \right| \cdot 100 \tag{D.1}$$

In eq. (D.1) the ϵ_{error} describes the percentage deviation between ϵ, simulated with a given relative tolerance, and the ϵ_{fine}, which is the simulation with the lowest relative tolerance. Due to the method used, the simulation with the lowest relative tolerance has an ϵ_{error} of zero and it has been excluded in Figure D.1b on the next page for this reason.

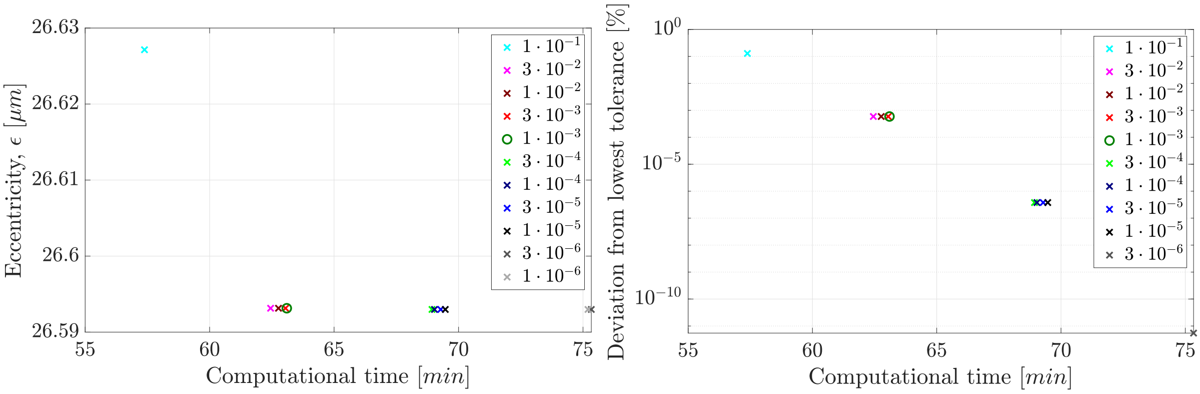

(a) S.S. solution as a function of the relative tolerance and the computational time, with the chosen relative tolerance encircled

(b) Deviation from lowest tolerance as a function of the computational time, with the chosen relative tolerance encircled

Figure D.1: Sweep of relative tolerances at S.S.

As seen from Figure D.1 the chosen relative tolerance is 10^{-3}. This point is chosen since the deviation is low and the computational time is found to be significantly faster, compared to the point with lowest tolerance. The relative tolerance chosen is seen to group with other relative tolerances however the computational time difference is low between these point for this reason the lowest relative tolerance is chosen as it should increase the accuracy with minimal performance penalty.

Next the mesh in the fluid film region is swept using the S.S. solver and the results are seen in Figure D.2.

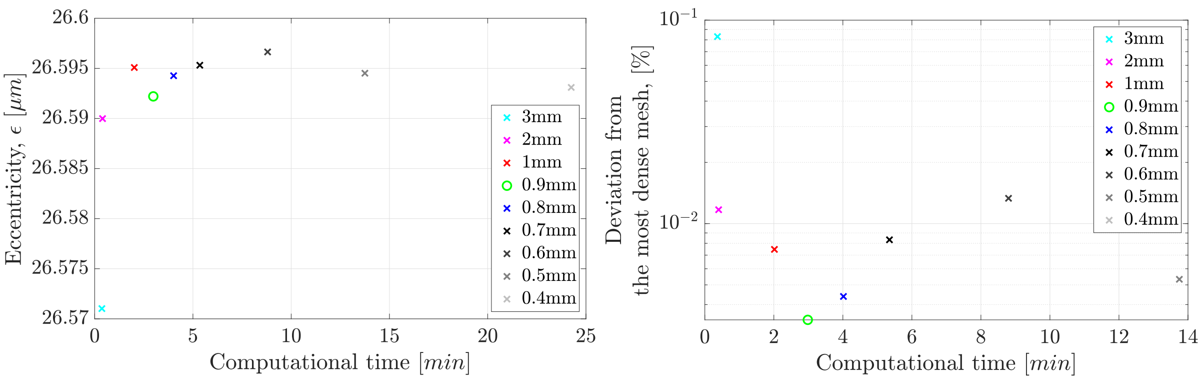

(a) Estimated eccentricity as a function of computational time

(b) Deviation from the most dense mesh as a function of the computational time

Figure D.2: Sweep of maximum length between nodes in the fluid film region.

From Figure D.2 it is seen that the maximum length between the nodes in the fluid film region are chosen to be 0.9 mm. This is chosen as it is deemed to calculate the eccentricity with a high accuracy at a low computational cost.

With a sufficient mesh for the fluid film region, the mesh for the solid region can be determined, as seen on Figure D.3 on the next page.

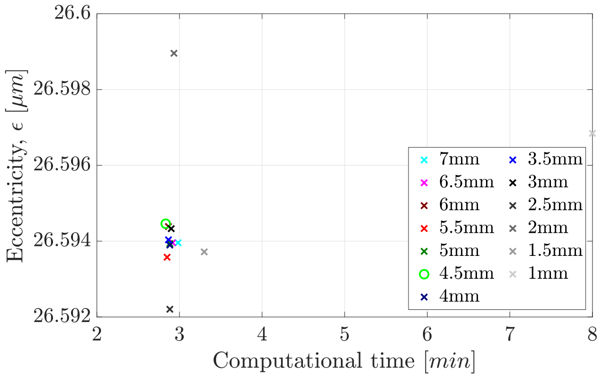

(a) Estimated eccentricity compared to the computational time, by varying the node density

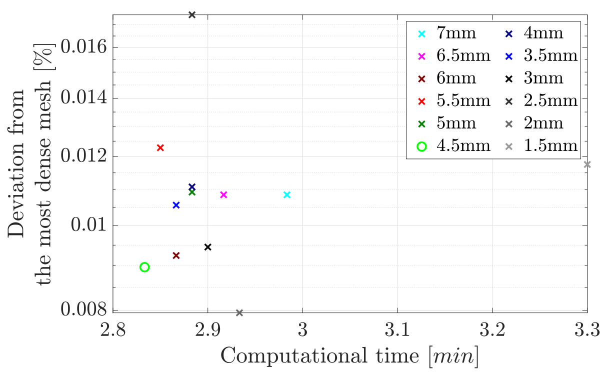

(b) Deviation from the most dense mesh compared to the computational time

Figure D.3: Sweep of maximum length between nodes in the solid area.

From Figure D.3 it is seen that the maximum length between the nodes in the solid region is chosen to be 2.5 mm. When inspecting Figure D.3b the variance in the error is seen to be low and the majority of the points is seen to group, with a low computational time. Based on this the mesh with the lowest computational time is chosen.

With a sufficient mesh for the model, the relative tolerance for the time dependent solver has to be determined. The time dependent solver uses the relative tolerance to determine the size of the time step. This means a low relative tolerance promotes smaller time steps and increases the computational time, however the dynamics is depicted with a higher accuracy. To ensure the time steps are smaller than the data logging rate, the maximum time step is set to 10 μs.

The time dependent model is simulated for 40 ms, with a binary input alternating the the force in the α-direction between 50 N and 100 N, as seen in figure D.4.

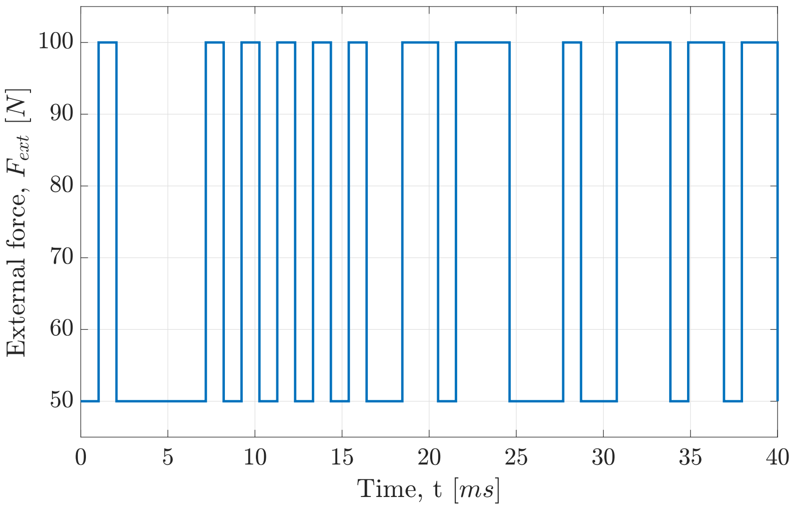

Figure D.4: Force input used for finding the time dependent relative tolerance.

The binary signal is implemented to ensure the model never reaches S.S. during the simulation, this is also seen in Figure D.5 on the next page.

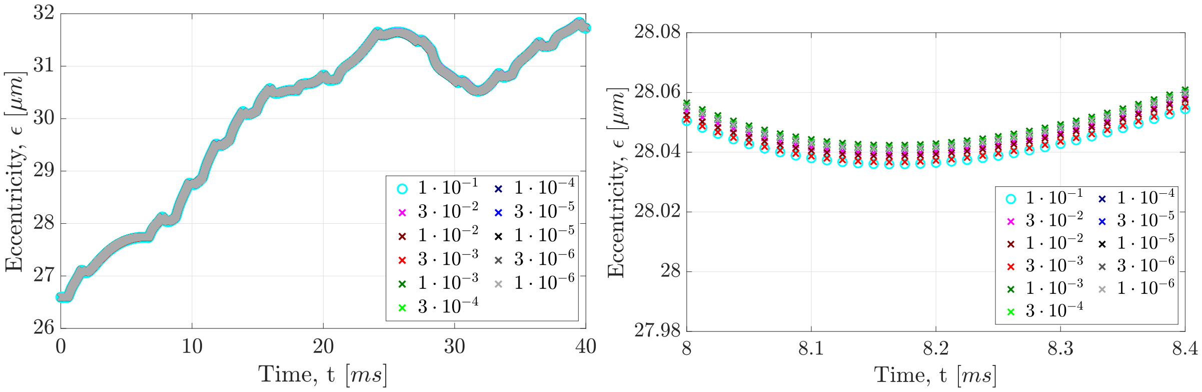

(a) Eccentricity with different relative tolerance **(b)** Zoom of eccentricity

Figure D.5: Time dependent solution with binary signal as input.

When inspecting Figure D.5a the effect of the relative tolerance is seen to be very small, however when inspecting Figure D.5b, a difference is seen. By assuming the lowest tolerance to be the most accurate, the deviation between the relative tolerance is found using eq. (D.1). This calculates an ϵ_{error} at every time stamp, to reduce the amount of points to be evaluated the RMS of the deviation for each simulation is calculated and compared to the computational time, as seen in Figure D.6.

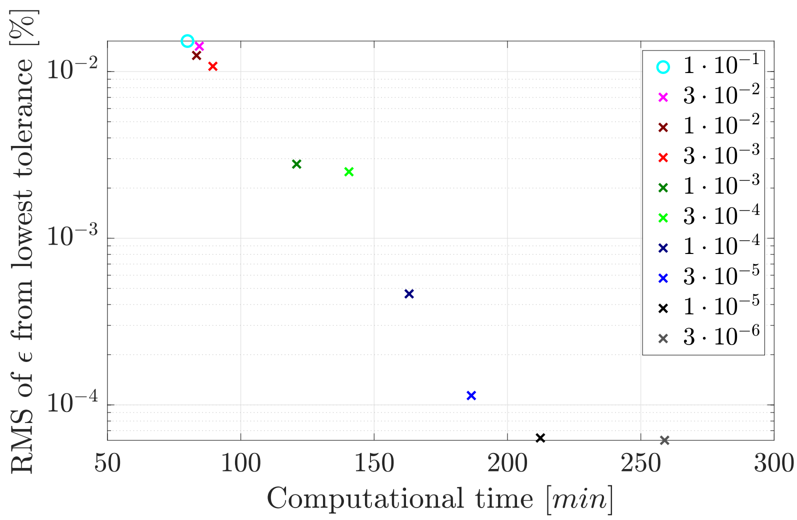

Figure D.6: The RMS error for the eccentricity time dependent.

From Figure D.6 the largest RMS is seen to be 0.02 %, which is deemed to be an insignificant error in the model. However the computational time is seen to increase as the relative tolerance is increased, for this reason the the relative tolerance for the time dependent solver is chosen to be 0.1.

E | Plot of oil properties

The models for the oil properties presented in Chapter 4 on page 21 are depicted below as functions of the fluid temperature.

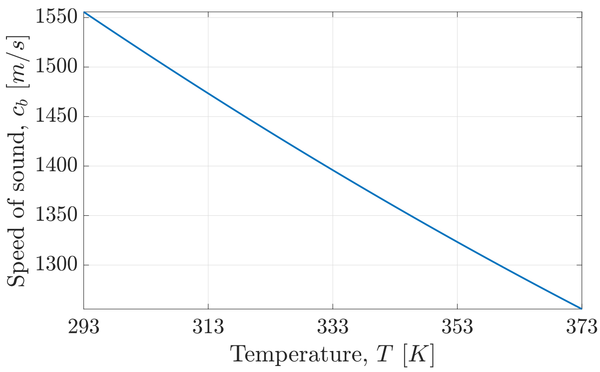

(a) Speed of sound in the oil as a function of temperature

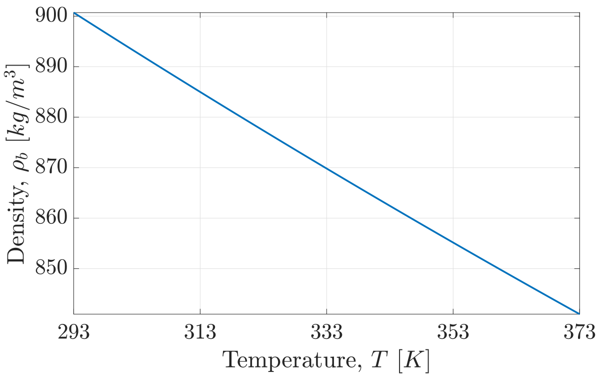

(b) Density in the oil as a function of temperature

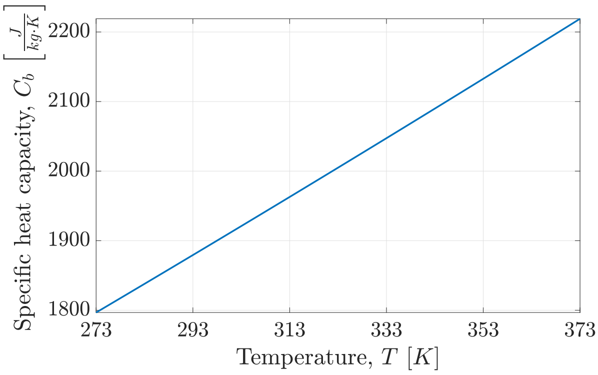

(c) Heat capacity in the oil as a function of temperature

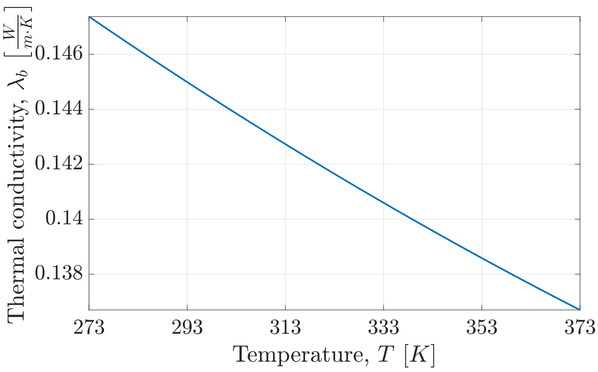

(d) Thermal conductivity in the oil as a function of temperature

Figure E.1: Hydraulic oil properties with respect to temperature

F | Sensitivity analysis

The sensitivity analysis is defined based on the following equation.

$$S = \frac{|\frac{\partial \angle J(\omega)}{\partial \gamma(\omega)}|}{|\frac{\partial \angle J(\omega)}{\partial A(\omega)}|} \tag{F.1}$$

Where A and γ is the magnitude and phase of the reflection coefficient spectrum, seen in the following equation.

$$R(\omega) = A(\omega)\left(cos(\gamma(\omega)) + i\, sin(\gamma(\omega))\right) \tag{F.2}$$

This formulation of the reflection coefficient spectrum is inserted into the layer spectrum, given by the following equation.

$$J(\omega) = \frac{1}{R_{bc}} \frac{R_{ab} - R(\omega)}{R_{ab}\, R(\omega) - 1} \tag{F.3}$$

Inserting the reflection coefficient spectrum into the layer spectrum it is seen that the layer spectrum is a function of the magnitude and phase of the reflection coefficient spectrum and the material properties of the system. Due to the complex properties of the above representation of the layer spectrum it is seen that the phase is described by the following equation.

$$\angle J(\omega) = tan^{-1}\left(\frac{Im(J(\omega))}{Re(J(\omega))}\right) \tag{F.4}$$

The sensitivity is then described by differentiating the above equation with regards to the phase and magnitude of the reflection coefficient spectrum, and inserting this into eq. (F.1). The sensitivity function is seen to then be a function the phase and magnitude of the reflection coefficient spectrum. A relation between the magnitude and phase of the reflection coefficient spectrum is however derived from considering the regression model used in the LSME algorithm, the following equation.

$$A(\omega)^2 \underbrace{\left(1 - R_{ab}^2 R_{bc}^2\right)}_{K_A} + \underbrace{\left(R_{ab}^2 - R_{bc}^2\right)}_{K_B} = 2\, A(\omega)\, cos(\gamma(\omega)) \underbrace{\left(R_{ab}\left(1 - R_{bc}^2\right)\right)}_{K_c} \tag{F.5}$$

This equation is a second order polynomial and it is possible to solve for the magnitude of the reflection coefficient spectrum, resulting in the following equation.

$$A(\omega) = \frac{K_C\, cos(\gamma(\omega)) \pm \sqrt{K_C^2\, cos(\gamma(\omega))^2 - K_A\, K_B}}{K_A} \tag{F.6}$$

It is from eq. (F.5) seen that if material a and c is of the same acoustic impedance then K_B equals zero. It is in this instance seen that when the square root term is subtracted, the numerator goes to zero. It is from this seen that the proper solution is found when the square root term is added. Inserting this expression into the sensitivity function, the sensitivity function only becomes a function of the phase of the reflection coefficient spectrum. The phase of the reflection coefficient spectrum is relates to the fluid film height from the equations below.

$$\gamma = \angle \frac{R_{ab} + R_{bc}J(\omega)}{1 + R_{ab}R_{bc}J(\omega)} \qquad \text{(F.7)} \qquad\qquad J(\omega) = e^{-\omega\tau} \qquad \text{(F.8)}$$

It is here seen that evaluating eq. (F.8) at the resonance frequency of the incident wave from ultrasound transducer, and inserting the layer spectrum into eq. (F.7), the sensitivity function becomes a function of fluid film height. The reason for evaluating at the resonance frequency of the incident wave, is that this is the frequency at which the system is most excited and from a practical point of view, this must be the frequency at which the algorithms have the most accurate fluid film height estimate.

G | Simulation parameters

Table G.1: The parameters used for the simulations throughout this project.

L_j	$50 \cdot 10^{-3}$	m	Journal length
L	$10 \cdot 10^{-3}$	m	Bushing length
R	$10 \cdot 10^{-3}$	m	Bushing inner radius
r	$9.95 \cdot 10^{-3}$	m	Journal radius
C_r	$50 \cdot 10^{-6}$	m	Radial clearance
R_b	$20 \cdot 10^{-3}$	m	Bushing outer radius
m	2	kg	Mass of the journal
a_v	63.34	µPa s	Vogel viscosity model [7]
b_v	879.8	K	Vogel viscosity model [7]
c_v	177.8	K	Vogel viscosity model [7]
a_r	$80 \cdot 10^{-3}$	Pa s	Reynolds viscosity model [3]
b_r	$31 \cdot 10^{-3}$	K^{-1}	Reynolds viscosity model [3]
a_{bv}	63.34	μPa s	Barus-Vogel viscosity [7]
b_{bv}	879.8	K	Barus-Vogel viscosity [7]
c_{bv}	177.8	K	Barus-Vogel viscosity [7]
$a_{1.bv}$	$33.4 \cdot 10^{6}$	MPa	Barus-Vogel viscosity [7]
$a_{2,bv}$	$325.6 \cdot 10^{3}$	$\frac{\mathrm{kPa}}{\mathrm{K}}$	Barus-Vogel viscosity [7]
λ_b	0.142	$\frac{\mathrm{W}}{\mathrm{m\,K}}$	Thermal conductivity in fluid [5]
f_{pr}	$80 \cdot 10^{3}$	Hz	Pulse rate frequency
T_{pr}	12.5	µs	Pulse rate time
f_s	100	kHz	Sampling rate
T_s	0.1	ns	Sampling time
q_1	888	$\frac{\mathrm{kg}}{\mathrm{m}^3}$	Density [10]
q_2	$0.7 \cdot 10^{-3}$	$\frac{1}{\mathrm{K}}$	Density[10]
q_3	293.2	K	Density[10]
q_1	761.4	$\frac{\mathrm{J}}{\mathrm{Kg\,K}}$	Specific heat capacity [5]
q_2	3.477	$\frac{\mathrm{J}}{\mathrm{kg\,K}^2}$	Specific heat capacity [5]
q_3	1.155	$\frac{\mathrm{mJ}}{\mathrm{kg\,K}^3}$	Specific heat capacity [5]
q_1	192.2	$\frac{\mathrm{mW}}{\mathrm{m\,K}}$	Thermal conductivity [5]
q_2	206.4	$\frac{\mu\mathrm{W}}{\mathrm{m\,K}^2}$	Thermal conductivity [5]
q_3	154.2	$\frac{\mathrm{n\,W}}{\mathrm{m\,K}^3}$	Thermal conductivity [5]

q_1	3.9	$\frac{\text{mm}}{\text{s K}^2}$	Speed of sound
q_2	3.39	$\frac{\text{m}}{\text{s K}}$	Speed of sound
q_3	1555	$\frac{\text{m}}{\text{s}}$	Speed of sound
q_4	273.2	K	Speed of sound
C_a	475	$\frac{\text{J}}{\text{kg}\cdot\text{K}}$	Specific heat capacity of steel [5]
ρ_a	7850	$\frac{\text{kg}}{\text{m}^3}$	Density of steel [5]
λ_a	44.5	$\frac{\text{W}}{\text{m K}}$	Thermal conductivity of steel [5]
c_a	5850	$\frac{\text{m}}{\text{s}}$	speed of sound in steel [14]
f_d	$5.86 \cdot 10^6$	Hz	Resonance frequency of incidence wave
σ	1	-	Standard deviation of ultra sound noise